The University Of Sheffield.

Deformation Of Cell Nuclei

By:

Ian Estabrook

A thesis submitted in partial fulfilment of the requirements for the degree of
Doctor of Philosophy

The University of Sheffield
Faculty of Science
Department of Physics and Astronomy

Submission Date:
April 10, 2018

Abstract

In this thesis we investigate the role of the cell nucleus in processes that involve nucleus deformation. To begin with, we mathematically model the motion of molecular motors, using an asymmetric particle model, as a method to describe one force generation mechanism within a cell. This model is used to explore the effects of molecular motors working in tandem while attached to a single object, such as the cell nucleus. We then move on to developing a analysis tool for use with images of nucleus deformation. This computational tool uses a simulated annealing energy minimisation method with classical elasticity to determine the deformation of the nucleus between images, and from the deformation field, make predictions about the traction force on the surface of the nucleus which caused the observed deformations. We begin by treating the nucleus as a homogeneous elastic solid and calculating the traction force to cause the deformations observed of nuclei as they pass through channels containing constrictions. We then developed a second model of the nucleus, where it is instead treated as a thin homogeneous elastic shell. The shell model of the nucleus was then applied to the same images of nuclei passing through channels, and the resulting traction forces compared with the solid model results. Both the solid and shell models of the nucleus were then developed further to calculate the traction force on a deforming nucleus, when using three dimensional images in the form of a series of z stacks as input. We also combine the traction force calculations with an iterative method to calculate Poisson's ratio from experimental images and compared this with previously published data of nuclei.

Acknowledgements

I would like to thank my supervisor, Rhoda Hawkins, without whom, this work and thesis could not have been completed. I also thank the various collaborators who shared experimental images with us, Hawa Thiam and Matthieu Piel, Pedro Monteiro and Susana Godinho and Ivie Aifuwa and Denis Wirtz. The images they provided and discussions with them helped develop the research presented in this thesis. I would also like to thank everyone that provided feedback and useful discussions throughout the course my PhD, including other members of the research group.

Contents

Nomenclature

Biological syntax used in this thesis, together with brief descriptions are included below.

- **Actin.** A protein found in the cytoskeleton. Actin is bound to by the myosin family of molecular motors.

- **Cytoplasm.** The cytoplasm of a cell refers to all components within a cell, with the exception of the cell nucleus.

- **Cytoskeleton.** The cytoskeleton is a structure within the cytoplasm, consisting of actin filaments, microtubules and intermediate filaments.

- **DNA.** Deoxyribonucleic acid. DNA is found within the cell nuclei and carries the genetic information for the cell. DNA is seen in chromosomes and is surrounded by the nuclear envelope to help protect the DNA from damage.

- **Dynein.** A family of molecular motors which walk towards the minus (-) ends of microtubules.

- **Eukaryotic cells.** Eukaryotic cells are cells which contain membrane bound organelles, such as the cell nucleus, as compared to prokaryotes which are cells that do not. Typical examples of eukaryotic cells include most animal and plant cells.

- **Kinesin.** A family of molecular motors which walk towards the plus (+) ends of microtubules.

- **Metastasis.** The process by which cancer cells spread from one part of the body to another. Typically involves travel from a tumour in to the blood stream, and then exiting elsewhere in the body to form secondary tumours.

- **Microtubules.** Microtubules are long rigid (in comparison to actin filaments) tubes made of the dimer tubulin.

- **Molecular motor.** A molecular motor is a molecular scale motor that exist within biological systems. The families Kinesin and Dynein bind to microtubules, while the Myosin families bind to actin filaments.

- **Myosin.** Myosins are a family of molecular motors which walk along actin filaments.

- **Nuclear envelope.** The nuclear envelope is a double layer membrane surrounding the cell nucleus, separating the cell cytoplasm and the DNA within the nucleus. The envelope contains nuclear pores which allow the passage of proteins in to and out of the nucleus.

- **Nuclear pores.** Nuclear pores are pores on the surface of the nucleus, which allow the passage of proteins in to and out of the cell nucleus.

- **Nucleus.** The nucleus of a cell contains the DNA and associated proteins, surrounded by the nuclear envelope. The nucleus exists in most eukaryotic cells and is important for continued cell existence.

Chapter 1

Introduction

1.1 Introduction

In this chapter, we briefly describe some specific aspects of cell biology relevant to this thesis. In particular, we first describe the cell, which is relevant to the whole thesis, and also the cell nucleus, focusing on its role within the cell. We describe some methods for observing the cell nucleus through experiments using fluorescent dyes to be able to observe the cell nucleus separately from the surrounding cytoplasm. We also discuss the role of molecular motors in the cytoskeleton, providing a basis for the analytical model of molecular motors developed in chapter 2. We introduce physical concepts in each of the chapters as they become relevant.

1.2 Cells

The cell is the fundamental building block of life, and forms the basis for all types of life, from single cell bacteria to complicated multicellular animal and plant organisms. Broadly, the cell consists of the cytoskeleton and associated proteins, and the cell nucleus.

1.2.1 Imaging cells

The term cell was first used to describe an observation made in 1665 by Robert Hooke when looking through a microscope at a slice of cork, where he observed what is now known as the cell wall of the plant. Van Leewenhoek observed the first protozoa in 1674 and then bacteria in 1683, where these were identified as evidence of life at microscopic scales, due to the fact that they exhibited motion. Even now, hundreds of years later, modern research of cells relies heavily on imaging biological matter to aid in our understanding. Experimental methods of imaging are still among the most important techniques in understanding the cell, and the different components within the cell. Chapters 3 to 6 of this thesis focus on modelling the cell nucleus

as it undergoes deformation. As such, experimental techniques that allow observations of the nucleus were key to the development of the models we made. We also briefly detail more recent imaging developments that have been used in experiments performed by collaborators to obtain the data used within this thesis.

The ability to identify different aspects of the cell, including the cell nucleus, has been paramount to enabling detailed studies of the nucleus. One particular innovation was the use of fluorescence in imaging. As the cell is largely water based, methods that cause parts of the cell to emit wavelengths of light were important in enabling the use of light microscopes on biological samples. One method is to use fluorescent proteins such as Green fluorescent protein (GFP) tagged to a protein by inserting DNA in to the genome of the target to be imaged. By placing GFP next to a specific protein, the GFP can be used as a tag to that protein. Another method is to use fluorescent dyes. A fluorophore binds to a specific element within the cell. Upon excitation, the fluorophore emits a wavelength of light which can be recorded using a fluorescence microscope. The fluorescence can be used to track the location of a tagged element in the cell, by measuring the intensity of emitted light over space and time in the resulting images.

Though dyes exist for a number of different biological molecules, the dyes of interest in this thesis are those which attach to parts of the nucleus. There are two families of dyes commonly used to stain the cell nucleus. They are the DAPI and the Hoescht families of dyes. Both of these dyes bind to A-T rich regions of DNA, and then emit light through fluorescence. The resulting fluorescence provides an intensity for a given pixel, representing a region in space. This is then used to determine whether a given pixel contained DNA or not. As typically the DNA is contained entirely within the nucleus of the cell, as discussed in section 1.2.2, this allows for the position of the nucleus to be identified. There are a few examples where the DNA could be outside of the nucleus in significant quantities, such as a rupture of the nuclear envelope,

but these cases are not considered in detail within this thesis.

1.2.2   The cell nucleus

The cell nucleus is an organelle which exists in eukaryotic cells. The nucleus is of particular interest due to applications in medical diagnosis. This is especially true for the diagnosis of cancers where it has been observed that the changes to the cell that cause cancerous behaviours also typically causes measurable changes to the nucleus shape [10]. The nucleus consists of two thin membranes, forming the nuclear envelope, surrounding tightly packed DNA. In developed cells, DNA is typically stored in the nucleus by having been tightly wrapped around histones, forming chromosomes[3]. The response of the nuclear envelope and the DNA to applied forces are important when considering how best to model the nucleus. We now describe these components and some related experiments in more detail.

On the inner surface of the nuclear envelope is a layer formed of proteins from the Lamin A/C and Lamin B families, known as the nuclear lamina. The nuclear lamina is formed from a dense network of these lamin proteins. For this thesis, the most important property of the nuclear lamina is that it is responsible for the stiffness of the cell nucleus. However, the role that each of the lamin families play in providing the stiffness is a relatively recent research area, and there is still some debate on the purpose of the lamin A/C and B1/B2 families in response to applied forces.

The mechanical response of the nuclear lamins in the lamina have been studied through treatments that inhibit the lamin A proteins, and then applying mechanical strains to the nucleus [23]. When a cell is deficient in lamin A/C, they typically have many more misshapen nuclei, as well as demonstrate a less nucleus more prone to rupture, which is interpreted as being a less stable nucleus[23].

1.2.3 Cells in confinement

In chapter 3, we develop a tool for analysis of experimental images of cell nuclei. The approach we took in developing the model and code was driven in part by experimental procedures. In this section, we describe some relevant experiments that helped form the approach used.

Cell confinement is often looked at in the context of cell motility. By confining the cell, you can limit the motion to one or two dimensions, rather than the three dimensional motion observed in cells in collagen matrices. The motion mechanisms used by cells have been seen to differ in confined motion compared to the three dimensional motion.

Cell motion within confined geometries can be induced through various experimental techniques, some examples of which include flow driven motion, such as in flow induced cytometry [26]. Cytometry is where cells are placed in a fluid flow which rapidly passes them through an imaging device to measure deformations. Another common approach is the use of chemical gradients to affect the direction of motion of the cells.

It is also possible for cells to self generate motion in confinement without any of the above chemical or physical cues causing the motion. This is the case for the cells confined to channels containing constrictions as shown in the experimental data in chapters 3 and 4. In the images of the nucleus within channels, the nucleus has to deform in order to pass through small constrictions. This is typically a significantly slower process than the deformation of the cytoplasm over the same shape change of the surrounding environment. Similar observations that significantly larger forces are needed to deform the nucleus have also been reported in micropipette aspiration [31] and Atomic force microscopy (AFM) experiments [21]. This causes the motion of the entire cell to slow down while the nucleus undergoes deformation [36]. This has important applications in medical diagnosis, where the stiffness of the nucleus can be affected by diseases, such as in cancer. Isolated cancerous cells have been measured to be softer than normal cells, despite evidence

indicating that when large numbers of cancerous cells come together forming tumours, the resulting tumour tissue is stiffer than healthy tissue [5].

As a result of the nucleus being stiffer than the cytoplasm, the forces required to deform a nucleus are larger than those exerted on the cytoplasm. This has potential applications in the diagnosis of disease, where observations of the deformations of the nucleus and cell could be used to determine, for example, if they are cancerous [26].

1.3 Molecular motors in intracellular processes

In chapter 2, we produce a model of molecular motors pulling a load, where the load could represent for instance, the nucleus of the cell, to position the nucleus as the cell undergoes mitosis, or to move vesicles around within the cell. The cytoskeleton is responsible for a number of active processes in the cell, including mechanisms of motility. This includes generating motion of the entire cell as well as intercelluar processes, such as the movement of vesicles or the cell nucleus. The main components of the cytoskeleton which are of interest to us are the filaments actin and microtubules and the molecular motor proteins, myosin, dynein and kinesin. The myosin family of molecular motor proteins interact with actin filaments, while kinesin and dynein interact with microtubules.

Molecular motors move in discrete steps along the filaments to which they bind. This stepping motion has been observed in optical trap experiments, where molecular motors have been attached to a bead, with the bead held in place by the pressure of a laser, which is used to exert force on the bead. The bead then moves in discrete steps away from the starting position as a molecular motor takes a step, and exerts force on the bead. These experiments have allowed the step size of different motors to be measured. Optical bead experiments have produced other results including the stall force of a single motor. The stall force was found by increasing the pressure of the

laser on the bead, until the motion of the bead is completely inhibited. This allowed calculation of the maximum force that a motor can bare while still causing motion of the bead.

The stepping motion of a molecular motor can be broken down in to multiple steps. First, a adenosine triphosphate (ATP) molecule binds to a molecular motor, then a hydrolysis process begins to release the energy stored in the chemical bonds. This is then converted in to kinetic energy by the motor.

Chapter 2

Molecular Motors

2.1 Introduction

In this chapter, we model molecular motors moving inside a cell.We have developed an analytical model of the velocity of a cluster of motors moving along cytoskeletal filaments. In section 2.2 the fundamental equations of the Asymmetric Simple Exclusion Process (ASEP) model used to describe the collective behaviour of stepping molecular motors are derived. We then extend the results derived by Joanny et al. [7] for a fixed number of motors on a single track by introducing the ability for motors to bind or unbind to the filament. In this case, the motors come from an effectively infinite source, and the effect of this on the steady state behaviour of the system is explored. In section 2.3, we allow the unbinding rate to vary with the load force carried by a motor, where the load force increases the unbinding rate exponentially. Next, in section 2.4 the forces are allowed to have a component dependent on the speed at which the load moves, in order to represent the drag force component caused by motion of an object within a fluid, such as the nucleus within the cytoplasm. Finally in section 2.5, we briefly discuss extending the model to allow multiple parallel tracks with bound motors.

2.1.1 Molecular motors

Molecular motors are a family of proteins that are capable of turning biochemical energy from adenosine triphosphate (ATP) hydrolysis in to mechanical work. Here we consider the action of cytoskeletal motors that bind to cytoskeletal filaments, such as the Myosin family of motors which bind to actin filaments, rather than other types of motors, e.g. the rotary motion generated in rotational driven motion of e-coli, or the Nucleic acid motors involved in various DNA binding processes. The decision to model molecular motors with stepping motion, such as Myosins and Kinesins was motivated by images such as figures 2.1 and 2.2, where an increase in the amount of the Actin/Microtubule respectively was observed as the nucleus deforms. One

possible reason for the observed increase in filaments is that the filaments are used by motors to exert force on the nuclear lamina, causing the nuclear deformation.

Myosin molecular motors produce useful work in the cell cytoskeleton, such as allowing the movement of vesicles within cells, through attachment and detachment processes to a track made of filamentous actin. The motors generate work by detaching a head from the filamentous actin, then by consuming energy generated through ATP hydrolysis, move the head forward along the filaments. In Myosin, this occurs by swinging a lever arm further along the filament, where the motor head is attached at the base, causing the stepping motion of the motors. Most Myosin family motors have two heads, which alternate between steps on a filaments in order to walk in a preferred direction on a filament, typically towards the barbed end of a filament. The velocity at which a Myosin molecular motor travels depends strongly on the particular family member considered, with the length of the arms of the myosin, the rate at which it can undergo hydrolysis,how long it typically spends bound on a single site, the angle at which it steps at all contributing to the speed at which they can function. For instance Myosin II and V have step sizes of 8nm and 36nm respectively, where Myosin V is typically responsible for transport while Myosin II is used in actomyosin force generation mechanisms such as muscle contraction.

The other common molecular motors in cells are Kinesin and Dynein, which walk in a similar fashion to Myosins, along microtubules rather than actin. Kinesin and dynein are similar to each other, except the have different directions of motion along microtubules, towards the + and - ends respectively. Microtubules are typically involved in processes that take place over longer distances than actin, owing to the increased persistence length of microtubules. For instance, Microtubules, Kinesin and Dynein are typically involved in intracellular transport of vesicles and organelles, and are capable of transport velocities of up to $3\mu m/s$. [4]

(a)

(b)
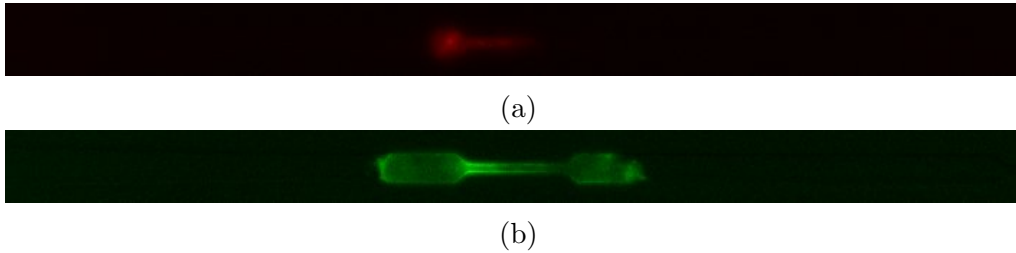
Figure 2.1: Example of Nucleus of epithelial cells of mice. Figure 2.1a shows the DNA within the nuclei (red) and figure 2.1b shows the filament actin (green). There is an increase in actin at the entrance in to the constriction, along the sides of the constriction/nucleus. Images provided by Hawa Thiam and Matthieu Piel, Institut Curie.

Molecular motors are one mechanism that cells use to internally generate force. This can lead to nucleus deformation. for the cell to use to cause nuclear deformation is through force application by molecular motors. When some cell nuclei are undergoing deformation, an increase in the number of filaments used by molecular motors observed. An example of this is shown in Figure 2.2. The figures show RPE-1 cells, expressing polo-like kinase 4 (PLK4), a regulator of the centrosome, where expression levels of PLK4 have been reported to be affected in tumours [20]. The image in figure 2.2a is of nuclei prior to treatment with the antibiotic Doxycycline and figure 2.2b shows nuclei after treatment. The images show that extra centrosomes have formed around the nucleus, and the number of microtubules significantly increased. The nuclei have extended to a more elliptical cross section from the untreated shape. The direction of elongation is generally close to the orientation of the microtubules near the nucleus, suggesting they play a role in the observed shape change. Though molecular motors are not shown in these images, the use of molecular motors stepping on the tracks is one possible way for the force required for the observed nuclear deformation to occur. A similar increase of the filament actin can be seen in the images used in chapter 3, where nuclei enter in to channels. Similarly to the increase

(a)   (b)
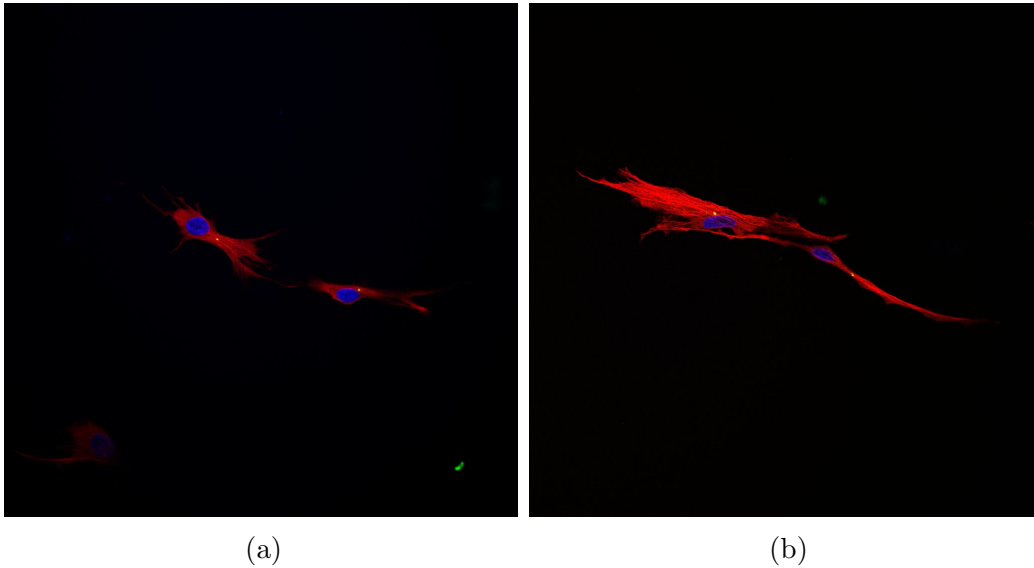
Figure 2.2: Example of Retinal Pigment Epithelial (RPE-1) cells. The nucleus of the cells are stained in blue, microtubules in red and centrosomes in green. Figure 2.2a shows an example of these nuclei prior to treatment, and figure 2.2b shows nuclei after treatment with the antibiotic Doxycycline. Images provided by Pedro Monteiro and Susana Godinho, Barts Cancer Institute, Queen Mary, University of London.

in microtubules deforming upon chemical treatment, when the nucleus is entering in to the constrictions there is an increase in the amount of actin around the nucleus. These images of nucleus deformation motivated the modelling of molecular motors in the following sections of this chapter.

The discrete stepping motion of molecular motors has been observed in optical bead experiments. These experiments study the properties of molecular motors through the use of optical traps [37]. A bead is placed in an optical trap, in a solution containing molecular motors which attach to the bead. As the motors move with the attached bead, the bead position is measured, and changes in discrete steps, demonstrating the discrete stepping of the motors [37]. Th the motion of the bead under the applied pressure allows the measurement of properties of the various Myosins or Kinesins [37, 1] such as the

step sizes, stepping rates and the stall force for different molecular motors.

2.2   The asymmetric simple exclusion process model of processive stepping motors

The statistical properties of a collection of moving particles on a track can be described using a Asymmetric Simple Exclusion Process (ASEP) model. The ASEP model was originally derived by Frank Spitzer [33] as a mathematical treatment of interacting moving particles. Since then, it has been expanded to many transport phenomena, including traffic flow [13], crowd motion[15], and most relevant to this thesis, the motion of stepping molecular motors. In this model, we treat molecular motors as pointlike particles moving along one dimensional tracks. This model allows molecular motors movement in both directions along the track, but to have biased motion in one direction. This is similar to describing the motion of motors using a classical Brownian ratchet where each the stepping motions of each motor are described stochastically [16, 2].

In the ASEP model, we treat the filaments that the motors walk along as a series of sites, where each site can be occupied by at most a single motor. Physically, the size of each site corresponds with the step size of the motors. A single track is then essentially a one dimensional system with particles moving forwards and backwards between adjacent sites along the track. A cartoon showing this process for a single motor bound on a track can be seen in figure 2.3, showing the stepping rates for that motor p_μ and q_μ in the respective directions.

The ASEP model treats molecular motors as having the following properties. Each motor is capable of moving in both directions along the track, with the forward stepping rate p_μ and backwards stepping rate q_μ. These rates describe the average time taken for a motor to move from one site to a neighbouring empty site in the corresponding direction. The stepping pro-
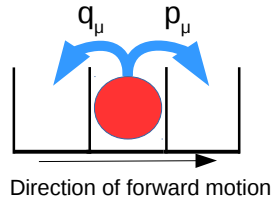
Figure 2.3: Cartoon showing a particle representing a molecular motor, and a small segment of the track representing the filament that the motor walks on. Each particle μ has stepping rates p_μ forwards and q_μ backwards. The stepping rates can be varied for different motors.

cess for a single motor is shown in figure 2.3. Each step taken by a motor is of a fixed length of one site in the corresponding direction to an adjacent, unoccupied site in either forwards or backwards directions.

Each motor can also be allowed to bind or unbind to the filamentous track. The process of binding or unbinding are described by the binding rate k_{on} and unbinding rate k_{off} respectively. A simple cartoon of this process is shown in figure 2.4. A given motor is either bound or unbound to a filament. A bound motor has a position on a filament, representing the site to which it is bound and the relative position of that motor compared to the others. An unbound motor is part of a large, effectively infinite source of motors around the tracks, which can bind to sites at the rate k_{on}. As with the stepping rates, each site may only be occupied by a single motor, and a motor cannot bind to an already occupied site.

The stepping rate of molecular motors has been shown in optical bead experiments to depend on the load force on the motor [30]. An increase in load force has been seen to cause an increased stepping rate towards the load (typically backwards) under large loads in myosin V motors [30].Similar results are seen in the motion of Myosin II in muscle contraction [29]. Here, myosin II molecular motors are responsible for sliding filaments together to cause muscle shortening. By reducing the load force required to contract muscle, the process has been seen to speed up significantly [29].
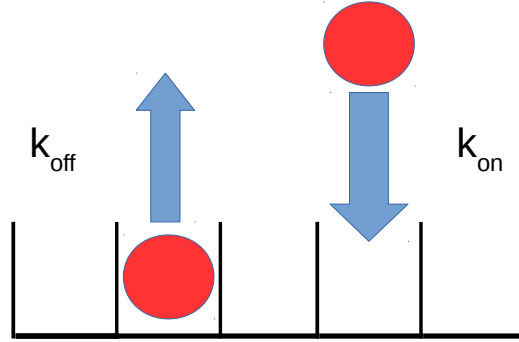
Figure 2.4: Cartoon showing particles binding and unbinding from a track. The particles bind with rate k_{on} and unbinding with rate k_{off}

One way the dependence of the motor stepping rates on the load force has been included in the ASEP model by allowing the values of p and q to vary with the applied force, as exponential functions affecting the stepping rates for any motor which is under load as shown below [7].

$$p_{lead} = p_0 e^{-f\delta} \tag{2.1}$$

$$q_{lead} = q_0 e^{f(1-\delta)}. \tag{2.2}$$

Here, f represents the load force on the motor in dimensionless units. δ is a value that varies from 0 to 1, representing the relative effect of the increased energy barrier under the load force on the ability of the motor to step forward, leading to a reduced stepping rate forward. For $\delta = 0$, the forward stepping rate is unaffected by the motor carrying a load, while the backwards stepping rate increases strongly for larger forces. For $\delta = 1$ the leading stepping rate decreases strongly under applied forces and the backwards stepping is unaffected by the load. Specifically, the leading motor on a given track experiences the load force, while the other motors do not. The stepping rates of the leading motor are allowed to vary dependent on the load force f as given in equations 2.1 and 2.2, where the forward and backwards stepping rates are now proportional to exponential functions of
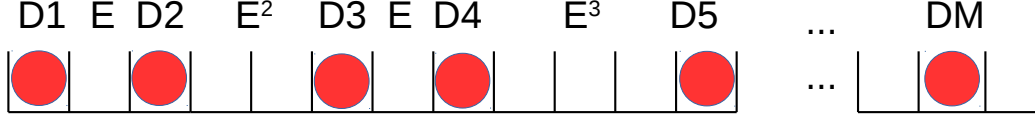
Figure 2.5: An example of the matrix description of motor positions. Each site occupied by a motor is labelled by a D, then a number counting which of the motors is represented. Each empty site is labelled by an E, with multiple consecutive sites being labelled by $E^{emptysites}$. In this example, the first motor is labelled D1, then an empty site E, the second motor D2, then two empty sites by E^2, so on. So the matrix product representing this configuration begins as $D_1 E D_2 E^2 ...$

the dimensionless force.

Following [12, 11] we studied the properties of a cluster of motors on tracks with the following matrix method. Each possible configuration of a number of motors and number of sites can be described through the statistical weight of the given configuration occurring. Each given site that is unoccupied is represented by a matrix E, and an site occupied by motor μ is represented by a matrix D_μ. A combination with n_1 holes after the first motor, n_2 holes after the second motor and so on, with M total motors is given by the matrix product of all the matrices representing the configuration. An example of this configuration is shown in figure 2.5.

The statistical weight, f_n, of the system for a given configuration n is then the trace of this product

$$f_n(n_1, n_2, n_3, ..., n_M) = Tr\left(D_1 E^{n_1} D_2 E^{n_2} D_3 E^{n_3} ... D_M E^{N_M}\right). \qquad (2.3)$$

The probability of being in any given state is found by normalising these weights by the partition function of the system, which is given by the sum of all possible states

$$Z_{n,m} = \sum_{n_1, n_2, ..., n_M} \delta_{(\sum n_\mu, N-M)} f_n(n_1, n_2, n_3, ..., n_M). \qquad (2.4)$$

For the weights f_n to represent the steady state of the system, the difference between probabilities of a given motor stepping in each direction from an occupied site into an empty site must be equal to the rate of the site being occupied, i.e.

$$p_\mu D_\mu E - q_\mu E D_\mu = D_\mu \qquad (2.5)$$

must hold for each motor μ.

In addition, since particles are unable to overtake each other due to the exclusion principle of occupied sites, the velocity of the entire cluster of motors is limited by the velocity of the forward most motor.

The theory set out by Evans [12] was used by Campas et al [7] to show that for a fixed number of motors, N (i.e. no binding or unbinding allowed), on a single track given by a ring, the mean velocity of the cluster of motors is given by

$$\bar{v} = \frac{p \left[1 - e^f \left(\frac{q}{p} \right)^N \right] \left[1 - \frac{q}{p} \right]}{e^{f\delta} \left[1 - \frac{q}{p} \right] + e^f \left[\frac{q}{p} - \left(\frac{q}{p} \right)^N \right]}. \qquad (2.6)$$

The result derived for equation 2.6 presumes that motors are unable to bind or unbind from the track. We now introduce the effect of unbinding and binding processes in to the model. If the motors can bind to and from the track, at rates k_{on} and k_{off} respectively, then we can predict the typical number of motors bound to the filament.

In the simplest case, we expect that the number of motors bound is described as a function of the binding and unbinding rates, where k_{on} and k_{off} are both force independent. In this case, where $P(n)$ is the probability of having n motors bound, the change in number of motors is given by the following master equation,

$$\frac{dP_n}{dt} = k_{on}P_{n-1} + k_{off}P_{n+1} - (k_{on} + k_{off})\,P_n. \tag{2.7}$$

To investigate the average collective behaviour of a cluster of motors capable of binding and unbinding, we consider only the steady state case of motor behaviour. This requires that the average number of motors bound to the filament does not change with time, hence $\frac{dP_n}{dt} = 0$ and the binding rates and states with n bound motors are related by

$$k_{on}P_{n-1} = k_{off}P_n \tag{2.8}$$

In the steady state, the number of motors bound therefore depends on the relation between the binding and unbinding rates, as well as the number of accessible sites for motors to bind to. We presume that the number of accessible binding sites on the track is much greater than the number of motors capable of attaching to the cargo. This assumes that the limiting rate is the number of motors capable of binding to the cargo rather than having excess motors but no sites for the motors to bind to. Physically this means that the size of the motors is far smaller than the cargo.

The mean average number of bound motors and velocity of the cluster of motors for a maximum number of sites N are given respectively as

$$\bar{n} = \sum_{n=0}^{N} nP_n, \tag{2.9}$$

$$\bar{v} = \sum_{n=0}^{N} P_n v_n. \tag{2.10}$$

The probability of being in a state with n bound motors P_n, can be written for the steady state case as a function of the binding rates k_{on}, k_{off} and the maximum number of motors bound, N. In the case where the binding and unbinding rates are constant, then the normalised probability P_n can be

written explicitly using equation 2.8. This equation can be generalised to

$$P_n = \left(\frac{k_{on}}{k_{off}}\right)^m P_{n-m} \tag{2.11}$$

where $n - m \geq 0$ and $N \geq n$. This can be used to write all the probabilities in terms of the binding rates and the probability of having no motors bound, i.e. $m = n$.

$$P_n = \frac{k_{on}}{k_{off}}^n P_0 \tag{2.12}$$

Since the total sum of the probabilities of all possible states allowed of the system most be equal to 1, we have

$$\sum_{n=0}^{N} P_n = \sum_{n=0}^{N} \frac{k_{on}}{k_{off}}^n P_0 = 1. \tag{2.13}$$

This gives an expression for the probability of being in a state with n motors bound in terms of only the binding rates,

$$P_n = \frac{\left(\frac{k_{on}}{k_{off}}\right)^n}{\sum_{n=0}^{N} \left(\frac{k_{on}}{k_{off}}\right)^n} = \frac{\left(\frac{k_{on}}{k_{off}}\right)^n}{1 + \sum_{n=1}^{N} \left(\frac{k_{on}}{k_{off}}\right)^n} \tag{2.14}$$

where the normalisation is found from the summation of all possible states, $\sum_{n=0}^{N} P_n = 1$.

Since the summation in the denominator is a finite geometric series, we can rewrite this as

$$1 + \sum_{n=1}^{N} \left(\frac{k_{on}}{k_{off}}\right)^n = \frac{\left(\frac{k_{on}}{k_{off}}\right)^{N+1} - 1}{\frac{k_{on}}{k_{off}} - 1}.$$

Which gives the full expression for the probability of being in the state with n bound motors as

$$P_n = \frac{\left(\frac{k_{on}}{k_{off}}\right)^n \left(\frac{k_{on}}{k_{off}} - 1\right)}{\frac{k_{on}}{k_{off}}^{N+1} - 1}.$$ (2.15)

In the case where only the leading motor on a track experiences the load force, the velocity of a state with n motors is given by equation (2.6). Substituting this velocity expression together with the expression for the probabilities, equation (2.15) in to equation 2.10 describes the effective speed of a cluster of motors with the ability to bind to and from the filament. The velocity in this case is then given by

$$\bar{v} = \frac{\frac{k_{on}}{k_{off}} - 1}{\frac{k_{on}}{k_{off}}^{N+1} - 1} \sum_{n=0}^{N} \left(\frac{p \left[1 - e^f \left(\frac{q}{p}\right)^n \right] \left[1 - \frac{q}{p} \right]}{e^{f\delta} \left[1 - \frac{q}{p} \right] + e^f \left[\frac{q}{p} - \left(\frac{q}{p}\right)^n \right]} \left(\frac{k_{on}}{k_{off}} \right)^n \right).$$ (2.16)

A comparison of the results with binding given by equation 2.16 with the results for a fixed number of motors, given by equation 2.6 is shown in figure 2.6. In both cases, the expected velocity for a system with many motors tends to the difference between the forward and backwards stepping rates, $p - q$ when the load force is small, and is otherwise limited by the stepping rate of the forward most motor, $pe^{(-f\delta)}$. As the dimensionless force increases however, there is a sharper decrease in the expected value of velocity for the case where binding and unbinding occurs, despite currently assuming the unbinding process to be force independent. This decrease exists because while the maximum number of motors that can bind is the same as in the case where binding and unbinding does not occur, the probability of being in the state with all motors bound would only be equal in the case where binding is significantly higher than the unbinding rate. As the force increases, the stepping rate of the leading motor decreases significantly, which then decreases the expected velocity of the system, despite the lack of direct force dependence in the unbinding rate.
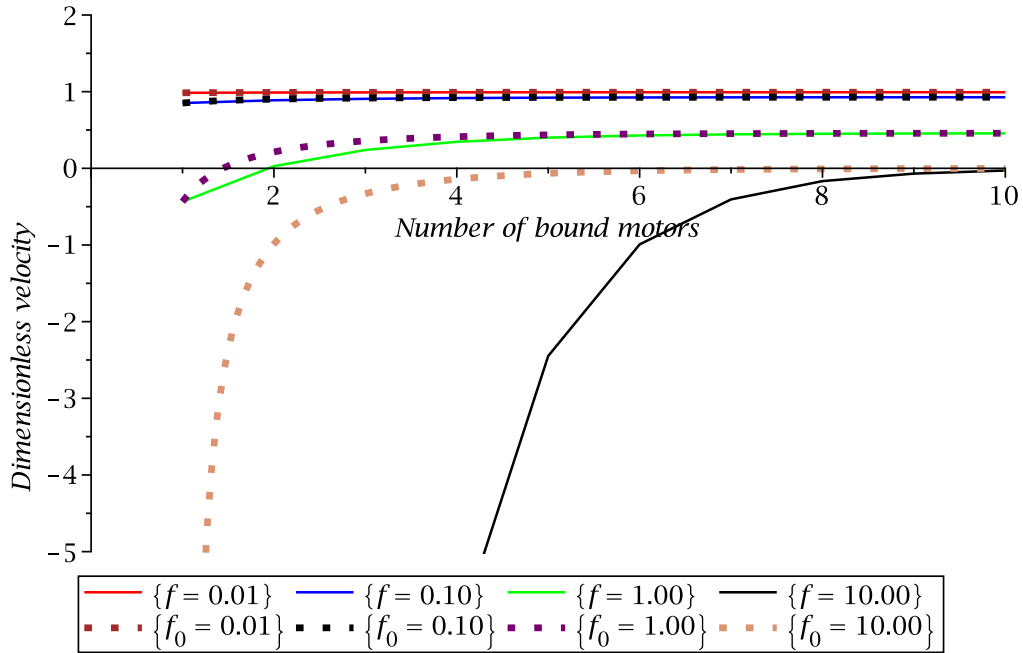
Figure 2.6: A comparison of the effect of allowing motors to bind or unbind. f_0 represent the original result given by equation 2.6 with a fixed number of motors,n=N, showing the velocity at that number of motors. The curves labelled by f show the result of equation 2.16, where the x axis represents the maximum number of motors allowed to bind (n sums from 1 to N). In both cases, the leading motor only feels the load force. In our model, each motor can bind or unbind from the track at force independent dimensionless rates k_{on}= 5.0 and unbinding rate k_{off}=2.0. The other parameters used in plotting both sets of curves are forward stepping rate p = 2.0, backwards stepping rate q=1.0, energy barrier delta=0.5.

2.3 Force dependent unbinding

Molecular motors have been seen to have increased unbinding rates when pulling loads. Single Kinesins pulling loads held in by place by optical force clamps were shown in [37] to be more susceptible to unbinding, suggesting the ATP cycle is dependent on the load.

To introduce a force dependent unbinding rate to the model, the expression for k_{off} is modified so that it now depends on the dimensionless load force. If $k_{off}^{[0]}$ is the load independent unbinding rate, the force dependent unbinding rate expression is written as

$$k_{off}^{[L]} = k_{off}^{[0]}e^{f\delta}. \tag{2.17}$$

As the model considers that only a leading motor on a track is experiencing the load force, the unbinding rate is separated in to components for the leading and all other following motors. For n motors bound in a state, the unbinding rate for the cluster of motors is altered as

$$k_{off} \rightarrow \frac{1}{n}k_{off}^{[L]} + \frac{n-1}{n}k_{off}^{[0]}. \tag{2.18}$$

The new master equation for this system is then given by

$$\frac{dP_n}{dt} = k_{on}P_{n-1} + \left(\frac{1}{n+1}k_{off}^{[L]} + \frac{n}{n+1}k_{off}^{[0]}\right)P_{n+1} - \left(k_{on} + \frac{1}{n}k_{off}^{[L]} + \frac{n-1}{n}k_{off}^{[0]}\right)P_n. \tag{2.19}$$

with the steady state solution given by

$$k_{on}P_{n-1} = \left(\frac{1}{n}k_{off}^{[L]} + \frac{n-1}{n}k_{off}^{[0]}\right)P_n. \tag{2.20}$$

As before, the probability of being in a state with n motors bound where

$n \geq 1$ is now given by

$$P_n = \frac{\left(\frac{nk_{on}}{(n-1)k^{[0]}+k_{lead}}\right)^n \left(\frac{nk_{on}}{(n-1)k_{off}^{[0]}+k_{lead}} - 1\right)}{\left(\frac{nk_{on}}{(n-1)k_{off}^{[0]}+k_{lead}}\right)^{N+1} - 1} \tag{2.21}$$

.

The resulting effective velocity for a maximum of N motors is shown in figure 2.7. This figure shows the effect of increasing the load force felt by the leading motors while increasing the maximum number of available sites for motors to attach to.
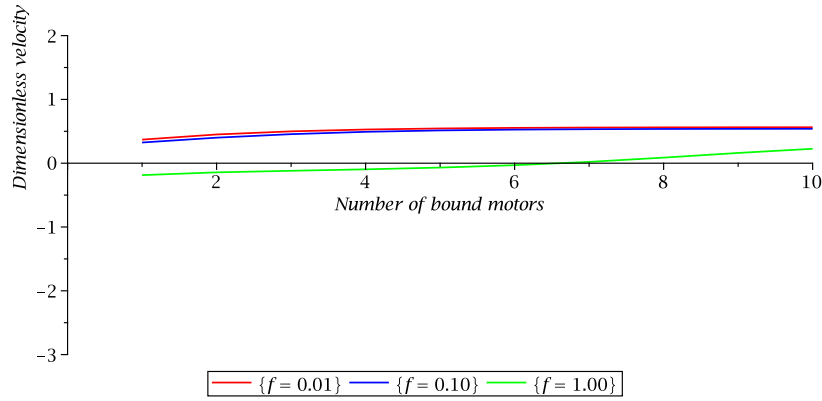
Figure 2.7: Dimensionless velocity against number of bound motors pulling varied dimensionless forces where the leading motors unbinding rate is now force dependent. The other parameters used are forward stepping rate p = 2.0, backwards stepping rate q=1.0, energy barrier delta=0.5, binding rate k_{on}= 5.0 and dimensionless unbinding rate k_{off}=2.0

2.4 Velocity dependent drag force

Often the cargo carried by molecular motors is in a fluid. For instance, the nucleus of a cell is moved around within the cytoplasm of the cell by micro-

tubules attaching to the nuclear envelope [35] with applications in various processes such as in the division of animal cells [3].

In the case of an object moving in a fluid, one might expect there to be a term in the force felt which is proportional to the velocity of the moving object, representing the drag force on the object opposing its motion. This is now added to the model by allowing the total force opposing felt by a leading motor to be given by

$$f_{tot} = f_{[0]} + f_{drag} = f_{[0]} + bv \tag{2.22}$$

where $f_{[0]}$ is the dimensionless, velocity independent force discussed previously, and b is a term which measures the relative contribution of the dimensionless velocity to the dimensionless force terms.
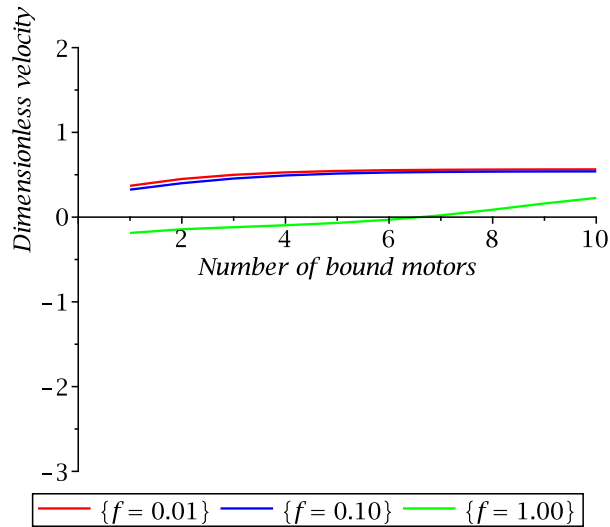
Figure 2.8: Dimensionless velocity against number of bound motors pulling varied dimensionless forces where the leading motors unbinding rate is now force dependent and the motor experiences a drag force proportional to the velocity. The other parameters used are forward stepping rate p = 2.0, backwards stepping rate q=1.0, energy barrier delta=0.5, binding rate $k_{on}=$ 5.0 ,dimensionless unbinding rate k_{off}=2.0 and drag coefficient b=1.0

Figure 2.8 shows the effect of allowing both a drag force and motors to

have a force dependant unbinding. Values of b on the order of magnitude 1.0 show no significant difference from figure 2.7. The results for b=1.0 are shown in this figure to demonstrate the effect of introducing a drag term.

The two main changes from the previous figure are that in all cases, the collective velocity of the motors is lowered, and in the dimensionless force $f_{[0]} = 1.00$ case, the number of motors required for forward motion decreases slightly to one fewer motors required for motion.

2.5 Multiple tracks with motors

Motors and filaments are capable of cooperative behaviour beyond the single track motion discussed so far. The simplest case would be a series of filamentous tracks aligned in parallel and with the same orientation of the barbed/pointed ends. This would allow a series of motors to collectively walk along separate filaments while pulling a load. If the force is shared equally between each of the T tracks with motors bound on each, then the force pulled by each motor only needs to be $\frac{f}{T}$, where f is the total force required for motion. Motors on multiple tracks could allow for motion where greater forces are required than the typical stall force of a molecular motor (on the order of pN). This could have applications, for instance, when motors are repositioning the nucleus rather than a smaller vesicle. In this simple model, the results of equations 2.6,2.16 and figures 2.6,2.7 would be altered by replacing any instances of the force f by the force divided by the number of tracks, $\frac{f}{T}$, and produce the same results otherwise. More complicated models involving tracks crossing, different alignments of tracks, allowing motors to step between different close tracks are all possible but are beyond the scope of the analytical work in this chapter.

2.6 Discussion and conclusions

In this section we have described an asymmetric particle model and applied it to the motion of molecular motors. We first introduced the basic model as detailed in [7], where predictions for the motion of a fixed number of motors were introduced. The model was then improved by allowing motors to unbind and bind to the track with fixed rates k_{on} and k_{off}. This allowed us to predict the effects of changing the number of motors on the collective speed. We then saw that in this model there was a decrease in the effective speed where the number of bound motors was significantly less than the force pulling capabilities of a single motor, and for a small force, the number of motors saturated for $k_{on} > k_{off}$, and returned to the effective speed with no binding processes.

Next, directed by the force dependence seen in experiments of motors pulling beads in optical traps, we allowed the unbinding rates to be force dependant, varying as $k_{off} = k_{off}^{[0]} e^{-f\delta}$. In keeping with the idea that only the leading motor feels any force from the load, the leading motor had the aforementioned unbinding rate, while the other motors kept the constant unbinding and all motors shared the same, constant binding rate. Again we saw as a result that the global maximum velocity decreased for large applied forces, while smaller forces had little effect on the collective motion.

Finally, we took in to consideration the surrounding medium which motors exist in. As the cytoplasm around the nucleus is typically fluid like, one might expect any motion of a organelle through the fluid to exert a additional drag force component on the organelle. This was included in the model by allowing there to be a term in the applied force proportional to the velocity at which the cluster of motors moves. As shown in figure 2.8, the effect of including the effects of a non zero drag coefficient can entirely prevent motion, compared to the prior cases where motion was slowed, but not entirely prevented. This implies that a significant component of any force in nuclear motion within cells is to enable motion through the surrounding medium.

Chapter 3

Nuclear deformation in two dimensions

3.1 Introduction

In this chapter, we look at the deformation of dendritic cell nuclei as the cells pass through channels containing constrictions. In section 3.2 we then introduce the method used to confine the cells, and the geometry of the channels used. Section 3.3 then describes the staining method used to image the cells, cell nuclei and the DNA within. Sections 3.4 and 3.5 then introduce the process we used to convert these images from raw data to a form appropriate to be used in our model of nuclear deformation. In section 3.6 we justify the treatment of the cell nucleus as an elastic object, and the Poisson's ratio used in our model. We then describe our model of the nucleus as a homogeneous elastic solid in section 3.8 and present our results.

3.2 Cell nuclei in confinement

The behaviour of cells and their nuclei in confinement is of interest for a number of reasons. Perhaps most importantly is that this has potential applications in identification of disease which affect the cells and/or nuclei, such as cancer. A cancer cell is metastatic when it is able to leave the current tumour and travel elsewhere in the body to form a secondary tumour. In order to leave an existing tumour, the cancerous cells typically enter in to the blood stream through a capillary, and then leave again at a later point [3]. This requires the cell and nucleus to deform on entry and exit to the blood stream. Understanding how this occurs could potentially lead to improved treatment of cancer. This has therefore lead to a number of studies looking at deforming cells and nuclei.

There are a number of ways to experimentally observe cell and nuclear deformation. These include for example the use of micropipettes, where nuclei are drawn in to a pipette [31], microfluidic devices where the nuclei pass through various geometries [8, 28], which can cause or allow nuclear deformations. The majority of this chapter focuses on modelling nuclei confined

within channels, as in figure 3.2. The principles can however be applied to any general elastic deformation. The channels and constrictions as shown in figure 3.2 are formed with three sides of Polydimethylsiloxane (PDMS) and the final side of glass, through which imaging occurs. A cartoon representation of the geometry of a segment of the channel is shown in figure 3.1. The xy plane of the confocal images taken as in figure 3.2 demonstrate the channel varying in width, y, in order to form constrictions through which a cell and its nucleus must deform to pass through. The size of the channel in the out of plane directions is also decreases from in the region of the constriction. In the channels used in these experiments provided by Matthieu Piel and Hawa Thiam [28], the dimensions of the channel (before and after the constrictions) are width $W = 7\mu m$, and height $H = 4.7 \pm 0.11$. The constrictions have a width $W = 2\mu m$, height $H = 3.43\mu m \pm 0.33\mu m$ and the length of the constrictions are $L = 20\mu m$ [28].
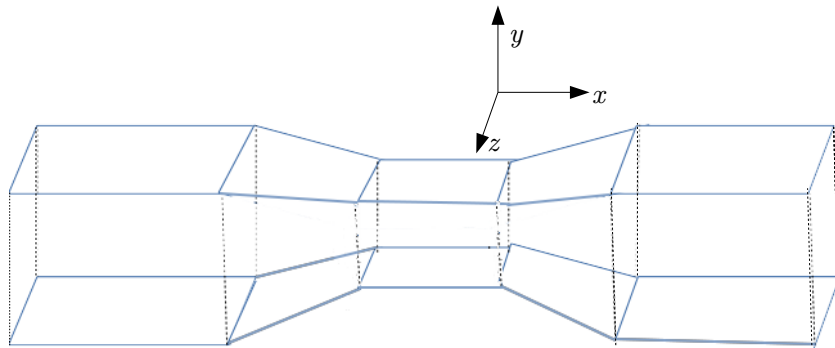
Figure 3.1: A cartoon of the channel with constriction geometry, showing a simple three dimensional representation of the channels formed in experiment by the group of Matthieu Piel [28]. The axes used in this chapter are as shown in the diagram, with x being the direction of motion along the channel and constriction, y being the in plane direction with a width $W = 2\mu m$ and the out of plane direction z, with height in the constriction $H = 3.43\mu m$.

3.3 Images of cell nuclei

One of the more common methods of investigating cells is the use of imaging. A usual method in live cell imaging is the use of fluorescent dyes to stain specific elements within a cell such as DNA or a chosen protein. Fluorescent labelling is used to identify the nucleus of the cell. The stained material then fluoresces, which can then be imaged using light microscopes.

In the context of imaging the nucleus, the two dyes typically used are Hoescht or DAPI (4',6-diamidino-2-phenylindole). Both of these dyes are used to stain the DNA within the nucleus. The two dyes vary in, among other things, emitted wavelength of light, as well as different toxicity levels depending on the cell. Both DAPI and Hoescht can be used in live cell imaging. The dye chosen typically depends on the resistance of the family of examined cells to the toxicity of the dye.

Another area of interest in fluorescent microscopy of the cell nucleus has been the nuclear lamins. The nuclear envelope includes the network surrounding the cell nucleus, including the nuclear lamina. The nuclear lamina is of particular interest in this thesis, as it is responsible for providing mechanical support to the nucleus. The main contributor to the stiffness of the nucleus is thought to be the lamin A family proteins within the lamina[23]. Through staining of both the DNA and lamins as a cell travels through a narrow constriction, it has been seen that the nuclear envelope can be ruptured, to allow for passage[28, 9].

3.4 Conversion of nucleus images to an outline

In order to determine the deformation field of a nucleus between frames of a video, we first convert the images of the nucleus such as figure 3.2 into a form useful for input in to our code. We do this by converting each
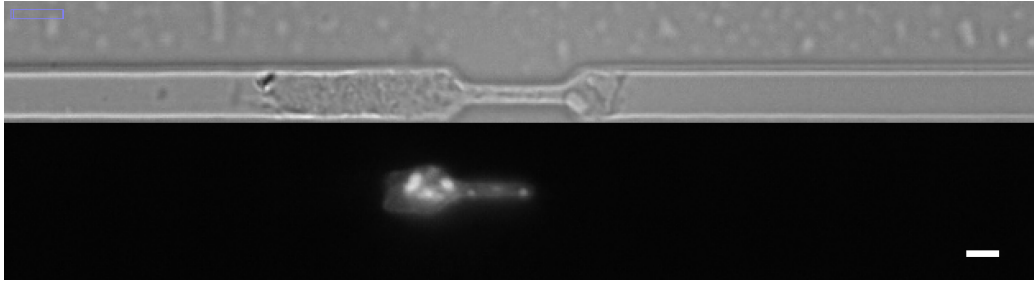
Figure 3.2: (Top) Confocal microscopy image of a mouse dendritic bone marrow cell, entering a constriction in a microfabricated channel. (Bottom) Fluorescent microscopy image of the nucleus of the same cell, stained with DAPI. Images provided by H Thiam and M. Piel. The scale bar is 4.3μm. The constriction width in this image is 2μm[28].

image of the nucleus in to an outline given by a list of coordinates using existing functionality of the image analysis software imageJ, with the method as follows.

We start by opening the video of the nucleus to be converted with imageJ. Then we use the "Set Threshold" tool to convert an image of the nucleus from a image where each pixel has a varying fluorescence in to a binary image where a pixel is either fluorescing or not. The dye used in the images show stained DNA, which we interpret from the binary images that fluorescing pixels represent the area within the nucleus, and that dark pixels are outside of the nucleus. The level at which the threshold is set is chosen for each video to be at the level before noise begins to appear in the form of scattered isolated fluorescing pixels in the background of the image, away from nucleus.

Once the threshold is set, using the analyse particles tool, also within imageJ, converts an entire video from the binary image in to an outline of all particles within the image. Since the nucleus is the only fluorescing object within the image, this provides a single curve in each frame, representing the edge of the nucleus in the two dimensional plane of the image. We then fit a cubic function to the curve using the magic wand and fit spline tools. The list of points on this spline is then exported to a text file for use as an input

file for each of the modelling steps which follow.

3.5 Averaging of different images

The curves drawn in section 3.4 can be noisy, and lead to irregularities in the calculation of the deformation field and related properties, as will be shown in section 3.12. In addition, each run of our model takes significant computation time. In order to analyse a larger set of images, rather than execute the model on each video frame individually, we looked at the average shapes of cell nuclei. This allows us to generate the average force required for the average typical deformation of a nucleus, while not requiring orders of magnitude increases in computational time.

First, each video frame is aligned approximately in time, by position relative to the channel entrance. This is so that images averages are generated using the nucleus at similar states. The chosen averages are the nucleus prior to entry (the frame before the nucleus begins deforming in to the constriction), the nucleus entering (chosen as the first frame where the nucleus begins deforming in to the channel), the nucleus entirely within the channel (the first frame where the rear of the nucleus completely passes the constriction entrance), the nucleus exiting (the first frame where the nucleus passes the constriction exit) and the nucleus after leaving the constriction (the first frame where the rear of the nucleus has moved past the constriction exit).

Then we use the outline of the nucleus in each video at one of the above shared time points to generate an average nucleus shape. The average shape is generated for each of the time points described previously by first finding each frame where the nucleus has the appropriate position relative to the channel constriction. This provides the list of outlines to use to generate the average shape from the various files, which are taken as described in section 3.4. The average outline is then generated by first repositioning each individual outline to have centre of mass at (0,0). Then in this reference

frame, spokes are drawn radially outwards from the centre of mass to the outline at fixed angular values, in order to find the average position at a list of angles. Spokes are placed every $\frac{2\pi}{n}$, where n is the average number of pixels making up the outline from all input shapes. Then the coordinates of each spoke at the same angle for each shape are summed up and divided by the number of input shapes to give the final average nucleus shape at each angle from all the nuclei at that time point.

3.6 Physical properties of the cell nucleus

The remainder of this chapter focuses on modelling nuclei that are confined within channels. The channels contain constrictions that are smaller than the cell nucleus, so that the nucleus is forced to deform in order to pass through the channels. The images used in the analysis here, as in figure 3.2, are provided by H. Thiam and M. Piel. these nuclei are moving through the channels without any external applied forces, such as an applied flow, neither is there a preferred direction of motion, such as through a chemotactic gradient. Any forces or deformations of the nucleus observed are therefore self generated by the cell observed. Our aim is to develop a mathematical model and software which can be used to analyse images of nuclear deformation such as figure 3.2. This analysis will determine the force fields applied to a nucleus for a given shape change observed between frames of a video. This could then allow for comparison with candidate force generation models in the future. To begin, in this section, we look at whether the nucleus undergoes any significant volume change, in order to help quantify the appropriate Poisson's ratio to be used in modelling the nucleus as an elastic object (see section 3.7 for justification of the treatment of the nucleus as an elastic object).

Figure 3.4 shows the change in area of cell nuclei as they travel along a channel and through a constriction. The nuclei are seen to undergo small variations in area as they travel along the channel in the absence of a constric-

(a)

(b)

(c)

(d)

(e)
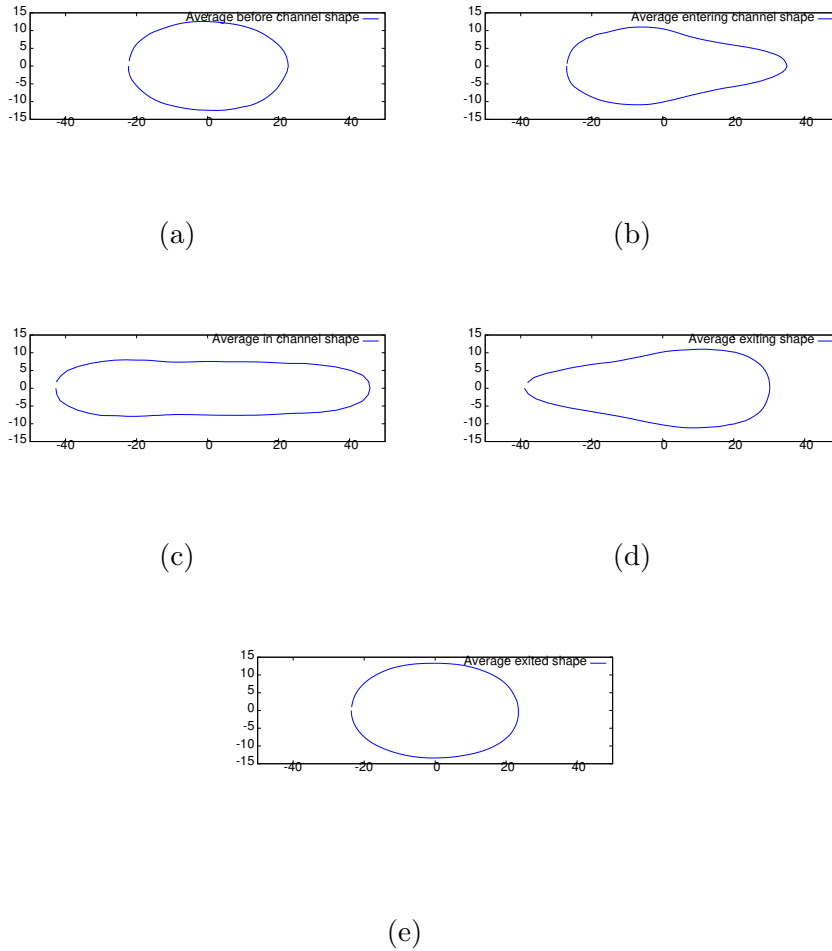
Figure 3.3: Average shapes of the dendritic cell nuclei as they pass through the channel constriction. Figure 3.3a shows the average nuclei shape from 71 images, just before the constriction, 3.3b as the nucleus begins entering the constriction from 56 images,3.3c while the nucleus is fully in the constriction from 71 images, 3.3d as the nucleus is exiting the constriction from 55 images, and figure 3.3e is the average shape of the nucleus after it has left the constriction from 71 images.

tion. Once a nucleus reaches a constriction it then undergoes a significant deformation in order to pass through the constriction. While undergoing
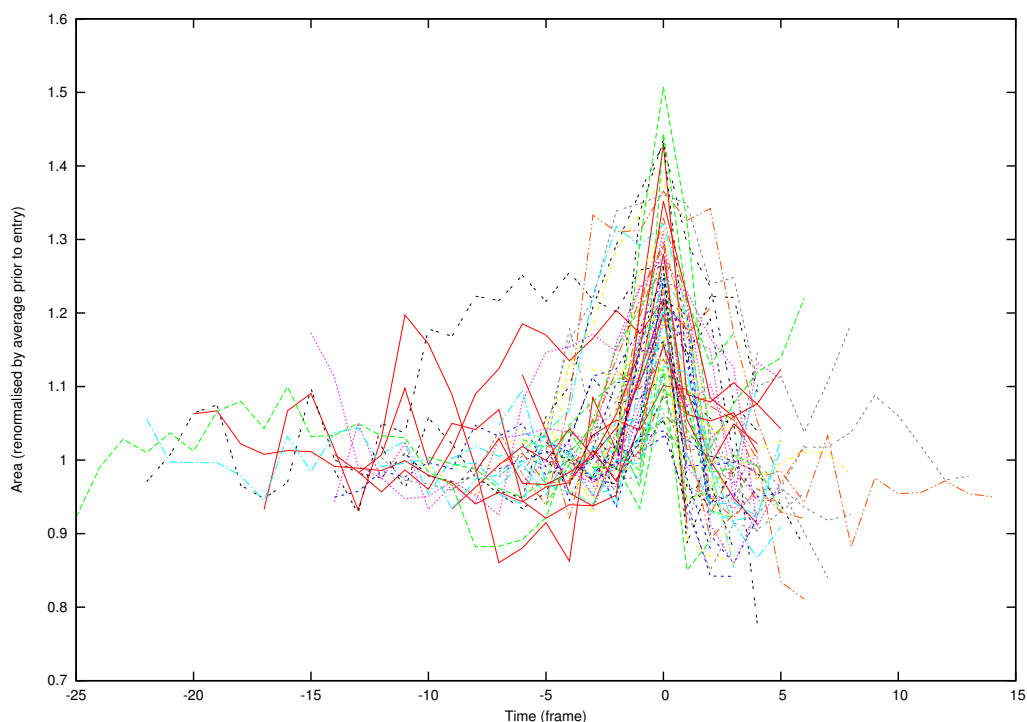
Figure 3.4: The relative area change of dendritic cell nuclei as travel through a channel of cross sectional shape $7\mu m$ by $5\mu m$ and they enter and travel through $2\mu m$ by $3.43\mu m$ constrictions. The area of each nucleus is rescaled by the average area of the cell nucleus prior to entering in to the constriction. The time axis is centred on the peak value of area. There is a significant area change as each nucleus encounters, deforms in to, and then exits a constriction.

deformation, the nucleus is seen to undergo a large increase in nucleus area, resulting in the peak seen in figure 3.4. Upon exiting the constriction, the nuclei then rapidly regain similar shapes and areas as seen prior to entry.

Figure 3.5 shows the profile of a cell nuclei while contained within the channel, prior to entering a constriction. Each slice of the image shows the cross section at a different height of the same nucleus. The nucleus is shaped in such a way that it fills the channel and constriction entirely in the out of plane direction, giving the same x-y profile at different heights.
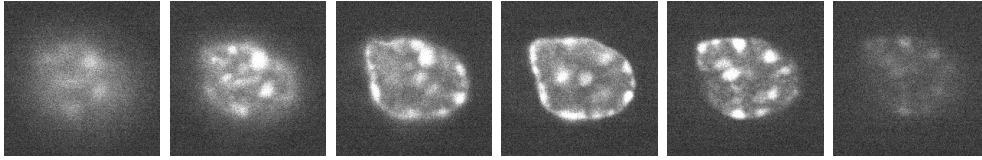
Figure 3.5: An example of the profile of one of the dendritic cell nuclei within a channel, but outside of any constriction. Each slice shows a different height of the same nucleus. The nucleus is shaped in such a way as to fill the channel in the Z direction.

We have established in figure 3.4 that there is an area change in the images of the dendritic nuclei. If the nuclei change volume as they pass through the channels, the volume change can be used to determine the Poisson's ratio of the nuclei. We now use these images of nuclei passing through the constrictions to calculate if there is any measurable volume change of these nuclei.

To determine whether there is any measurable volume change of the nuclei as they pass through the constriction, we calculate an estimate of each nucleus volume. The channel cross section dimensions (width in plane × height out of plane) are $7\mu m \times 4.7\mu m$ outside the constriction, and$2\mu m \times 3.43\mu m$ inside the constriction. The total volume of the nucleus is measured by calculating the area of the nucleus within the constriction and outside of the constriction to find two area values, A_{in} and A_{out}. The two values are then multiplied by the heights of the constriction, h_{in} and h_{out} respectively. This method of estimating the nucleus volume assumes that the nucleus fills the channel in the out of plane direction, both inside and outside of the constriction. This is motivated by images such as those in 3.5 whereby the nucleus profile is minimally changed between different z stacks representing different heights of the same nucleus.

Figure 3.6 shows the mean volumes of each nucleus, where the mean is calculated over all frames at that position relative to the constriction. The three time points are 1) before the nucleus enters the constriction, 2) while

any part of the nucleus is between the constriction entry and exit, and 3) after the nucleus has exited the constriction. Figure 3.7 shows the volumes rescaled by the mean volume of the given nucleus before entry, at the same time points as in 3.6.

There is no clear pattern of volume increase or decrease in either of these graphs. In addition, there is no statistical difference between the mean volumes over all the nuclei before the constriction $(240 \pm 90)\,\mu m^3$, in the constriction,$(223 \pm 67)\,\mu m^3$ or after the constriction $(235 \pm 57)\,\mu m^3$.
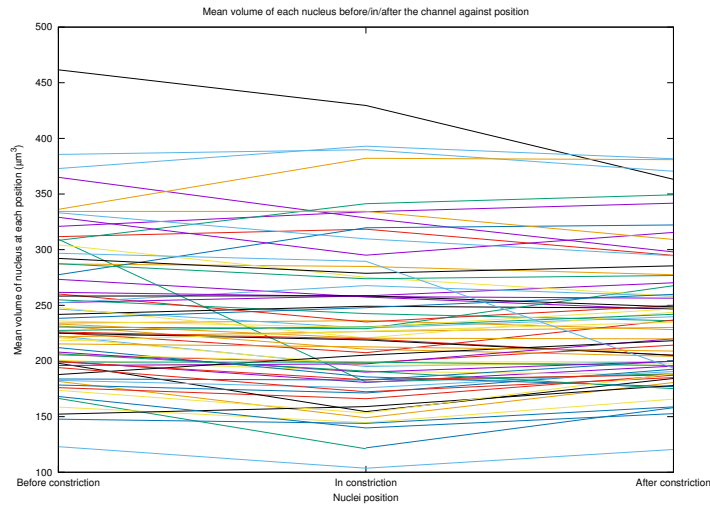
Figure 3.6: The mean volume of each nucleus in μm^3 before the constriction, inside the constriction and after the constriction. Each mean value is calculated using every frame in the corresponding position of the nucleus relative to the constriction.

Another method to determine whether there is any volume change of the nucleus within the channels is to observe the density of DNA within the cell. As DNA is the most dense component within the nucleus, observing how the density of the DNA changes with position in the channel could indicate if there are any significant volume changes. If the nucleus does increase in volume, the average density of materials within the nucleus, including the DNA should decrease by more than the change in the dimensions of the
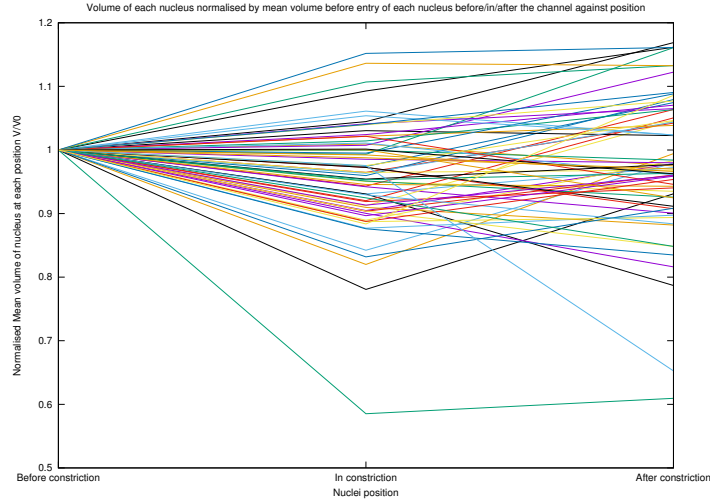
Figure 3.7: The mean volumes of each nucleus, renormalised by the mean volume of the nucleus before entry in to the constriction. Each mean value is calculated using every frame in the corresponding position of the nucleus relative to the constriction.

channel in to the constriction and vice versa if the nucleus is compressed.

In order to measure the average intensity of fluorescing pixels, the background of the images considered must be removed. This was done using the existing software within imageJ, which uses a "rolling ball" method, in order to remove the background of images [34]. However, as in the example shown in [34], this typically leaves the background as pixels with small, but non zero values of fluorescence. In order to accurately count the number of fluorescing pixels, these must not be counted when computing the mean intensity value.

To do this, the average intensity of all the pixels in a given image is calculated. The mean value and standard deviation of the fluorescence of the pixels is then calculated. Then each image is decreased by an amount given by

$$I_{new} = I_{old} - \tilde{I} - a\sigma \tag{3.1}$$

where I_{new} is the intensity with the background removed , I_{old} is the intensity

with background, $\tilde{I}$ is the mean intensity of all pixels, σ is the standard deviation of the intensities and a is a value that is dependent on the image. The value of a is increased in increments of 0.1 from 0, until the number of fluorescing pixels matches that of the area of the curves around the nuclei, which were previously drawn by hand, using the threshold tool and selection tools within imageJ, for each given image and frame.
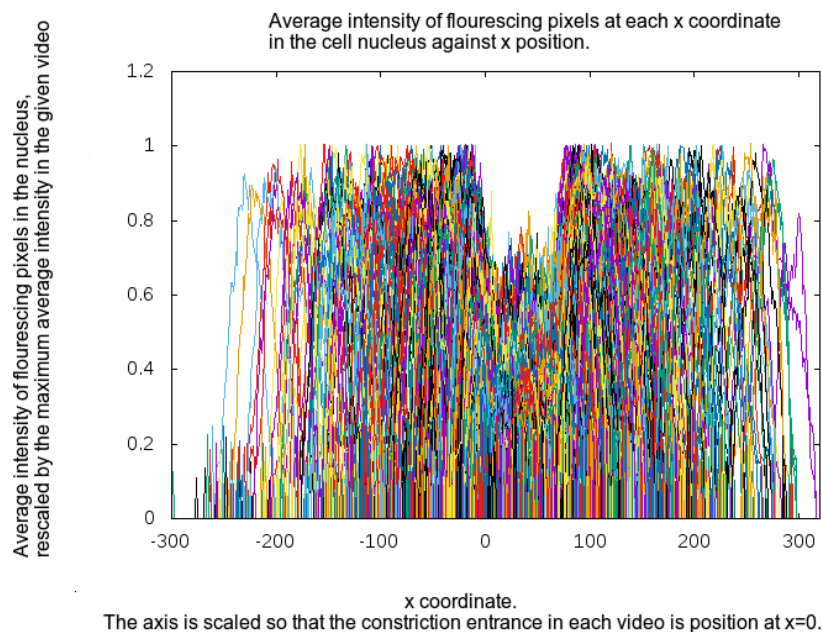
Figure 3.8: The average intensity of fluorescing pixels against position of 80 cell nuclei travelling through channels containing constrictions. The constriction entrance in each video is positioned at x=0. Each video of a nucleus is renormalised by the maximum value of average intensity seen in the video.

The change in DNA intensity at each x coordinate as shown in figure 3.8 to between $60-70\%$ is also consistent with the change in height of the channel from $5\mu m$ outside of the constriction to $3.43\mu m$ within the constriction, i.e.

the constriction is approximately 70% of the height of the channel.

As shown by the results demonstrating no measurable volume change and DNA density changes consistent with the changes in height of the channel and constriction , we treat the nucleus as an incompressible elastic material with Poisson's ratio of $\nu = 0.5$ for the remainder of this chapter.

3.7   Continuum elasticity relations

In this thesis, the nucleus is treated as an elastic object, as assumed for example by [6, 17]. This is motivated by the fact that the cell nucleus has been seen to display a significantly more elastic response to applied forces than the surrounding cytoplasm in micropipette aspiration experiments [31, 18]. These experiments occur over a time scale of minutes. This is a similar time scale as the experiments of nuclei entering to channels. This justifies the assumptions that the nucleus on these time scales is elastic and not viscoelastic. The mechanical properties of the nucleus have also been investigated using atomic force microscopy. The indentations observed, caused by small applied forces demonstrate that the nucleus is stiffer than surrounding cytoplasm [25]. In the microchannel experiments analysed below, the nucleus is seen to regain its original shape after exiting a constriction, implying it is behaving elastically.

In order to describe the nucleus behaviour a continuum approach is used, justified by the relevant properties of the nucleus as a whole on length scales much larger than the constituent molecules.

The standard constitutive equation for a continuum linear elastic solid obeying Hooke's law is given by [24]

$$\sigma_{ij} = \frac{E}{1+\nu} \left(u_{ij} + \frac{\nu}{1-2\nu} u_{kk} \delta_{ij} \right) \tag{3.2}$$

where σ_{ij} is the stress tensor, E is the Young's modulus, ν is Poisson's ratio

and u_{ij} is the strain tensor. The subscripts label tensor elements and δ_{ij} is the Kronecker delta function. Repeated indices use the standard Einstein summation convention. The strain tensor is defined by:

$$u_{ij} = \frac{1}{2}\left(\frac{\partial u_i}{\partial x_j} + \frac{\partial u_j}{\partial x_i} + \frac{1}{2}\frac{\partial u_k}{\partial x_i}\frac{\partial u_k}{\partial x_j}\right) \tag{3.3}$$

where u_i is the displacement and x_i is the position vector. In chapter 5, to compare with published data, we use the linear version of this strain tensor, which is only valid for small deformations, while in this chapter we use the full expression, as the nonlinear terms are not negligible here. The free energy density, f, of a deformed elastic solid expressed in terms of the strain, u_{ij}, and stress tensors ,σ_{ij} is given by ([24]);

$$f = \frac{1}{2}\sigma_{ij}u_{ij}. \tag{3.4}$$

The traction force is defined as the external force on a unit area of the surface of a body. For an elastic object it is given by ([24]);

$$t_i = \sigma_{ij}n_j, \tag{3.5}$$

where n_j represent the components of the normal to the surface.

3.8   Nucleus as a homogeneous elastic solid

We consider two models of the nucleus in this thesis. In this chapter, we treat the nucleus as a homogeneous elastic solid, and in a later chapter as a thin elastic shell.On a simple level, the nucleus is an envelope (the nuclear membrane and lamina) surrounding the water, DNA and associated proteins within. The nuclear lamina consists of nuclear lamins of the families A/C and B1/B2. The lamin A/C families are known to give the elastic response to the nucleus, while B family lamins do not contribute significantly [23].

The response of the internal elements however are not so clear. The DNA is tightly packed within the nucleus, by wrapping the chromosomes tightly around histones to a fraction of the uncompressed volume. In this section we treat the internal elements as an elastic solid with the same properties as the nuclear lamina.

In order to treat the nucleus as an elastic solid, the deformation field within the nucleus must be defined. The deformations are considered around the centre of mass reference frame of the nucleus. Physically, this means that the centre of mass has no deformation between any two given images, i.e. the deformation field at $(0, 0, 0)$ is $(u_x, u_y, u_z) = (0, 0, 0)$. The deformation field of the rest of the body is defined such that it is a function of the deformation of the nucleus boundary. In the model defined here, the deformation field is assumed to decrease linearly to zero from each boundary point towards the centre of mass.

In order to accommodate the assumption of a deformation field decreasing lineally along the radial direction, the calculations of derivatives in this model are performed using polar coordinates in the 2d plane seen in images. However, the coordinates and deformation fields read in and calculated are known in Cartesian coordinates. In order to minimize computation time, these derivatives are calculated as given below, using the forms of numerical derivatives for varying spatial positions between mesh points.

$$\frac{\partial u_x(x_{(i,j)}, y_{(i,j)})}{\partial r} = \frac{u_x(x_{(i,j+1)}, y_{(i,j+1)}) - u_x(x_{(i,j-1)}, y_{(i,j-1)})}{r_{(i,j+1)} - r_{(i,j-1)}} \tag{3.6}$$

$$\frac{\partial u_y x_{(i,j)}, y_{(i,j)}}{\partial r} = \frac{u_x(x_{(i,j+1)}, y_{(i,j+1)}) - u_x(x_{(i,j-1)}, y_{(i,j-1)})}{r_{(i,j+1)} - r_{(i,j-1)}} \tag{3.7}$$

$$\frac{\partial u_x^{(i,j)}}{\partial \theta} = \frac{R_{i+1} u_x^{(i+1,j)} \Delta\theta_i - R_{i-1} u_x^{(i-1,j)} \Delta\theta_{i+1} + u_x(x_{(i,j)})((\Delta\theta_{i+1})^2 - (\Delta\theta_i)^2)}{\Delta\theta_{i+1} \Delta\theta_i (\Delta\theta_i + \Delta\theta_{i+1})}$$

$$\tag{3.8}$$

$$\frac{\partial u_y^{(i,j)}}{\partial \theta} = \frac{R_{i+1} u_y^{(i+1,j)} \Delta\theta_i - R_{i-1} u_y^{(i-1,j)} \Delta\theta_{i+1} + u_y(x_{(i,j)})((\Delta\theta_{i+1})^2 - (\Delta\theta_i)^2)}{\Delta\theta_{i+1} \Delta\theta_i (\Delta\theta_i + \Delta\theta_{i+1})}.$$

$$\tag{3.9}$$

$$\tag{3.10}$$

Where R_{i+1} is the ratio of the radius at point $i + 1$ to the radius at point i. Similar expressions are used for the innermost and outermost shapes, but replaced with forward/backward finite difference methods respectively.

The factors of R_i in the latter two equations are included to scale for small variations in the radius between points.

These equations, together with the standard relations between Cartesian and polar coordinates allow the strains to be numerically evaluated from equation 3.3 in the Cartesian coordinate basis directly.
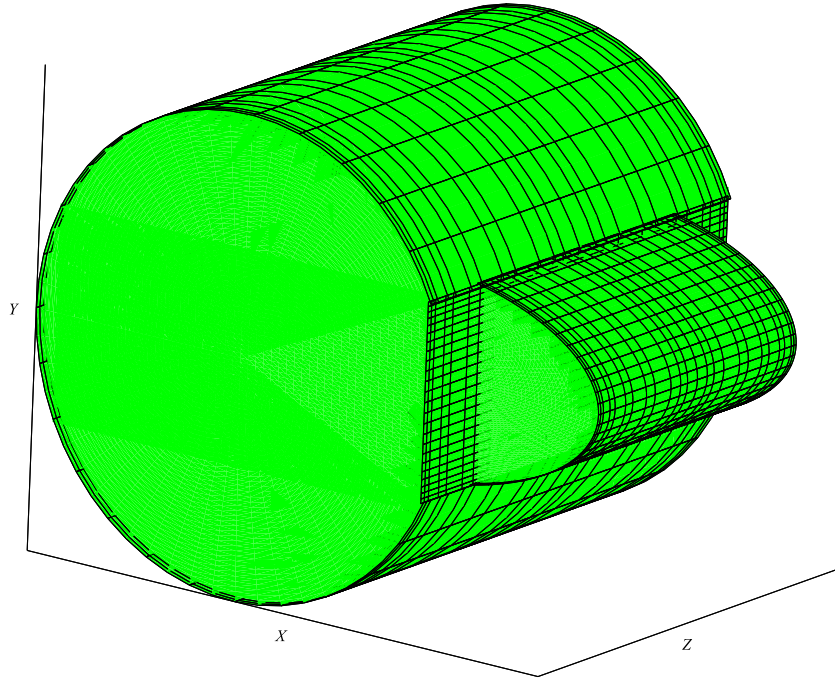
Figure 3.9: Cartoon of the nucleus shape in a channel. The cartoon shows a nucleus beginning to deform as it enters in to a constriction within the channel, forming a protrusion. The cartoon represents the shape of the nucleus as it enters in to the constriction. Here, the nucleus decreases in height (z) by a fraction $\frac{3.3}{5.0}$, as in the data for the constrictions used in this chapter.

3.9 Strain components in the third direction

Figure 3.5 shows that the cell nucleus contained in a channel has the same cross section at different heights (z). We assume that the outlines of cell nuclei that that can be seen in the images (such as figure 3.2) represent the central plane of the nucleus. Therefore we assume that the nucleus curvature in the z direction is zero, both within the channel and inside the constriction. These assumptions mean that, prior to entering the channel, the nucleus has zero curvature in the out of plane direction with the same cross section at each height as shown in figure 3.9. When inside the constriction, we assume that the nucleus still has the same cross section as seen in the single plane

observed in the out of plane direction, up to the new, smaller constriction height. This approximation that the nucleus has the same cross section throughout the entire channel and/or constriction is used for the nucleus at all time steps.

Rather than calculating the strain from a known deformation as in the xy plane, we treat these nuclei as incompressible elastic materials. For an incompressible material, the strain in the out of plane direction is defined by the incompressibility condition that the trace of the strain tensor must be zero for a incompressible material. In this case that means that the strain component in the out of plane direction, zz is

$$u_{zz} = -(u_{xx} + u_{yy}) \tag{3.11}$$

Since the deformation in the out of plane direction, u_z, varies only along the channel direction, x, under these approximations, the strain component in the yz direction is given as

$$u_{yz} = u_{zy} = \frac{1}{2}\left(\frac{\partial u_y}{\partial z} + \frac{\partial u_z}{\partial y} + \frac{\partial u_k}{\partial y}\frac{\partial u_k}{\partial z}\right) = 0. \tag{3.12}$$

The deformation in z changes with the x direction at the entrance and exit of the constrictions. The deformation in z is therefore proportional to Heaviside functions, and the change in height of the channel to the constriction. The deformation in z can be written using four Heaviside functions to give a deformation of $L_z^{con} - L_z^{chan}$ on entering, and $L_z^{chan} - L_z^{con}$ on exiting as:

$$u_z = \left(L_z^{con} - L_z^{chan}\right)\left(H(x_i + u_x - x_{ent}) - H(x_i - x_{ent}) + H(x_i - x_{exit}) - H(x_i + u_x - x_{exit})\right)Az. \tag{3.13}$$

Where $H(x)$ are Heaviside functions, L_z^{con} is the height of the constriction, L_z^{chan} is the channel height, x_i is the x position of a point on the undeformed

shape, u_x is the deformation along x that point undergoes, and x_{ent} and x_{exit} are the entrance and exit x positions of the constriction entrance and exit respectively. The combination of the first two Heaviside terms returns a value 1 if the point x_i is outside the constriction, and $x_i + u_x$ is inside the constriction. Similarly, the second two terms return a value of -1.0 if the nucleus goes from inside the constriction to outside. In order to meet the incompressibility condition, A is a position dependent value given by

$$A = \frac{-u_{xx} + u_{yy}}{\left(L_z^{con} - L_z^{chan}\right)\left(H(x_i + u_x - x_{ent}) - H(x_i - x_{ent}) + H(x_i - x_{exit}) - H(x_{exit} + u_x - x_i)\right)}$$
$$(3.14)$$

which simplifies the expression of u_z to

$$u_z = -(u_{xx} + u_{yy})z. \tag{3.15}$$

so that the incompressibility condition is met.

Using the first form of the expression for u_z gives the final components of the strain as

$$u_{xz} = u_{zx} = \left(L_z^{con} - L_z^{chan}\right)\left(\delta(x_i + u_x - x_{ent}) - \delta(x_i - x_{ent})\right.$$
$$\left. + \delta(x_i - x_{exit}) - \delta(x_{exit} + u_x - x_i)\right)Az.$$

As the images represent the central plane of the nucleus within the channel, for $z = 0$, this gives

$$u_{xz} = u_{zx} = 0. \tag{3.16}$$

While in general a non zero σ_{zz} stress term exists, the curved surface of the nucleus is defined so that its normal is perpendicular to the $\hat{z}$ direction. Therefore the σ_{zz} term does not contribute to the traction force on the surface seen in images. The traction force on the central plane can then be solved based on the two dimensional problem, as the traction over the central plane

is unaffected by the edges.

3.10 Simulated annealing to determine deformation fields.

In order to determine the deformation field between two images of cell nuclei, the nucleus must be tracked from image to image. One common method to determining the deformation fields between images is by following known 'landmarks' in the images [38, 27]. A landmark is a recognisable area that can be used to determine a local deformation field. The global deformation field is then extrapolated from the local deformation of landmarks. However, due to the complex nature of the nucleus deformation field, together with the limited resolution currently resolvable, means there are no consistently reliably identifiable landmarks in the DAPI stained images of the nucleus described above. A different approach is needed in order to determine the deformation field, and subsequently all values calculated from the deformation fields between images.

As there is no direct way to currently observe the deformation of given elements of the nuclei between a series of DAPI stained images such as figure 3.2, due to the limits in spatial and temporal resolution, there is no unique mapping between two images of nuclei. Instead we determine the deformation field through an energy minimisation simulated annealing routine. That is, we seek the mapping that minimises the free energy of the deformation,given by equation 3.4, and we assume that this mapping describes the physical deformation the nuclei undergoes. In addition, to minimise computational time, we only calculate the deformation field for the outline of the nucleus from each image. Then where necessary, the deformation field for any elements inside the nucleus we extrapolated from the deformation of the boundary as described below.

An image such as 3.2 is be converted in to an outline as described in

section 3.4. Then with two such outlines, we can calculate the deformation field between the two outlines. For example this can be applied to two sequential frames from a video of images such as figure 3.2, where the nucleus deforms between the first and second images.

In this case, we refer to the first image as the source image and the second as the target image. Initially we set the deformation field between the source and target image boundaries as a somewhat arbitrary mapping between the source and target image boundaries to obtain an approximation of the deformation field. This mapping is chosen by assuming that elements that make up the boundary maintain sequential order during any deformations and that initially, each pixel from the source boundary shape ends up on a pixel on the target shape. We then refine the deformation by using a simulated annealing approach to minimise the free energy of deformation.

To define the arbitrary mapping, the input lists of the boundary and target coordinates are remeshed, so that each list has the same number of elements, chosen to match the number of points on the input target shape. That is, the number of points on the source shape are either increased or decreased by adding or removing points respectively. The resulting curve representing the source shape has the same number of points as the target shape, evenly spaced in angular position.

The arbitrary initial mapping is then determined by setting each point on the target to map to one of the points in the source, such that the combination has the lowest possible starting energy of mappings between these points.

The deformation field is then perturbed to find configurations with lower free energy. An element of the source shape is chosen at random by generating a random number between 0 and the number of points on the surface. The deformation field is then perturbed by moving this element towards one of its nearest neighbours along a straight line on the source boundary. The chosen element then has a direction of perturbation chosen at random, forwards or backwards along the curve, and is then perturbed a tenth of the distance

towards the chosen neighbour.

The energy of the new configuration is calculated. If the free energy of deformation decreases, the new deformation location is recorded as a new minimal energy configuration. If the free energy increases the energy by an amount ΔE, the configuration is kept if the energy change when compared with $\exp(-\frac{\Delta E}{k_b t})$ is greater than a randomly generated number between 0 and 1. If not, then the change is discarded, and a new perturbation performed, as in standard simulated annealing procedures, which can are described in more detail in[22, 14].

3.10.1 Alignment of the nucleus to remove translation

In order to define the deformation field between two images of cell nuclei under motion, we must choose a point to register the images. Initially we consider two cases, firstly where the centre of mass of the nuclei are aligned by the centres of mass, and then where the nuclei are aligned by the rearmost or forwardmost point of the nucleus. The distinction between the two cases is important, as it changes the deformation field at all points along the surface of the nucleus. This in turn affects the strain through the assumption that the deformation field drops linearly to zero at the centre of mass and therefore stress and traction forces, as well as the Poisson's ratio if we choose to calculate it (see later chapter 5) using the found deformation field.

The aim is to remove the force free translational motion of the nuclei between the two images, so that the deformation field calculated is only that of the shape change of the nuclei. For the first case we look at, the nucleus is aligned by placing the centre of mass of each nucleus at the origin. This was chosen to remove any extrinsic motion of the nucleus from the deformation field calculations, and physically represents a deformation of an object fixed in place at the centre of mass. To align the nucleus images around the centre of each of their masses, we calculate the centre of mass of the nucleus using the input outline of the nucleus. When the polygon forming the nucleus

outline consists of N points, the approximation to centre of mass of a general
polygon is given by

$$(x_c^j, y_c^j) = \frac{1}{6A} \sum_{i=1}^{N} ((x_i y_{i+1} - x_{i+1} y_i)(x_i + x_{i+1}, y_i + y_{i+1})). \qquad (3.17)$$

where (x_c^j, y_c^j) are the coordinates of the centre of mass of frame j of the
video, A is the area of the polygon, and (x_i, y_i) are the coordinates of each
pixel on the boundary making up the polygon representing the nucleus, and
the surface of the polygon is a closed loop such that the final point N connects
directly to the point i=1. The nuclei are then aligned by setting the centres of
mass of the shapes representing the nuclei between sequential shape changes
to be equal. i.e. for a single video, the the shapes observed in two sequential
frames j and $j+1$ where frame j represents the undeformed shape and $j+1$
represents the deformed shape, would have the centres of masses aligned by

$$(x_c^j, y_c^j) = (x_c^{j+1}, y_c^{j+1}). \qquad (3.18)$$

Each point in the corresponding frame j is then redrawn around the centre
of mass by subtracting the value of the centre of mass from every point in
the polygon. This shifts the shape along the x and y axes by $-(x_c^j, y_c^j)$. This
is repeated for the frame being deformed to $j+1$ as well, with the centre of
mass (x_c^{j+1}, y_c^{j+1}), so that both the undeformed frame and deformed frames
have centres at the origin $(0,0)$. The deformation field and all fields derived
from it can then be calculated for the centre of mass aligned shapes.

For the second case, the nucleus is now aligned by the rearmost (or for-
wardmost) point of the outline. This was chosen to better represent the
deformation field on entry in to a constriction, where the of the motion in
the laboratory frame is of the leading edge of the nucleus deforming as it
enters in to a constriction. Comparatively, the rear edge moves forward less
than the front edge, meaning it has relatively smaller motion compared to

the leading edge. Given this behaviour on entering in to constrictions, it is likely that the nucleus deformation will be better approximated by this approach instead of the centre of mass method described above, as this will provide minimal deformation to the rear of the nucleus and larger deformations towards the front in to the channel, and leads to larger forces generated at the leading edge. This is discussed in more detail in section 3.10.2

The rearmost point of the nucleus is found by iterating through each point on the surface of the polygon approximating the nuclear shape, and taking the point with smallest x_i as the nucleus moves from left to right through the channel (the largest x_i is used if the nucleus is moving in the opposite direction). Once the smallest value of the x coordinate is found, at point (x_s^j, y_s^j) for image j, the two images j and $j+1$ are aligned by setting the values of the rearmost points equal, i.e.

$$(x_s^j, y_s^j) = (x_s^{j+1}, y_s^{j+1}). \tag{3.19}$$

This is done by repositioning the two shapes are then as in the first case, by shifting the polygons so that the respective rears of the shapes, are placed at the same location in space $(x_s^j, y_s^j) = (x_s^{j+1}, y_s^{j+1})$. The undeformed source shape is placed so that the centre of mass is still at the origin, $(x_c^j, y_c^j) = (0,0)$, i.e. the points on the undeformed shape are shifted by (x_c^j, y_i^j), where (x_c^j, y_c^j) is the centre of mass of the undeformed shape. Then the deformed target shape is placed so that the rear of the target shape in the centre of mass configuration is at (x_s^j, y_s^j) in the frame of the undeformed shape. This means that the deformed shape is moved by $(x_s^{j+1}, y_s^{j+1}) - (x_s^j, y_s^j) - (x_c^{j+1}, y_i^{j+1}))$, i.e. the deformed shape is placed at its centre of mass, and then shifted along the x axis so that the rear is aligned with the undeformed shape.

The deformation fields are then calculated with the shapes now aligned by the rear most points on the two shapes.

3.10.2 Alignment of undeformed and deformed nuclear shapes

In section 3.10.1, we described two limiting models of the relative positioning of the nuclei in the source and target shapes. The relative position where translation is removed from the images is likely to be between the two limiting cases described in that section. However the limits on both the spatial and temporal resolution of the nuclei in the images prevent the translation component of the motion from being identified precisely from any given series of images. There are limitations as to how often an image of the cell nucleus can be captured, meaning that we do not see the nucleus position at the same point in space relative to the constriction in each video. As a result, the positioning of the nucleus generally falls in to one of five broader positions (before the constriction, entering in to the constriction, inside the constriction, leaving the constriction and after the constriction). Consequently, direct observation of the nucleus deformation between frames of the video is problematic. Due to the spatial limitations, it is also not possible to identify any landmarks within the nucleus which could be used to determine the deformation of the entire nucleus.

In order to estimate the location where the deformed nucleus should be placed relative to the undeformed nucleus, we measured how the position of the front and rear of the nucleus changed between frames. Measurements of the change in the front and rear change position of each nucleus were taken between frames at each of the five positions (before the constriction, entering in to the constriction, inside the constriction, leaving the constriction and after the constriction).

Figure 3.10 shows the changes in position of the rear of each nucleus, against the change in position of the front of the same nucleus, with a linear fit of the form $y = mx + c$. The gradient of the lines of best fit, as shown in each of the graphs, provides an estimate of the how far the front position of the nucleus will move, given a change in the rear position, or vice versa.
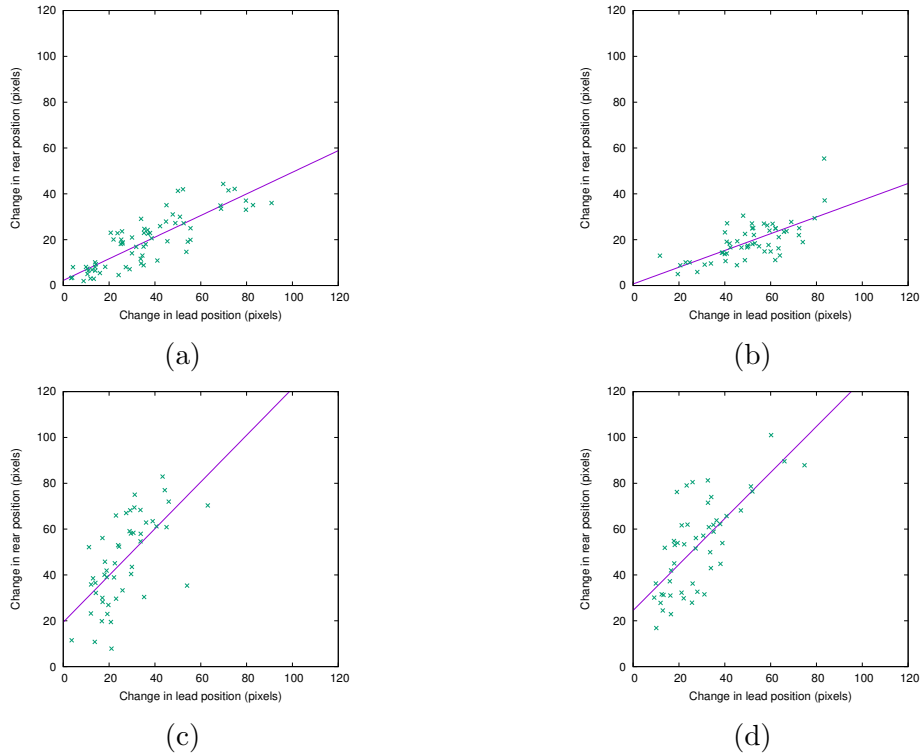
Figure 3.10: These figures show the change in the rear position of each nucleus against the change in leading position of the same nucleus. Each point in each of the graphs represents one nucleus. (a) shows the changes as the nucleus moves from before the constriction to beginning to enter the constriction. (b) shows the changes from when the nucleus is entering the constriction, to when it is fully in the constriction. (c) shows when the nuclei are moving from in the constriction to leaving the constriction. Finally, (d) shows the nucleus as they go from leaving the constriction to having fully exited the constriction. The best fit lines in each image are for (a): $y = 0.47(\pm 0.04)x + (2.23 \pm 1.48)$, for (b): $y = 0.37(\pm 0.05)x + 0.68(\pm 2.81)$, for (c): $y = 1.02(\pm 0.18)x + 19.4014(\pm 5.179)$ and for (d): $y = 1.00(\pm 0.1375)x + 24.52 \pm 4.38$.

The intercept with the y axis measures how much the rear of the nucleus will move when the front of the nucleus does not change position. The y intercept is near zero in figures 3.10a and 3.10b, consistent with the nucleus

being unable to move the rear without the front of the nucleus deforming as it entering the constriction, as the out of plane direction is already filled by the nuclei volume. In figures 3.10c and 3.10d, the y intercept is larger than from zero, representing the nucleus filling the volume in the out of plane direction and unlike the entry position the nucleus can move freely into the larger space post-constriction.

The gradient provides an estimate of where the point of zero deformation should be between each average deformation of the nucleus. The nuclei are initially aligned by the centres of mass, and then shifted an amount along the x axis, to reflect the change given by the ratio of the change in position of the rear to the change in position of the front of the nuclei. As the nuclei are orientated so that they all move in the positive x direction, the value of the ratio is always positive. If the ratio of the change in the rear position to the change in the front position, m, is $m \geq 1$, then the rear moved more than the front, and the target nucleus shape is shifted forwards in space relative to the undeformed nucleus. Vice versa if the ratio is in the range $0 \leq m \leq 1$, then the nucleus is shifted in the opposite direction.

The distance that we shift the entire target shape along x is proportional to the relative change in the rear or front position compared to the sum of the changes to the rear and the front in the respective directions. The proportion of the distance to move in the given direction is

$$\frac{\Delta r - \Delta f}{\Delta r + \Delta f} = \frac{m - 1}{m + 1} \tag{3.20}$$

where Δr and Δf are the changes in the rear/front of the nucleus position between the undeformed and deformed shapes when aligned in the centre of mass frames respectively. The values used to shift each target shape are given in table 3.1.

Position	Gradient	Shift of nucleus position from centre of mass
Before to entering	0.47	$-0.36\lvert\Delta r\rvert$
Entering to in	0.37	$-0.46\lvert\Delta r\rvert$
In to exiting	1.02	$0.01\lvert\Delta f\rvert$
Exiting to out	1.00	$0.00\lvert\Delta f\rvert$

Table 3.1: The changes in position used to shift the target shape. Δr and Δf represent the changes between the rear and front position of the nuclei respectively, in the centre of mass frame.

3.11 Solid nucleus model results and discussion

We present here the results of the traction force calculations for the dendritic cell nuclei travelling through channels and entering in to constrictions for three different methods of alignment. First, the traction forces are found for nuclei aligned by fixing the centre of mass of the nuclei. Then for nuclei where they are fixed at the rearmost point of the nucleus between images. Finally, we look at the case where the nuclei are aligned at a point within the nucleus, determined from the difference between the distances the front and rear of the nuclei move during deformation. The aim of each of these different alignment choices is to remove translation from the images, and find the forces which cause the deformation of the nucleus.

3.12 Traction force using a single nucleus video

In section 3.5, we discussed the importance of using an average nucleus shape instead of any single image of the nucleus. Figure 3.11 shows the deformation and traction fields using images of a single nucleus, as it begins to enter a constriction. As defined in section 3.7, the traction force is the results of taking the product of the calculated stress tensor and the normal vector
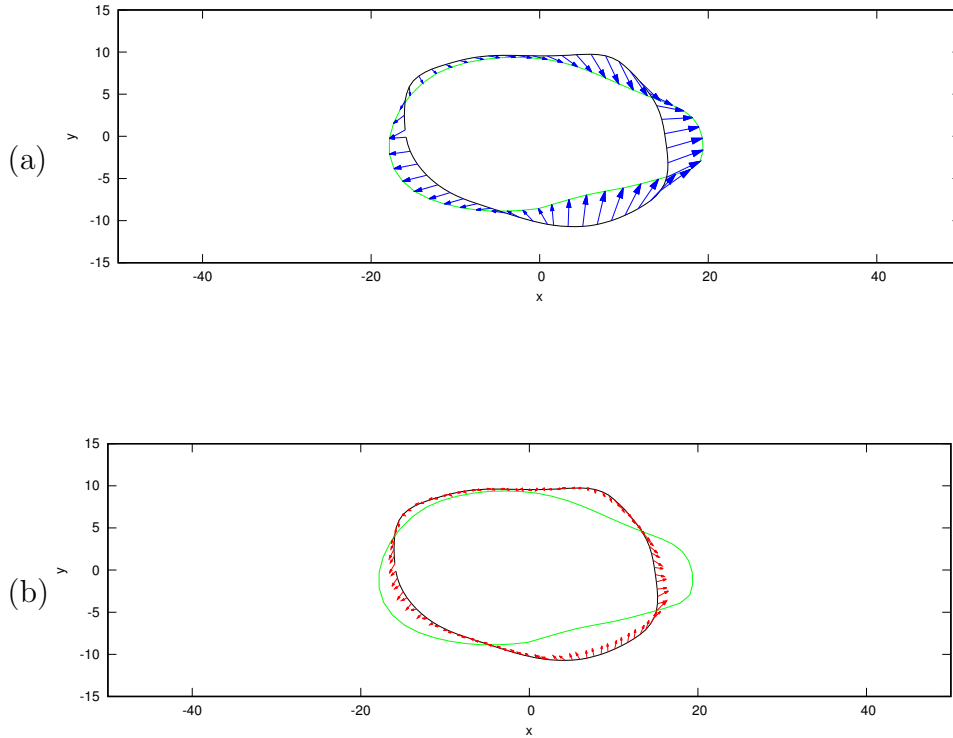
Figure 3.11: (a) shows the deformation field an example nucleus from prior to the constriction, to the shape of the nucleus as it begins entering the constriction. (b) shows the traction force field causing the deformation shown in (a). The black outline is the undeformed shape, while the green outline is the deformed shape. In (a) the blue arrows represent the final deformation field found between the images. The deformed shape is moved a distance +1.7 pixels along the x direction, from the centre of mass aligned position (see section 3.10.2). In (b), the red arrows represent the traction force direction and magnitude, with each arrow scaled such that one unit of length on the axes represents a traction force of 1kPa. The nucleus has zero curvature in the out of plane direction, as shown in figure 3.1.

to the surface at that point, $\mathbf{t_i} = \sigma_{ij}\mathbf{n_j}$. In figure 3.11, the deformation shown has been calculated using the energy minimisation method discussed earlier in this chapter. The input shapes are noisy in comparison to the average shapes, as described in section 3.5. This is responsible for the lack of symmetry in the outlines, as can be seen from the overlayed outlines in figure 3.11, where the shape for $y > 0$ is significantly different to $y < 0$. The noise then leads to non intuitive deformation and traction fields, compared to what one might expect for the nucleus entering in to a constriction. For instance, near the rear of the nucleus in this example, there is a significant downwards component to the force, as a result of a lack of symmetry in the shape. These single images could be useful, for example if comparing the force in a given deformation with some known force generation mechanism, such as the intensity of observed filaments as discussed in Chapter 2. However they are harder to compare with predictions for forces that cause shape changes of the nucleus during movement through a constriction. Instead, we now use the average shapes of nuclei for the remainder of this and the following chapter where the images of nuclei moving through channels containing constrictions are considered.

3.13 Results for average shaped nucleus

3.13.1 Centre of mass aligned nuclei for $\nu = 0.5$

Firstly we examined the behaviour of cell nuclei where the nuclei were aligned between images by their centres of mass. This means the deformation field from the source shape to the target shape was assumed to be zero at the centre of mass of both shapes. The deformation field in the centre of mass frame represents a nucleus that does not have any forward motion, and so is only an approximation of the deformation experienced by the nuclei travelling through the channels. This version of the model could be applied to nuclei within cells changing shape, but not undergoing motion, such as in the steps

leading up to cell division.
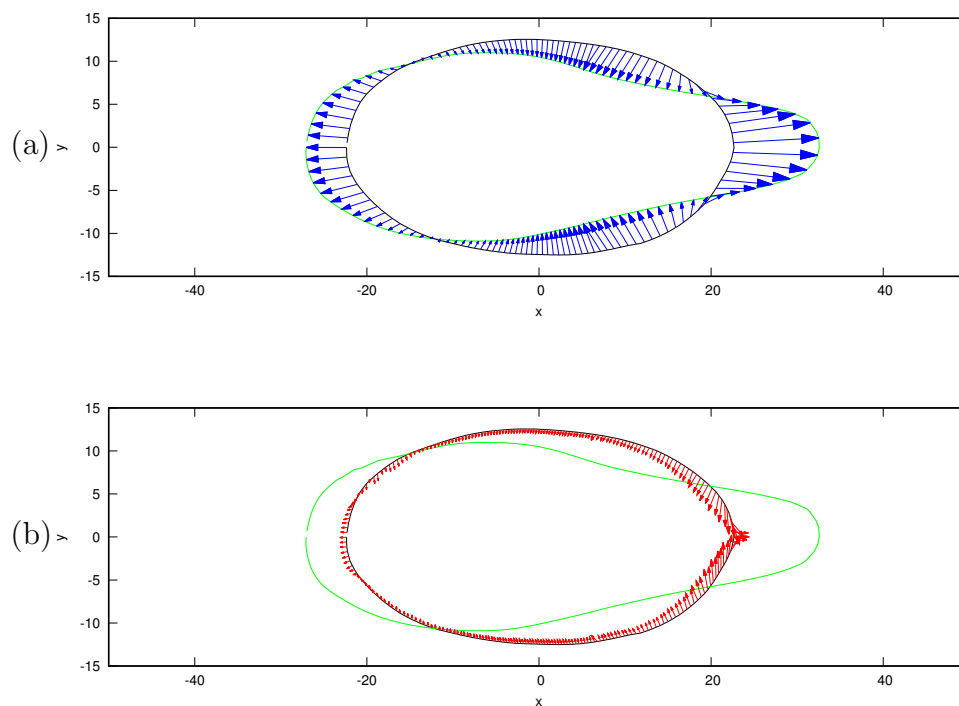
Figure 3.12: (a) shows the deformation field of the nucleus from the average shape of 71 nuclei prior to the constriction, to the average shape of 56 nuclei as they begin entering the constriction. (b) shows the traction force field causing the deformation shown in (a). The black outline is the undeformed shape, while the green outline is the deformed shape. In (a) the blue arrows represent the final deformation field found between the images. The deformed shape is moved a distance +1.7 pixels along the x direction, from the centre of mass aligned position (see section 3.10.2). In (b), the red arrows represent the traction force direction and magnitude, with each arrow scaled such that one unit of length on the axes represents a traction force of 1kPa. The nucleus has zero curvature in the out of plane direction, as shown in figure 3.1.

Figure 3.12 shows the traction force for the deformation of the average shape of the nucleus, where the images of the nucleus are aligned at the origin (0,0). The force distribution shows an almost constant magnitude force at the rear of the nucleus outwards, towards the direction of deformation. The direction of the traction force then swaps from outwards to inwards nearer, the centre of the body, as one might expect where the deformation is of the nucleus being compressed in that direction.The traction force then increases in magnitude towards the leading edge of the nucleus, perpendicular to the direction of the motion, except near the very front, where the traction direction rapidly switches towards the direction along the channel.

We then look at the same outlines of nuclei, but instead with the two shapes aligned at the rear, then compare the resulting traction fields.

3.13.2   Rear aligned nuclei for $\nu = 0.5$

In order to more closely model the behaviour of the nuclei, we now consider other alignments beyond placing both deformed and undeformed nuclei so that the centre of mass of both is at $(0, 0)$. Here, we positioned the deformed nuclei so that the rear of the deformed cell nucleus starts at the same position prior to energy minimisation as the undeformed shape. To find the initial alignment, both the deformed and undeformed shapes are placed in the centre of mass frame. The most negative x value of both the deformed and undeformed is then found. The deformed nucleus shape is then shifted along the x axis by the difference between the most negative x coordinates of the undeformed and deformed shapes respectively, $(x_{undeformed_min} - x_{deformed_min})$ so that the rear of the deformed shape aligns with the rear of the undeformed shape. The centre of mass of the undeformed shape is kept at $(0, 0)$ and the deformation of the outline is still assumed to drop to zero linearly at the centre of mass of the undeformed shape.

Figure 3.13 shows the results of the deformation field and traction when the rear points are initially aligned. The rears are not exactly aligned after
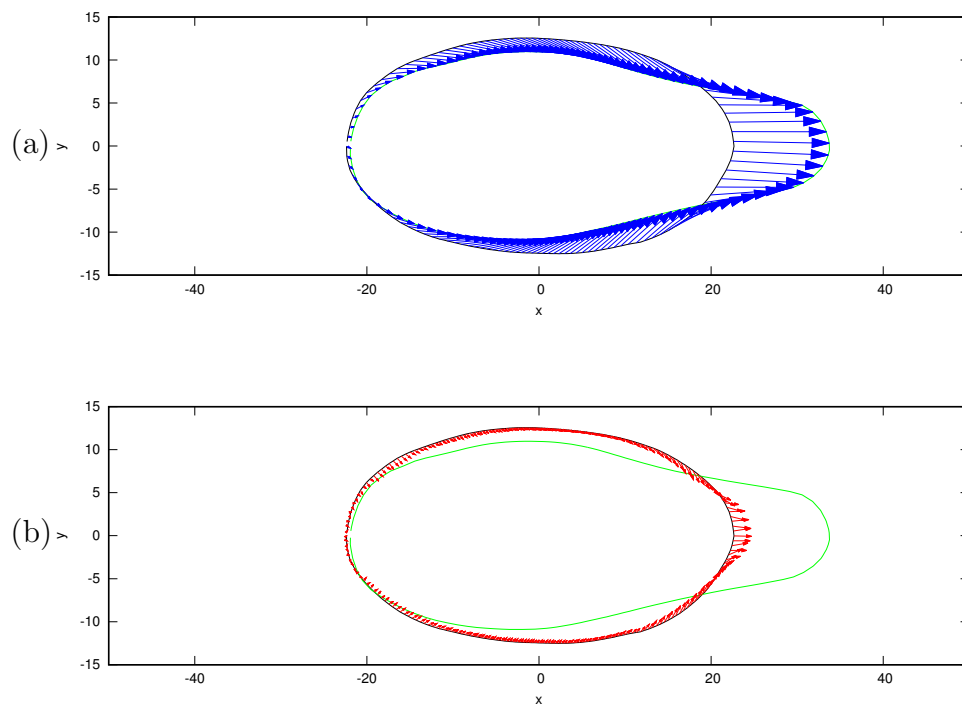
Figure 3.13: (a) shows the deformation field of the nucleus from the average shape of 71 nuclei prior to the constriction, to the average shape of 56 nuclei as they begin entering the constriction. (b) shows the traction force field causing the deformation shown in (a).

The black outline is the undeformed shape, while the green outline is the deformed shape. In (a) the blue arrows represent the final deformation field found between the images. The deformed shape is moved a distance +1.7 pixels along the x direction, from the centre of mass aligned position (see section 3.10.2). In (b), the red arrows represent the traction force direction and magnitude, with each arrow scaled such that one unit of length on the axes represents a traction force of 1kPa. The nucleus has zero curvature in the out of plane direction, as shown in figure 3.1.

the simulated annealing algorithm as a small amount of volume is lost from where the points move slightly, due to the assumption of perturbations occur-

ring on linear segments between points. The volume loss is limited (change from rear is around 0.2pixels), and so not considered further here.

3.13.3   Aligned nuclei for $\nu = 0.5$

Lastly, we look at aligning the nuclei based on the average shape changes, at a point between the centre of mass and the rear/front aligned cases, based on the changes in front and rear positions given in figure 3.10. Figures 3.14-3.17 show the deformations and traction forces between the five averaged shapes of the nucleus. The figures show the deformation and associated traction fields prior to the constriction to beginning to enter (figure 3.14), entering to fully in the constriction (figure 3.15), from in the constriction to beginning to leave (figure 3.16) and from leaving the constriction to after having fully left the constriction (figure 3.17). Each of the deformed shapes are shifted along x relative to the undeformed shape from the centre of mass position, by the amount given in table 3.1.

In figure 3.14, the nucleus begins to enter the constriction. The resulting traction force shows compression everywhere except close to the rear and front of the nucleus, as in the centre of mass aligned case. At the leading edge, there are outwards forces, with a small increase in magnitude at the front compared to the centre aligned example shown in figure 3.12. Similarly there is a small decrease in magnitude of the force at the rear. These changes are as we would expect when the deformed shape position is moved along the positive x direction, relative to the undeformed shape.

The traction force as the nucleus goes from entering to fully inside the constriction, shown in figure 3.15 has a positive x component almost everywhere. This is an unsurprising result, given that earlier we found that the front of the nucleus moves more compared to the rear of the nucleus in this part of the deformation process than in any of the other time steps, as shown in figure 3.10b. There is a small region of points near the rear that show a rear facing traction force, where the nucleus still deforms in that direction.

However this is notably a smaller region than in the other figures. This is likely to be the result of the front of the nucleus moving more than the rear of these nuclei.

The next figure, 3.16, shows the traction force as the nucleus changes shape from the shape taken inside the constriction to the shape on beginning to exit. Because of the curve representing the undeformed shape being almost parallel to the x axis, the traction arrows over that region are therefore almost perpendicular to the x direction, due to the definition of the traction used in equation 3.5. The traction force is larger in magnitude near the front than the rear, due to the larger deformation of the front in plane than at the rear. Also noticeable in this diagram are the points making up the surface, preferring to move closer together nearer the origin $(0,0)$ than at the ends during the energy minimisation process, causing more points along the lines near the centre than at the ends. This effect was not as noticeable in figure 3.14, where the figure outline was more uniform around the origin.

The final figure, 3.17 shows the traction force on the nucleus as it changes shape from the average shape during exit of the constriction, to the average shape taken when the nucleus has fully left the constriction. The average shapes used are notably similar to the shapes taken before the constriction and on entering, as we would expect from an object displaying elastic behaviour. The magnitude of the force is now significantly larger at the rear than at the front, which coincides with the rear of the nucleus now deforming more to regain the shape prior to entry in to the constriction, when the front of the nucleus has already left the constriction.

These figures demonstrate the model we have created, which we used to determine the traction force from experimental data. However, this computational model is not restricted to nuclei within channels and could be applied to any images of deforming nuclei, if appropriate assumptions are made about the deformation in the out of plane direction. This could also be used if the images provided information about the out of plane direction,

as is the case in chapter 6.
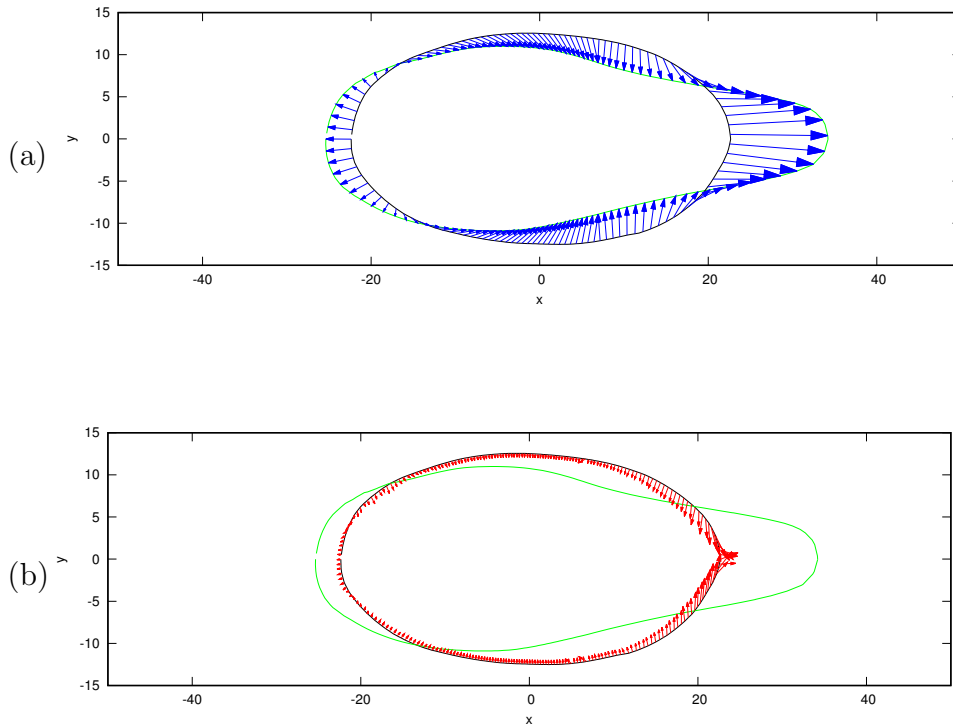
Figure 3.14: (a) shows the deformation field of the nucleus from the average shape of 71 nuclei prior to the constriction, to the average shape of 56 nuclei as they begin entering the constriction. (b) shows the traction force field causing the deformation shown in (a). The black outline is the undeformed shape, while the green outline is the deformed shape. In (a), the blue arrows represent the final deformation field found between the images. The deformed shape is moved a distance +1.7 pixels along the x direction, from the centre of mass aligned position (see section 3.10.2). In (b), the red arrows represent the traction force direction and magnitude, with each arrow scaled such that one unit of length on the axes represents a traction force of 1kPa. The nucleus has zero curvature in the out of plane direction, as shown in figure 3.1.

Figure 3.15: (a) shows the deformation field of the nucleus from the average shape of 56 nuclei entering the constriction, to the average shape of 71 nuclei within the constriction. (b) shows the traction force field causing the deformation shown in (a). The black outline is the undeformed shape, while the green outline is the deformed shape. In (a) the blue arrows represent the final deformation field found between the images. The deformed shape is moved a distance +1.7 pixels along the x direction, from the centre of mass aligned position (see section 3.10.2). In (b), the red arrows represent the traction force direction and magnitude, with each arrow scaled such that one unit of length on the axes represents a traction force of 1kPa. The nucleus has zero curvature in the out of plane direction, as shown in figure 3.1.

Figure 3.16: (a) shows the deformation field of the nucleus from the average shape of 71 nuclei within the constriction, to the average shape of 55 nuclei as they begin exiting the constriction. (b) shows the traction force field causing the deformation shown in (a). The black outline is the undeformed shape, while the green outline is the deformed shape. In (a) the blue arrows represent the final deformation field found between the images. The deformed shape is moved a distance +1.7 pixels along the x direction, from the centre of mass aligned position (see section 3.10.2). In (b), the red arrows represent the traction force direction and magnitude, with each arrow scaled such that one unit of length on the axes represents a traction force of 1kPa. The nucleus has zero curvature in the out of plane direction, as shown in figure 3.1.

Figure 3.17: (a) shows the deformation field of the nucleus from the average shape of 55 nuclei exiting the constriction, to the average shape of 71 nuclei after they have fully exited the constriction. (b) shows the traction force field causing the deformation shown in (a). The black outline is the undeformed shape, while the green outline is the deformed shape. In (a) the blue arrows represent the final deformation field found between the images. The deformed shape is moved a distance $+1.7$ pixels along the x direction, from the centre of mass aligned position (see section 3.10.2). In (b), the red arrows represent the traction force direction and magnitude, with each arrow scaled such that one unit of length on the axes represents a traction force of 1kPa. The nucleus has zero curvature in the out of plane direction, as shown in figure 3.1.

3.14 Summary

In this chapter, we have described the computational model that we have created for analysing the deformation of cell nuclei. The cell nuclei were modelled as a homogeneous elastic solid. We then used a simulated annealing algorithm to determine the deformation between two outlines by minimising the energy of deformation. To demonstrate the model being used, we applied the model to images of nuclei moving through channels, provided by Matthieu Piel and Hawa Thiam. Based on our analysis of the area change of these nuclei and the change in florescence intensity of the DNA within the nucleus, we determined that these nuclei behave like an incompressible elastic material.

We described a method to convert those images into outlines. These outlines were then used as input data to the model, comparing the use of a single image to the use of the average shapes generated from a large number of nuclei images. These images were used to generate the deformation and traction fields shown in figures 3.14 to 3.17, as an example of the calculation of the forces that caused the deformation of a nucleus in the experiment of nuclei confined within channels.

In the following chapter, we build on this model with a second description of the nucleus, where instead of treating the nucleus as a homogeneous elastic solid, it is described as a thin elastic shell. Another possible approach would be to consider other elastic models that could be applied to the nucleus, such as viscoelastic behaviour or different nonlinear elasticity models. However further elastic solid models are beyond the scope of this thesis.

Chapter 4

Nuclear deformation: Shell model

4.1 Introduction

In this chapter we will discuss modelling the cell nucleus as a thin elastic shell, rather than as a homogeneous elastic solid as in the previous chapter. We have produced a computational model similar to the previously discussed solid nucleus model to determine the deformation, strain, stress and traction fields of a deforming thin shell.

The chapter briefly describes the differential geometry needed to calculate the strain in a general coordinate system, and how to convert the data from a Cartesian deformation to a strain in the basis used to calculate the strains, and then the resulting strain back to the Cartesian equivalent. This is then applied to the average shapes of the nucleus deforming, as in the prior chapter, to determine the traction fields during deformation if the nucleus behaves as a thin elastic shell. We then compare these results with the solid model traction forces for the same nuclear shapes, and discuss the effect of treating the nucleus as a thin shell.

4.2 Cell nucleus as a thin elastic shell

In the previous chapter, we treated the cell nucleus as a homogeneous elastic solid capable of deforming.In this chapter, we propose a second model of the nucleus, where we treat only the nuclear lamina as having an elastic response to deformation, rather than the entirety of the nucleus. We model the nuclear lamina, which surrounds the DNA and other contents within the nucleus, as a thin elastic shell.

The approximation of the nuclear lamina as a thin elastic shell is motivated by the assumption that the nuclear lamins of types A and B, which have been shown to provide mechanical stability to the nucleus [23], respond to deformations like an elastic material. In addition, the relative volume of the nuclear lamina is assumed to be a relatively small fraction of the total volume of the nucleus. This is consistent with measurements of the thickness

of the nuclear lamina, which is typically on the order of 100nm,. Compared to the height of the nucleus in these constrictions, which is limited to $2\mu m$ within the constriction, this is estimated as $\frac{0.1\mu m * 2}{2\mu m} \approx 10\%$ of the nucleus height at the most constricted. The nuclear lamina is considered to be a homogeneous elastic material, with the same properties over the entire lamina surface, as in the solid model in the previous chapter.

In the images of the nucleus, the method to determine the deformation of the nuclear outline as described in section 3.10 is used again here.

As the strains are calculated using only on the deformation of the elastic lamina, the stress and traction values then calculated from these strains only represent the induced stress and force required for the surface, and not the inner material. This means that the traction forces calculated only represent the force required to cause the deformation of the elastic shell, and not to deform the contents of the nucleus. This effectively assumes that the material inside the elastic shell is completely compressible, requiring no additional force to deform.

In order to calculate the deformation field through the energy minimisation method, minimising the free energy of deformation given in equation 3.4, requires that we are able to calculate both the stress and strain over the nucleus surface. In order to calculate the strain for the nucleus as a thin elastic shell, we use the thin shell approximation. The thin shell approximation here means all derivatives across the normal direction of the surface are negligible in comparison to the derivatives along the tangential directions.

In comparison to the solid model nucleus case, where we required the deformation field to be defined inside the nucleus, assuming the nucleus is a thin shell together with the thin shell approximation instead defines the strain over the elastic body entirely. We do not need to define the deformation inside the body, as was required for the elastic solid model of the nucleus.

To incorporate the thin shell approximation in to a shell model of the nucleus, we therefore calculate the strains in the normal and tangential coor-

dinate basis $(\mathbf{s_1}, \mathbf{s_2}, \mathbf{n})$, before transforming the values back in to Cartesian coordinates.

4.2.1 Differential geometry of surfaces

In order to generally describe the more complicated unknown surface in the general tangent and normal coordinate basis, and calculate values along the surface, we first describe the general form of the derivatives using differential geometry. The general forms involve the curvatures of the surface and the christoffel symbols of the surface, and an analytic method to calculating the derivatives is given below.

Briefly, a surface $\mathbf{X}(\mathbf{s_1}, \mathbf{s_2}, \mathbf{n})$ described by two tangential directions s_1, s_2 and the normal direction n has an associated metric tensor given by the derivatives of the surface along each of the directions at each point.

$$g_{ij} = \left(\frac{\partial X(s_1, s_2, n)}{\partial x_i} \cdot \frac{\partial X(s_1, s_2, n)}{\partial x_j} \right) \tag{4.1}$$

For a positively oriented surface, where by definition when travelling along the curve describing the surface, the interior of the curve is on the left, the outwards normal to the surface is then given by

$$\mathbf{n} = \mathbf{e_{s_1}} \times \mathbf{e_{s_2}} = \frac{\partial X(s_1, s_2, n)}{\partial s_1} \times \frac{\partial X(s_1, s_2, n)}{\partial s_2}. \tag{4.2}$$

Then, for a surface with two tangent vectors $\mathbf{e}$ and $\mathbf{e\prime}$ with components in the basis $(x, y, \cdots)$ represented by subscripts, the metric tensor is given as

$$\mathbf{g} = \begin{pmatrix} e_x \cdot e'_x & e_y \cdot e'_y & \cdots \\ e_x \cdot e'_x & e_y \cdot e'_y & \cdots \\ \vdots & \vdots & \ddots \end{pmatrix} \tag{4.3}$$

The christoffel symbols are written in terms of the metric tensor as

$$\Gamma_{ij}^k = \frac{1}{2}g^{kl}\left(\frac{\partial g_{il}}{\partial x_j} + \frac{\partial g_{jl}}{\partial x_i} - \frac{\partial g_{ij}}{\partial x_l}\right). \tag{4.4}$$

Similarly, the curvature of the surface, measured as the rate of change of the normal direction along the surface can be expressed as a tensor, C_{ij}.

A thin shell surface can be written as a function of only the two tangent directions, $\mathbf{X}(\mathbf{s_1}, \mathbf{s_2}, \mathbf{n})$, and so the metric tensor is a 2x2 matrix, with the components s_1 and s_2 representing two tangent directions along the surface.

$$\mathbf{g} = \begin{pmatrix} e_{s1} \cdot e_{s1} & e_{s1} \cdot e_{s2} \\ e_{s1} \cdot e_{s2} & e_{s2} \cdot e_{s2} \end{pmatrix}. \tag{4.5}$$

The derivatives along the surface of the basis vectors are then given in terms of the curvature and metric as

$$\frac{\partial \mathbf{e_j}}{\partial x^i} = C_{ij}\mathbf{n} + \Gamma_{ij}^k\mathbf{e_k}. \tag{4.6}$$

Using these relations, we can describe any thin shell surface, for instance those seen in images of the nucleus. Because the images considered are only in two dimensions, an analytical approach is used to describe the out of plane direction s_2,which will discussed in the following section, while the in plane images provide s_1 from the outline. The normal direction is assumed outwards, and an assumption that the shape must be symmetric in the out of plane direction requires that the normal also be in the XY plane seen in images, and so can be determined purely from the s_1 tangent vector. As the surface is flat in the out of plane direction, the vector in the out of plane direction is easily defined as a unit length vector parallel to the z axis. As such the metric tensor is the identity and the christoffel symbols are all zero, leaving only the curvature terms in the shell model of this particular out of plane direction shape. However, this is included in the computational model to allow for use with other, more complicated shapes if necessary, however this is beyond the scope of this thesis.

Using these equations from differential geometry, it is then possible to calculate the strain in an arbitrary coordinate system.

4.2.2 Shell model calculations

In the two dimensional plane XY seen in images, we define the $\mathbf{s_1}$ direction as the in plane tangent direction, orientated so that the normal direction $\mathbf{n}$ is directed outwards. The $\mathbf{s_1}$ and $\mathbf{n}$ components of the strain are calculated numerically in our model, through substitution of the above expressions in to the general form of the strain tensor

$$u_{ij} = \frac{1}{2}\left(\frac{\partial u_i}{\partial x_j} + \frac{\partial u_j}{\partial x_i} + \frac{\partial u_i}{\partial x_k}\frac{\partial u_j}{\partial x_k}\right) \tag{4.7}$$

We assume that the surface of the nucleus has zero curvature in the out of plane direction, and that the two dimensional images represent the deformation as motivated by the assumption that the nucleus fills the channel at all times as in section 3.9. As the surface has in the out of plane direction, the curvature in this direction is zero at the planes observed in the images, meaning the derivative of the normal vector in this direction is zero.

In this section, the curvature tensor components are

$$C = \left(\begin{array}{cc} \left(\frac{\partial \mathbf{n}}{\partial s_1}\right)\cdot\mathbf{e_{s1}} & \left(\frac{\partial \mathbf{n}}{\partial s_1}\right)\cdot\mathbf{e_{s2}} \\ \left(\frac{\partial \mathbf{n}}{\partial s_2}\right)\cdot\mathbf{e_{s1}} & \left(\frac{\partial \mathbf{n}}{\partial s_2}\right)\cdot\mathbf{e_{s2}} \end{array}\right) = \left(\begin{array}{cc} \left(\frac{\partial \mathbf{n}}{\partial s_1}\right)\cdot\mathbf{e_{s1}} & 0 \\ 0 & 0 \end{array}\right) \tag{4.8}$$

where the two of the terms with derivatives of s_2 are zero, because the derivative of the normal vector is zero in the s_2 direction. The term $\left(\frac{\partial \mathbf{n}}{\partial s_1}\right)\cdot\mathbf{e_{s2}}$ is also zero, because the derivative of the normal vector is perpendicular to the s_2 direction, hence the dot product with e_{s2} is zero. The remaining term is calculated numerically. Later, in chapter 6, the full curvature tensor is evaluated numerically when using three dimensional data.

4.3 Converting between (x, y, z) and (s_1, n, s_2) bases

In order to perform the calculations in the shell model, we need to be able to convert values between the Cartesian (x,y,z) basis and the (s_1, n, s_2) basis. The values that need to be expressed in the two bases are either vectors (deformation, traction) or second order tensors (strain, stress). Because the difference between the chosen bases is a rotation of the coordinate axes. we use a combination of rotation matrices to convert the values of the deformation between the two bases. We define the angle from the x axis to s_1 to be given by θ and the angle from the z direction to s_2 is given by ϕ. The vector deformation is converted from the Cartesian basis (x, y, z) through a rotation around z, so that the x axis is aligned to the s_1 direction, and y is rotated by the same angle. If the normal direction is in the x-y plane, then y will be aligned to the normal direction. In this chapter, the normal is in the x-y plane which then requires s_2 to be parallel or antiparallel to z. If the surface direction s_2 was not parallel to z, then a further rotation of the vector is performed. The vector is rotated by angle ϕ around the s_1 direction, so that the vector is expressed in the (s_1, n, s_2) basis. As we assumed that the nucleus fills the channel in the out of plane direction, s_2 is parallel to z and so the angle of rotation is zero in this chapter. However the full rotation expression is used later in chapter 6.

The components of a rotation matrix R are given by $R = e_i \cdot e'_j$, where the unprimed are the basis vectors in the starting configuration (here, Cartesian coordinates) and the primed vectors are the basis vectors in the new configuration, the (s_1, n, s_2) basis. We perform the rotation in two steps, dependent on two angles θ and ϕ.

θ is the angle between the tangent to the nucleus in the xy plane, s_1 and the x axis as shown in figure 4.1. The direction of s_1 relative to the Cartesian axes can be found numerically at any point on the surface using
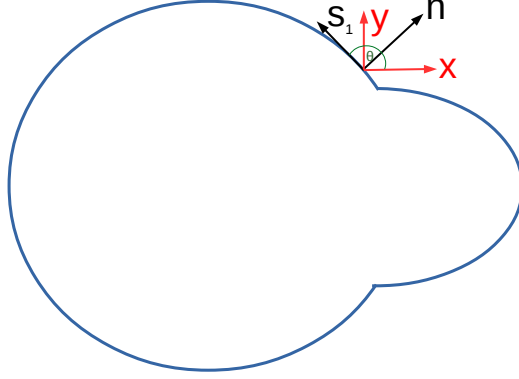
Figure 4.1: Example showing the (s_1, n) basis components compared to the in plane (x, y) coordinates, at a chosen point on the surface.

the neighbouring points. The direction of s_1 at a point i can be approximated by the normalised vector of the straight line between points $i + 1$ and $i - 1$, which have coordinate changes given by $(x_{i+1} - x_{i-1}, y_{i+1} - y_{i-1}, 0)$. s_1 is a normalised vector and given by the following expression

$$s_1 = \frac{(x_{i+1} - x_{i-1}, y_{i+1} - y_{i-1}, 0)}{\sqrt{(x_{i+1} - x_{i-1})^2 + (y_{i+1} - y_{i-1})^2}}. \tag{4.9}$$

The angle between the x direction and the s_1 direction at point i can then be calculated using the inverse tangent, $arctan((y_{i+1} - y_{i-1})/(x_{i+1} - x_{i-1}))$. In order convert the components of a vector, such as the deformation vector, which is measured in the Cartesian basis, to the basis determined by the curve for the calculations, we use a rotation matrix R_θ which rotates around the z axis by the angle θ.

R_θ is similar to the standard rotation matrix, however as rotating both axes by θ would rotate the y axis on to the negative of the normal direction, the expression is slightly different

$$R_\theta = \begin{pmatrix} \cos(\theta) & \sin(\theta) & 0 \\ \sin(\theta) & -\cos(\theta) & 0 \\ 0 & 0 & 1 \end{pmatrix} \tag{4.10}$$

The angle ϕ is the angle between the z axis and the s_2 direction,rotated around s_1. However, ϕ is zero in this case, as the nucleus has zero curvature in the out of plane direction and s_2 is parallel to the z direction.

The deformation vector can be expressed in the new basis representing the surface by the transformation

$$\mathbf{u}(s_1, n, z) = R_\theta^T \mathbf{u}(x, y, z) \tag{4.11}$$

This value is then rotated through angle ϕ around s_1, where the components of s_1 are known from the points on the curve making up the shape. For a point i with neighbours $i + 1$ and $i - 1$, where the curve is orientated clockwise, the vector s_1 is given by $s_1 = \frac{(x_{i+1} - x_{i-1}, y_{i+1} - y_{i-1}, 0)}{|s_1|}$, where $|s_1|$ is a normalisation constant to give a unit vector.

The full rotation of the vector components to express them in the new basis is given as

$$\mathbf{u}(s_1, n, z) = R_\phi^T R_\theta^T \mathbf{u}(x, y, z). \tag{4.12}$$

A similar approach is used to convert the strain tensor from the basis it is calculated in, (s_1, n, s_2) back to Cartesian coordinates.

$$U(s_1, n, z) = R_\phi R_\theta U(s_1, n, s_2) R_\theta^T R_\phi^T. \tag{4.13}$$

In this chapter, due to the assumption of zero curvature of the nucleus surface in the out of plane direction, $\phi = 0$. However the full expression is included in the computational model to allow for use with other shapes of nuclei, or three dimensional data as in chapter 6.

4.4   Shell model results

4.4.1   Traction forces for an incompressible shell
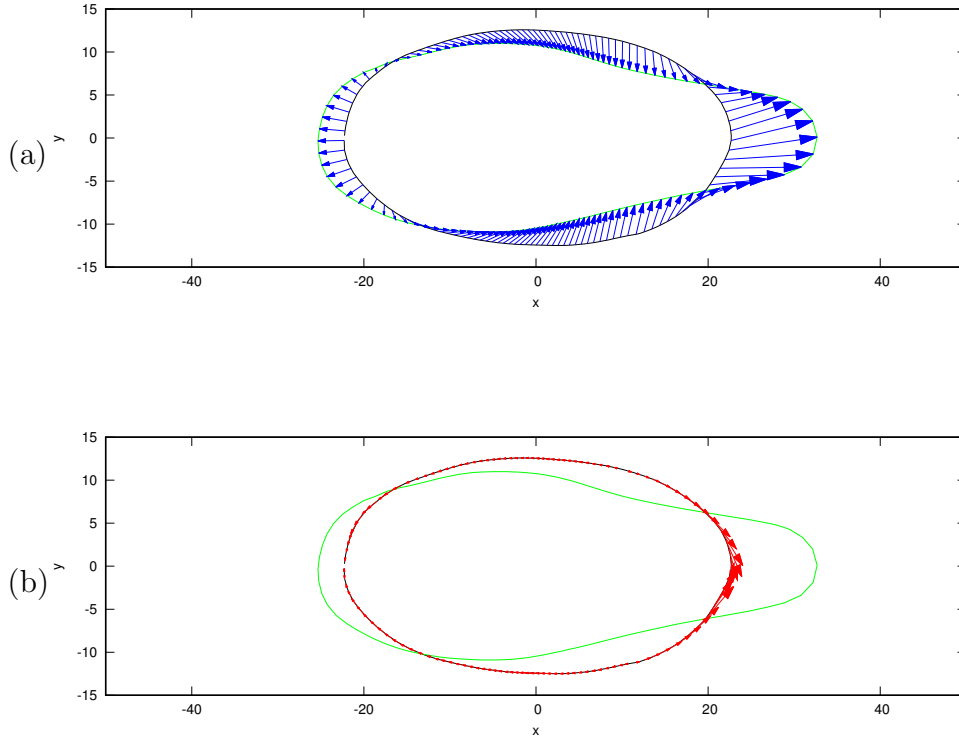
Figure 4.2: (a) shows the deformation field of the nucleus from the average shape of 71 nuclei prior to the constriction, to the average shape of 56 nuclei as they begin entering the constriction. (b) shows the traction force field causing the deformation shown in (a). The black outline is the undeformed shape, while the green outline is the deformed shape.

In (a) the blue arrows represent the final deformation field found between the images. The deformed shape is moved a distance +1.7 pixels along the x direction, from the centre of mass aligned position (see section 3.10.2).

In (b), the red arrows represent the traction force direction and magnitude, with each arrow scaled such that one unit of length on the axes represents a traction force of 0.5kPa. The nucleus has zero curvature in the out of plane direction, as shown in figure 3.1.

Figure 4.3: (a) shows the deformation field of the nucleus from the average shape of 56 nuclei entering in to the constriction, to the average shape of 71 nuclei when they are fully inside the constriction. (b) shows the traction force field causing the deformation shown in (a). The black outline is the undeformed shape, while the green outline is the deformed shape. In (a) the blue arrows represent the final deformation field found between the images. The deformed shape is moved a distance $+7.3$ pixels along the x direction, from the centre of mass aligned position (see section 3.10.2). In (b), the red arrows represent the traction force direction and magnitude, with each arrow scaled such that one unit of length on the axes represents a traction force of 0.5kPa. The nucleus has zero curvature in the out of plane direction, as shown in figure 3.1.
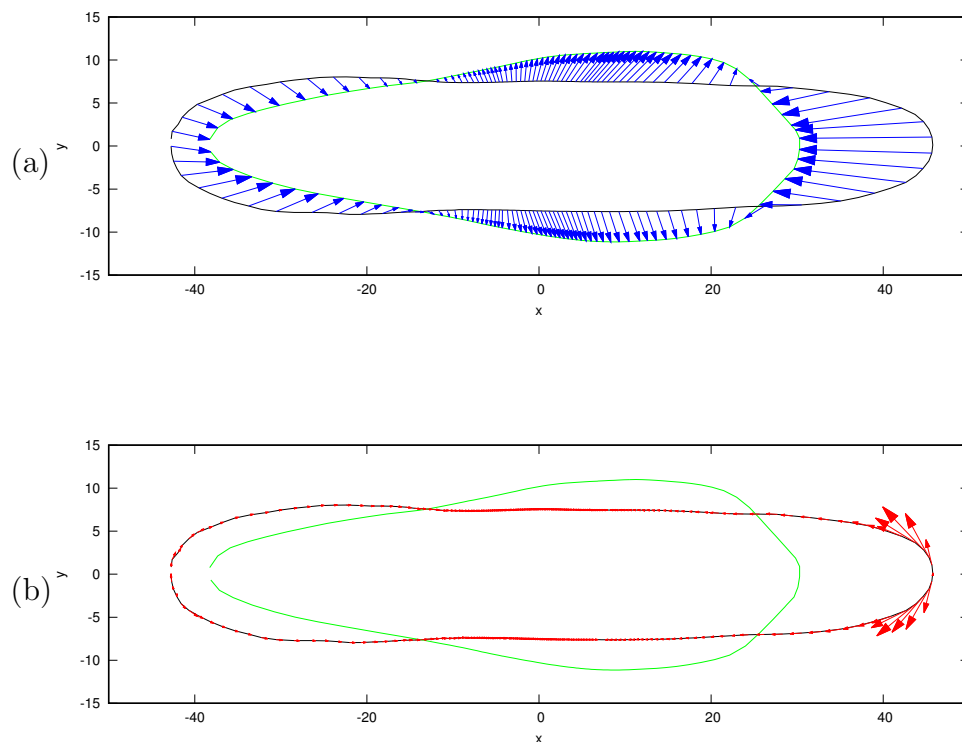
Figure 4.4: (a) shows the deformation field of the nucleus from the average shape of 71 nuclei inside the constriction, to the average shape of 55 nuclei as they begin exiting the constriction. (b) shows the traction force field causing the deformation shown in (a). The black outline is the undeformed shape, while the green outline is the deformed shape. In (a) the blue arrows represent the final deformation field found between the images. The deformed shape is moved a distance +0.15 pixels along the x direction, from the centre of mass aligned position (see section 3.10.2). In (b), the red arrows represent the traction force direction and magnitude, with each arrow scaled such that one unit of length on the axes represents a traction force of 0.5kPa. The nucleus has zero curvature in the out of plane direction, as shown in figure 3.1.
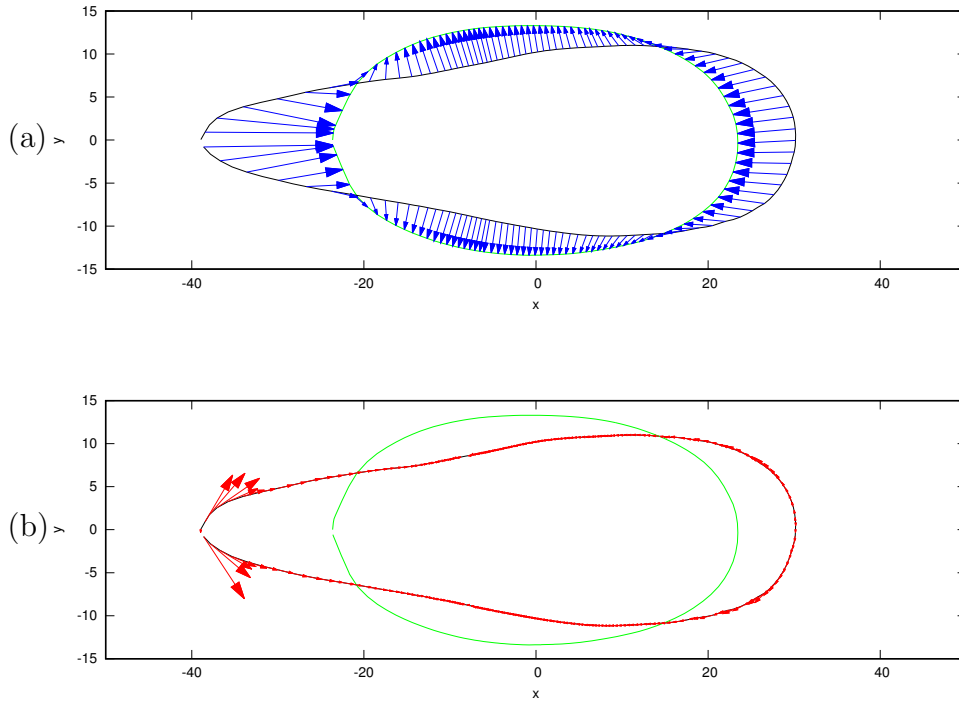
Figure 4.5: (a) shows the deformation field of the nucleus from the average shape of 55 nuclei exiting the constriction, to the average shape of 71 nuclei after they have fully left the constriction. (b) shows the traction force field causing the deformation shown in (a). The black outline is the undeformed shape, while the green outline is the deformed shape. In (a) the blue arrows represent the final deformation field found between the images. The deformed shape is moved a distance 0.0 pixels along the x direction, i.e. is kept at the centre of mass aligned position (see section 3.10.2). In (b), the red arrows represent the traction force direction and magnitude, with each arrow scaled such that one unit of length on the axes represents a traction force of 0.5kPa. The nucleus has zero curvature in the out of plane direction, as shown in figure 3.1.

As in the previous chapter, we present the results of our shell model traction force calculations. We applied our model to videos of dendritic cell nuclei as they travelled through channels containing constrictions. Figures 4.2-4.5 show the traction and deformation fields output for the averaged shapes of the nucleus passing through the constriction.

The deformation fields are different to the deformation fields found in figures 3.14-3.17. This is unsurprising given the energy of deformation (which is minimised to determine the final deformation field) is dependent on the strain of the material. In the solid model, points on the deformed shape were positioned to minimise radial distance. In the shell model, the deformation minimises the number of points in regions of high curvature. This is due to the term in the strain calculations proportional to the curvature in plane along s_1, multiplied by the normal deformation at that point, u_n. Having fewer points in these regions outweighs the energy cost of having larger variations in the deformation field between neighbours, and so lowers the final energy of deformation.

The traction force in each figure is parallel to the surface at that point. This is due to the incompressibility condition. This can be understood in the (s_1, n, s_2) basis. The nn component of the strain is zero for the shell, while the other terms are in general non-zero. Then in this basis, the stress terms can be written explicitly as

$$\sigma_{ij} = \frac{E}{1+\nu} \left(u_{ij} + \frac{\nu}{1-2\nu} \left(u_{kk}\delta{ij} \right) \right). \qquad (4.14)$$

However, the incompressibility condition means that $u_{kk} = 0$ over the body regardless of basis. As such this equation simplifies to

$$\sigma_{ij} = \frac{E}{1+\nu} \left(u_{ij} \right). \qquad (4.15)$$

Writing each component explicitly in this basis would give

$$\sigma_{s_1 s_1} = \frac{E}{1 + \nu} \left(u_{s_1 s_1} \right)$$

$$\sigma_{s_1 n} = \frac{E}{1 + \nu} \left(u_{s_1 n} \right)$$

$$\sigma_{s_1 s_2} = \frac{E}{1 + \nu} \left(u_{s_1 s_2} \right)$$

$$\sigma_{nn} = \frac{E}{1 + \nu} \left(u_{nn} \right) = 0$$

$$\sigma_{n s_2} = \frac{E}{1 + \nu} \left(u_{n s_2} \right)$$

$$\sigma_{s_2 s_2} = \frac{E}{1 + \nu} \left(u_{s_2 s_2} \right)$$

where, $\mathbf{t} = \sigma \cdot \mathbf{n}$, with $\mathbf{n} = (0, 1, 0)$ as the unit normal in this basis, the resulting traction is

$$\mathbf{t} = \begin{pmatrix} \sigma_{s_1 s_1} & \sigma_{s_1 n} & \sigma_{s_1 s_2} \\ \sigma_{s_1 n} & \sigma_{nn} & \sigma_{n s_2} \\ \sigma_{s_1 s_2} & \sigma_{n s_2} & \sigma_{s_2 s_2} \end{pmatrix} \begin{pmatrix} 0 \\ 1 \\ 0 \end{pmatrix} = \begin{pmatrix} \sigma_{s_1 n} \\ \sigma_{nn} \\ \sigma_{n s_2} \end{pmatrix} = \begin{pmatrix} \sigma_{s_1 n} \\ 0 \\ 0 \end{pmatrix}. \qquad (4.16)$$

In the incompressible limit, σ_{nn} is zero due to the dependence on the u_{nn} component of strain only, and $\sigma_{n s_2}$ is zero due to the symmetry in s_2, under the assumption that the images represent the central plane of the nucleus. This means the traction is parallel or antiparallel to the s_1 direction in the incompressible limit for a thin elastic shell. In general, the magnitudes of the traction force are smaller than for the equivalent elastic solid deformation shown in chapter 3. This is due to the thin shell approximation setting one component of the strain to zero,whereas in the solid chapter, both in plane directions had non-zero strains. It should be noted when comparing the figures for the shell results, to make the results more visible, the traction

arrows are scaled by 0.5kPa where in chapter 3 they were scaled by 1kPa. This means that any of the traction force arrow would have twice the length in the shell traction images to represent the same magnitude of traction force.

4.4.2 Traction force for a compressible elastic shell ($\nu = 0.4$)

In figures 4.2-4.5, the traction force is parallel to the surface. This then raises the question of whether treating the elastic shell as an incompressible material properly includes the force required to cause any shape changes of the internal parts of the nucleus, which may not necessarily be an incompressible elastic material. To demonstrate that the result of traction arrows being parallel to s_1 is due to the incompressibility condition, we include a result, figure 4.6. In this figure, the nucleus shell is given a Poisson's ratio of $\nu = 0.4$. The magnitudes of the traction force are larger than in figures 4.2-4.5 due to the inclusion of the second term in the stress calculation, where the full stress equation is given by equation 4.14. For an incompressible elastic material, the second term is zero, whereas it is in general non zero for a compressible elastic material. Therefore this results in larger stresses, and consequently the larger traction forces, as shown in figure 4.6. This figure shows a significant component of the traction force is perpendicular to s_1, in comparison with the incompressible examples.

4.5 Summary

In this chapter, we have extended the computational model from the previous chapter for analysing the deformation of cell nuclei. The additions described in this chapter described the nucleus as a thin, homogeneous elastic shell, representing the nuclear lamina. We summarised the differential geometry needed to calculate the components of the strain tensor in the general basis

(s_1, n, s_2). The values of the metric, christoffel symbols and curvature tensor were then applied to the geometry of nuclei as they move through a channel.

The shell model was then applied to the average shape of nuclei as shown in figures 3.3(a)-(e) in Chapter 3.5. For an incompressible elastic shell, this resulted in traction forces of smaller magnitudes than in the corresponding incompressible elastic solid, and with the traction forces parallel to the surface. The forces being parallel to the surface was a result of the incompressible condition, as shown in the comparison in figure 4.6, where the shell was allowed to compress with a Poisson's ratio of 0.4. In this figure, the resulting tractions were no longer parallel to the surface, and were of a larger magnitude due to the additional terms in the stress calculation.
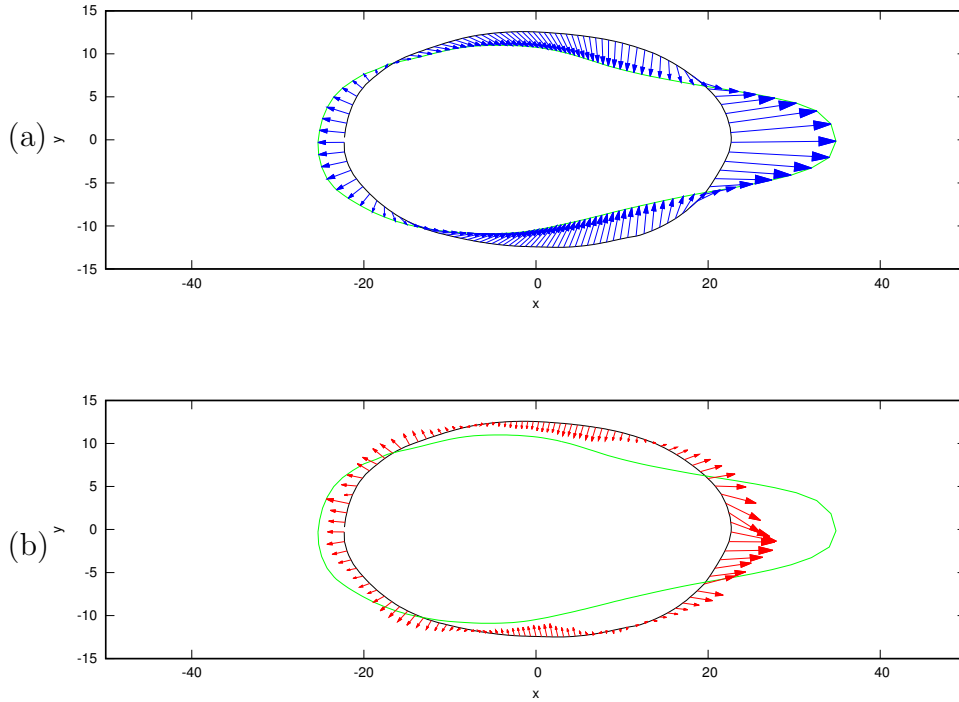
Figure 4.6: The calculated deformation and traction fields as in figure 4.2, but with Poisson's ratio given by $\nu = 0.4$ and Youngs modulus E=5000Pa. (a) shows the deformation field of the nucleus from the average shape of 71 nuclei prior to the constriction, to the average shape of 56 nuclei as they begin entering the constriction. (b) shows the traction force field causing the deformation shown in (a). The black outline is the undeformed shape, while the green outline is the deformed shape. In (a) the blue arrows represent the final deformation field found between the images. The deformed shape is moved a distance 0.0 pixels along the x direction, i.e. is kept at the centre of mass aligned position (see section 3.10.2). In (b), the red arrows represent the traction force direction and magnitude, with each arrow scaled such that one unit of length on the axes represents a traction force of 1.0kPa. The nucleus has zero curvature in the out of plane direction, as shown in figure 3.1.

Chapter 5

Poisson's ratio of cell nuclei

5.1 Introduction

In this chapter we discuss calculating the Poisson ratio of a nucleus. In chapters 3 and 4,we treated the nucleus as an incompressible elastic material ($\nu = 0.5$), but this is not always the case. We discuss a method for numerically calculating the Poisson ratio. We then compare this method to a recent paper which claims to have observed auxetic behaviour in nuclei.

5.2 Numerical calculation of Poisson's Ratio

The assumption that the nucleus fills the channel in the out of plane direction at all times and the observed changes in area in the two dimensional plane measured in images, imply that the nuclei are able to change volume. For a compressible nucleus, the goal is to determine the value of the Poisson's ratio,ν, from a general series of images of nuclear deformation. We require a physically meaningful estimate of ν to determine the traction field of the material through the energy minimisation process described in 3.10. In this section we describe an iterative method, using the relation between the area change of the nuclei and the elastic constants, and the simulated annealing method described in section 3.10, to determine the Poisson's ratio from a series of the images of a cell nucleus deforming as follows.

For a chosen Poisson's ratio, it is possible to determine the deformation, strain, stress and traction fields through an energy minimisation approach, using our Monte Carlo simulations.

The strain and stress induced in the nuclei should be directly related to the relative change in area of the shape and the Poisson's ratio of the material.

The bulk modulus, K, of a material can be expressed in terms of the pressure induced in a material undergoing deformation,

$$K = -V\frac{dp}{dV} \tag{5.1}$$

where the negative sign convention implies that a positive pressure is compressive.

For a material which completely fills a channel of size Lz in the out of plane direction, this can be rewritten in terms of the area, A,

$$K = -V\frac{dp}{dV} = -V\frac{dp}{dV} = -LzA\frac{1}{Lz}\frac{dp}{dA} = -A\frac{dp}{dA}. \tag{5.2}$$

Then using the well known relationship between elastic constants, this expression can be rewritten in terms of the Young's modulus, E, and Poisson's ratio, ν.

$$K = \frac{E}{3\left(1 - 2\nu\right)} \rightarrow \nu = \frac{1}{2} - \frac{E}{6K}. \tag{5.3}$$

In the finite limit, this gives the expression for Poisson's ratio in terms of the area change and pressure on the surface as

$$\nu = \frac{1}{2} - \frac{E\frac{\Delta A}{A}}{6\Delta p} = \frac{1}{2} - \frac{E\frac{\Delta A}{A}}{6p}. \tag{5.4}$$

Where by assuming that the initial shape is undeformed, and that the pressure on the surface prior to deformation is zero on the surface, then Δp is replaced with p, the pressure on the deformed shape. This essentially assumes that the pressure p is that which causes the deformation of the material. The strain, stress and traction fields will be known and vary at different positions on the nuclei for a given Poisson's ratio. Since the area change is a global property of the nucleus undergoing deformation, by comparing the values of the area change with the average pressure, the Poisson's ratio can be determined.

The pressure is defined as the hydrostatic pressure at each point, i.e. $p = \frac{1}{3}\sigma_{ii}$ where the repeated indices represent the Einstein summation convention.

p is calculated as a series of values related to the local deformation of the body, and so varies at each position. The mean value of p is calculated by weighting the stress at each point by the length of segment of the boundary that the stress at that point represents. For a point i on the nucleus boundary at coordinates (x_i, y_i), the neighbouring points on the boundary $i+1$ and $i-1$ have coordinates $(x_{\pm i}, y_{\pm i})$ respectively. The stress components and pressure are then calculated at each point on the body and the pressure at each point is weighted using the distance between i and the midpoints of $i \pm 1$ in each direction as

$$\left(\sqrt{\frac{\Delta x_i}{2.0}^2 + \frac{\Delta y_i}{2.0}^2} + \sqrt{\frac{\Delta x_{i-1}}{2.0}^2 + \frac{\Delta y_{i-1}}{2.0}^2} \right) p_i \tag{5.5}$$

where $\Delta x_i = x_{i+1} - x_i$, $\Delta y_i = y_{i+1} - y_i$ and p_i is the hydrostatic pressure at point i.

The mean weighted pressure used to calulate Poisson's ratio for a nucleus with boundary consisting of N points is then given as

$$\bar{p} = \frac{1}{L} \sum_{i=1}^{N} \left(\sqrt{\frac{\Delta x_i}{2.0}^2 + \frac{\Delta y_i}{2.0}^2} + \sqrt{\frac{\Delta x_{i-1}}{2.0}^2 + \frac{\Delta y_{i-1}}{2.0}^2} \right) p_i \tag{5.6}$$

where L is the total length of the curve representing the nucleus ($L = \sum_{i=1}^{N} \sqrt{(\Delta x_i)^2 + (\Delta y_i)^2}$).

We then calculate the Poisson's ratio of a cell nucleus using an iterative method combining the equations for mean hydrostatic pressure, with Poisson's ratio as given in equation 5.4 and the deformation field found by minimisation of the energy of deformation. As the pressure can vary with position, while the volume (or area) change is measured as a property of the entire nucleus, the average value of p over the entire body is used, where the pressure at each point i, p_i is weighted by the distance along the nucleus surface between the midpoints of the nearest neighbours at $i+1$ and $i-1$.

First a initial Poisson's ratio is chosen (unless stated otherwise, the value

of the Poisson's ratio is initially assumed to be $\nu = 0.40$ in this thesis). This value is then used to calculate the energy of deformations, and through the Monte Carlo simulations described in section 3.10, the minimal energy deformation field is found. Then for this deformation field, the strain and stress are calculated. The stress then provides the hydrostatic pressure for the nucleus. Substituting this value of the pressure in to equation 5.4 then gives a new estimate for ν. The value of ν is then iterated over for the same deformation field, with the stress recalculated for each new ν until the input and calculated values return the same value (the threshold between new and old values of ν is set to be $(\nu_{new} - \nu_{old}) < 10^{-3}$ unless otherwise stated). When a new value of ν is found, the deformation field is then calculated again with the new value of ν. This iterative process is repeated until the Poisson's ratio no longer changes with the new deformation field iteration step.

This method allows us to estimate the Poisson's ratio for a nucleus based on the deformations seen in the images.

5.2.1 General expressions

Poisson's ratio can be expressed in terms of Young's modulus, E, and Bulk modulus, K, as

$$\nu = \frac{1}{2} - \frac{E}{6K}. \tag{5.7}$$

The bulk modulus measures the change in volume, ΔV, of an elastic object with deformation field $\mathbf{u}$, where the deformation is caused by an applied pressure, p. In the small strain limit, K can be expressed as a derivative of the volume change as

$$\frac{1}{K} = -\frac{1}{V_0} \frac{\partial V}{\partial p}. \tag{5.8}$$

We can approximate this in the finite limit, as changing from a volume V_0 of the undeformed elastic object to volume V of the deformed object, under

a pressure change where zero pressure is defined as the undeformed state, so $\Delta p = p$.

Then

$$\frac{1}{K} \approx -\frac{1}{V_0}\frac{\Delta V}{\Delta p} = -\frac{1}{p}\frac{\Delta V}{V_0}. \tag{5.9}$$

Using this expression of the bulk modulus, the equation for Poisson's ratio under small deformations can be written as

$$\nu = \frac{1}{2} - \frac{E\frac{\Delta V}{V_0}}{6p}. \tag{5.10}$$

If the pressure causing the deformation is the hydrostatic pressure, p is defined in terms of the stress tensor as

$$p = \frac{1}{d}\sigma_{ii} = \frac{1}{3}\left(\sigma_{xx} + \sigma_{yy} + \sigma_{zz}\right) \tag{5.11}$$

where d is the number of dimensions used in the system, and the right hand side of the equation is the relation written explicitly in three dimensional Cartesian coordinates.

In addition, the ratio of relative volume change to original volume is equal to the trace of the strain tensor,

$$\frac{\Delta V}{V_0} = u_{ii} = u_{xx} + u_{yy} + u_{zz}.$$

In general then, Poisson's ratio can be evaluated using any of the equivalent equations:

$$\nu = \frac{1}{2} - \frac{Eu_{ii}}{2\sigma_{ii}} \tag{5.12}$$

$$\nu = \frac{1}{2} - \frac{E\frac{\Delta V}{V_0}}{6p} \tag{5.13}$$

$$\nu = \frac{1}{2}\frac{E\frac{\Delta V}{V_0}}{6/d\sigma_{ii}}. \tag{5.14}$$

5.2.2 Uniaxial stress

First we consider a uniaxial stress along the z axis. This requires that the nucleus deforms in such a way that only the σ_{zz} stress term is non-zero, while the other components are zero, i.e.

$$\sigma_{xx} = \sigma_{xy} = \sigma_{xz} = \sigma_{yy} = \sigma_{yz} = 0.$$

The xx and yy terms being zero put constraints on the strains in those directions. Writing the stress terms out explicitly gives the following equations

$$
\begin{aligned}
\sigma_{xx} &= \frac{E}{1+\nu} \left(u_{xx} + \frac{\nu}{1-2\nu} \left(u_{xx} + u_{yy} + u_{zz} \right) \right) \\
&= \frac{E}{(1+\nu)(1-2\nu)} \left((1-\nu)u_{xx} + \nu \left(u_{yy} + u_{zz} \right) \right) \\
&= 0
\end{aligned}
$$

$$
\begin{aligned}
\sigma_{yy} &= \frac{E}{(1+\nu)(1-2\nu)} \left((1-\nu)u_{yy} + \nu \left(u_{xx} + u_{zz} \right) \right) \\
&= 0.
\end{aligned}
$$

So we have two constraints for the strains,

$$(1-\nu)u_{xx} + \nu \left(u_{yy} + u_{zz} \right) = 0 \tag{5.15}$$

$$(1-\nu)u_{yy} + \nu \left(u_{xx} + u_{zz} \right) = 0 \tag{5.16}$$

Subtracting one of these equations from the other leads to the condition that

$$u_{xx} = u_{yy}. \tag{5.17}$$

Substituting this in to either of the equations 5.15 or 5.16 gives

$$0 = \left((1 - \nu)u_{xx} + \nu\left(u_{xx} + u_{zz}\right)\right).$$

This can then be rearranged for ν to give

$$\nu = -\frac{u_{xx}}{u_{zz}}. \tag{5.18}$$

We now demonstrate that the same result occurs from the general equation for Poisson's ratio. Using equation (5.12)

$$
\begin{aligned}
\nu &= \frac{1}{2} - \frac{E u_{ii}}{2\sigma_{ii}} \\
&= \frac{1}{2} - \frac{E\left(u_{xx} + u_{yy} + u_{zz}\right)}{2\left(\sigma_{xx} + \sigma_{yy} + \sigma_{zz}\right)} \\
&= \frac{1}{2}\left(1 - \frac{E\left(2u_{xx} + u_{zz}\right)}{\left(\sigma_{zz}\right)}\right)
\end{aligned}
\tag{5.19}
$$

In the case of a uniaxial stress, the Young's modulus, E, is the ratio between the zz components of stress and strain, $Eu_{zz} = \sigma_{zz}$. Substituting this value into equation (5.19) gives

$$\nu = \frac{1}{2}\left(1 - \frac{\sigma_{zz}\left(2u_{xx} + u_{zz}\right)}{u_{zz}\sigma_{zz}}\right)$$

$$= \frac{1}{2}\left(1 - \frac{\left(2u_{xx} + u_{zz}\right)}{u_{zz}}\right)$$

$$= \frac{1}{2}\left(\frac{u_{zz} - \left(2u_{xx} + u_{zz}\right)}{u_{zz}}\right)$$

$$= \frac{1}{2}\left(\frac{-2u_{xx}}{u_{zz}}\right)$$

$$= -\frac{u_{xx}}{u_{zz}} \tag{5.20}$$

$$\tag{5.21}$$

However, this equation is only valid if the stress is non-zero only in one direction.

5.2.3   Biaxial stress

To illustrate that the above relation is only true for uniaxial stress, we now look at the case where two of the components along the axial directions of the stress tensor are non-zero, while the others are zero.

Let σ_{xx} and σ_{zz} be non-zero, while the other terms are zero, so

$$\sigma_{xy} = \sigma_{xz} = \sigma_{yy} = \sigma_{yz} = 0.$$

As in the uniaxial case, by using the expression of the stress written in terms of strain components, as well as the elastic constants (E and ν) and setting the yy component of stress to be zero, ($\sigma_{yy} = 0$), we have

$$\sigma_{yy} = \frac{E}{\left(1 + \nu\right)\left(1 - 2\nu\right)}\left((1 - \nu)u_{yy} + \nu\left(u_{xx} + u_{zz}\right)\right)$$

$$= 0.$$

The constraint on the yy component of the strain is then

$$u_{yy} = \frac{-\nu}{1-\nu} \left(u_{xx} + u_{zz} \right).$$

Or, rearranged for ν,

$$\nu = -\frac{u_{yy}}{u_{xx} - u_{yy} + u_{zz}}. \tag{5.22}$$

This result can also be obtained from the general Poisson's ratio expression by assuming $\sigma_{yy} = 0$, for the biaxial case.

$$
\begin{aligned}
\nu &= \frac{1}{2} - \frac{E u_{ii}}{2\sigma_{ii}} \\
&= \frac{1}{2} \left(1 - \frac{E \left(u_{xx} + u_{yy} + u_{zz} \right)}{\sigma_{xx} + \sigma_{zz}} \right)
\end{aligned}
$$

The zz term of the strain can be written in terms of the stress components as

$$
\begin{aligned}
u_{zz} &= \frac{1}{E} \left((1+\nu)\sigma_{zz} - \nu \left(\sigma_{xx} + \sigma_{zz} \right) \right) \\
&= \frac{1}{E} \left(\sigma_{zz} - \nu\sigma_{xx} \right).
\end{aligned}
$$

Rearranged for E this gives

$$E = \frac{1}{u_{zz}} \left(\sigma_{zz} - \nu\sigma_{xx} \right) \tag{5.23}$$

The same result can be shown with the xx term of strain, giving

$$E = \frac{1}{u_{xx}} \left(\sigma_{xx} - \nu\sigma_{zz} \right). \tag{5.24}$$

Adding these equations as (5.23)$*u_{zz}$+(5.24)$*u_{xx}$ gives

$$Eu_{zz} + Eu_{xx} = (\sigma_{xx} + \sigma_{zz})(1 - \nu)$$

$$E(u_{zz} + u_{xx}) = (\sigma_{xx} + \sigma_{zz})(1 - \nu)$$

$$E = \frac{(\sigma_{xx} + \sigma_{zz})}{(u_{zz} + u_{xx})}(1 - \nu)$$

Substituting this value in for E gives

$$\begin{aligned}
\nu &= \frac{1}{2}\left(1 - \frac{E(u_{xx} + u_{yy} + u_{zz})}{\sigma_{xx} + \sigma_{zz}}\right) \\
&= \frac{1}{2}\left(1 - \frac{(\sigma_{xx} + \sigma_{zz})(1 - \nu)(u_{xx} + u_{yy} + u_{zz})}{(u_{zz} + u_{xx})(\sigma_{xx} + \sigma_{zz})}\right) \\
&= \frac{1}{2}\left(1 - \frac{(1 - \nu)(u_{xx} + u_{yy} + u_{zz})}{(u_{zz} + u_{xx})}\right) \\
&= \frac{1}{2}\frac{(u_{xx} + u_{zz} - (1 - \nu)(u_{xx} + u_{yy} + u_{zz}))}{(u_{zz} + u_{xx})}
\end{aligned}$$

$$2\nu(u_{zz} + u_{xx}) = -u_{yy} + \nu(u_{xx} + u_{yy} + u_{zz})$$

$$\nu(u_{xx} - u_{yy} + u_{zz}) = -u_{yy}$$

$$\nu = -\frac{u_{yy}}{(u_{xx} - u_{yy} + u_{zz})} \tag{5.25}$$

in agreement with equation (5.22) for Poisson's ratio in case of biaxial stress. In the case of uniaxial stress, where $u_{xx} = u_{yy}$, this reduces back to the expression found for the uniaxial Poisson's ratio, as shown in equation (5.18).

5.2.4   Biaxial strain

In the paper that will be looked at in the following sections, they state that "We choose to apply a one-dimensional compression to the ES cells using only the lateral walls, but not the top and bottom ones.". In addition, they also calculate the strain of the nucleus in two dimensions only, "Finally, the

MATLAB PROGRAM calculates the strain of the nucleus (cell) in both dimensions".

Here we derive the results for a nucleus that is not constrained in the out of plane direction, and then deforms in such a way that the strain in the out of plane direction is zero, $u_{yy} = 0$.

Poisson's ratio can then be expressed from the expression of u_{yy},

$$u_{yy} = \frac{1}{E} \left((1 + \nu) \sigma_{yy} - \nu \left(\sigma_{xx} + \sigma_{yy} + \sigma_{zz} \right) \right) \tag{5.26}$$

$$0 = (1 + \nu) \sigma_{yy} - \nu \left(\sigma_{xx} + \sigma_{yy} + \sigma_{zz} \right) \tag{5.27}$$

$$0 = \sigma_{yy} - \nu \left(\sigma_{xx} + \sigma_{zz} \right) \tag{5.28}$$

$$\nu = \frac{\sigma_{yy}}{\sigma_{xx} + \sigma_{zz}}. \tag{5.29}$$

The same result can be obtained from the general expression of Poisson's ratio, equation (5.12), as follows

$$\nu = \frac{1}{2} - \frac{E u_{ii}}{2 \sigma_{ii}} \tag{5.30}$$

$$= \frac{1}{2} \left(1 - \frac{E \left(u_{xx} + u_{zz} \right)}{\sigma_{xx} + \sigma_{yy} + \sigma_{zz}} \right) \tag{5.31}$$

Expressing the xx and zz components of strains in terms of the stress, for $u_{y}y = 0$ we have

$$u_{xx} = \frac{1}{E} \left(\sigma_{xx} - \nu \left(\sigma_{yy} + \sigma_{zz} \right) \right) \tag{5.32}$$

$$u_{zz} = \frac{1}{E} \left(\sigma_{zz} - \nu \left(\sigma_{xx} + \sigma_{yy} \right) \right). \tag{5.33}$$

Therefore,

$$E \left(u_{xx} + u_{zz} \right) = \left(\sigma_{xx} + \sigma_{zz} \right) \left(1 - \nu \right) - 2 \nu \sigma_{yy} \tag{5.34}$$

Using this expression in equation (5.31), we have

$$\nu = \frac{1}{2}\left(1 - \frac{(\sigma_{xx} + \sigma_{zz})(1 - \nu) - 2\nu\sigma_{yy}}{\sigma_{xx} + \sigma_{yy} + \sigma_{zz}}\right) \qquad (5.35)$$

$$2\nu = \frac{(\sigma_{xx} + \sigma_{yy} + \sigma_{zz}) - (\sigma_{xx} + \sigma_{zz})(1 - \nu) - 2\nu\sigma_{yy}}{(\sigma_{xx} + \sigma_{yy} + \sigma_{zz})}$$

$$(5.36)$$

$$2\nu\left(\sigma_{xx} + \sigma_{yy} + \sigma_{zz}\right) = \sigma_{yy} + \nu\left(\sigma_{xx} + 2\sigma_{yy} + \sigma_{zz}\right) \qquad (5.37)$$

$$\nu\left(\sigma_{xx} + \sigma_{zz}\right) = \sigma_{yy} \qquad (5.38)$$

$$\nu = \frac{\sigma_{yy}}{\sigma_{xx} + \sigma_{zz}} \qquad (5.39)$$

Expressing this solution for ν by writing the stress components in terms of the strains demonstrates that this is not equivalent to $-\frac{u_{xx}}{u_{zz}}$.

5.3 Poisson ratio comparison with existing work

The poisson ratio of a material measures the way it changes shape when forces are applied to it. In this section we compare the results of our approach with that of the published work in the paper of K. Chalut et al. [19], where they claim to have found nuclei with negative poisson ratios.

In the paper, they state that they have calculated the Poisson ratio as follows. "For small strains, the Poisson's ratio can be approximated by the negative of the transverse over axial strain. Thus for axial strains smaller than 0.5 we approximated the Poisson's ratio by fitting the nuclear transverse strain versus axial strain data to a linear function".

These two sentences seem to explain two different methods that are seemingly incompatible in measuring the same value.

The first implies that for small strains, they should be measuring the

value

$$\nu = -\frac{u_{tt}}{u_{aa}}. \tag{5.40}$$

This is equivalent to the uniaxial stress condition, as shown in section 5.2.2.

The second sentence implies that they want to measure

$$\nu = -\frac{\partial u_{tt}}{\partial u_{aa}}. \tag{5.41}$$

where u_{tt} and u_{aa} are the transverse and axial strains respectively.

Elsewhere in the paper, the transverse and axial strains are defined in terms of the deformation between shapes as

$$u_{tt} = \frac{t' - t}{t} \tag{5.42}$$

$$u_{aa} = \frac{a' - a}{a}. \tag{5.43}$$

Where a,t are the ellipsoidal radii along the axial and transverse directions of the undeformed shape, and a',t' are the ellipsoidal radii along the axial and transverse directions. These are equivalent to the expressions of strain for an extending bar in one dimensional strain.

Figure 5.1 is reproduced from the paper [19]. It has been modified to have coloured regions which under the first definition of the strain as given by equation 5.40 would represent non-physical poisson ratios. Under this definition, the green region would have poisson ratios of $\nu > 0.5$ and the blue region represents poisson ratios of $\nu < -1.0$. Three of the nuclei as circled and labelled A,B and C have been compared with the poisson ratio calculation through our iterative energy minimisation method.

By assuming that the nuclear deformation are from circular nuclei, in units so that the radius of the undeformed nucleus is 1, we can estimate from figure 5.1 the ellipses that were deformed to under the first strain definition using equations 5.42 and 5.43.
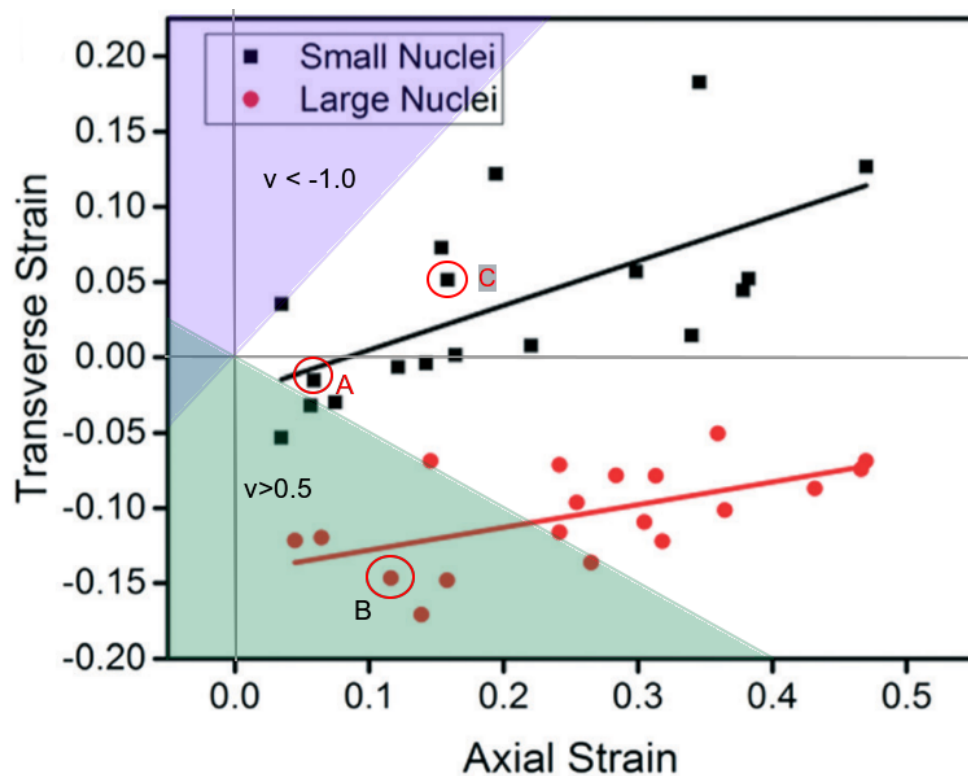
Figure 5.1: Figure adapted from the paper [19] with permission from the Royal society of Chemistry. Three of the nuclei, labelled A,B and C are in different regions where under definition 5.40 they would have different Poisson ratio behaviour under the definition in equation 5.40.

Nucleus	u_{aa}	u_{tt}	a	t	a'	t'	$-\frac{u_{tt}}{u_{aa}}$
A	-0.02	0.05	1	1	0.98	1.05	0.40
B	-0.15	0.12	1	1	0.85	1.12	1.25
C	0.05	0.15	1	1	1.05	1.15	-0.33

Table 5.1

Each is chosen from a different region on the diagram. The definition of poisson ratio in 5.40 is used to calculate the column $\nu = -\frac{u_{tt}}{u_{aa}}$. Nucleus A is predicted to be in the region of $\nu > 0$, behaving like a typical material, B is in the region where this definition predicts an non-physical poisson ratio, and the strains found on nucleus C predict auxetic behaviour of the nucleus.

To conclude that the behaviour of the nucleus is auxetic, the authors of the paper took different nuclei under different deformations, and therefore different strains in the axial and transverse directions, and fit a best fit line to the data, and used the gradient of this line to estimate the strain under the definition from equation 5.41.

5.4 Comparison between results in [19] and output of my calculations and poisson ratio model

In this section, we make comparisons between the paper by Kevin and our model, using the shapes derived from figure 5.1 and given in table 5.1. We compare three shapes from the model by K Chalut et al.[19] model, which each correspond to a different region in the elastic response as measured by the poisson ratio.

5.4.1 Strain comparisons

We first look at the strain outputs from our model in comparison with those provided in the paper. We first look at our model in the centre of mass aligned mode. Here, we compare the calculated strains with the values predicted for circle/ellipse deformations in the paper using formula 5.42 and 5.43. The assumptions about the deformation of the nucleus in the out of plane direction for these comparisons are as in our analysis of the data provided by Hawa Thiam and Matthieu Piel in Chapters 3 and 4. Briefly, we
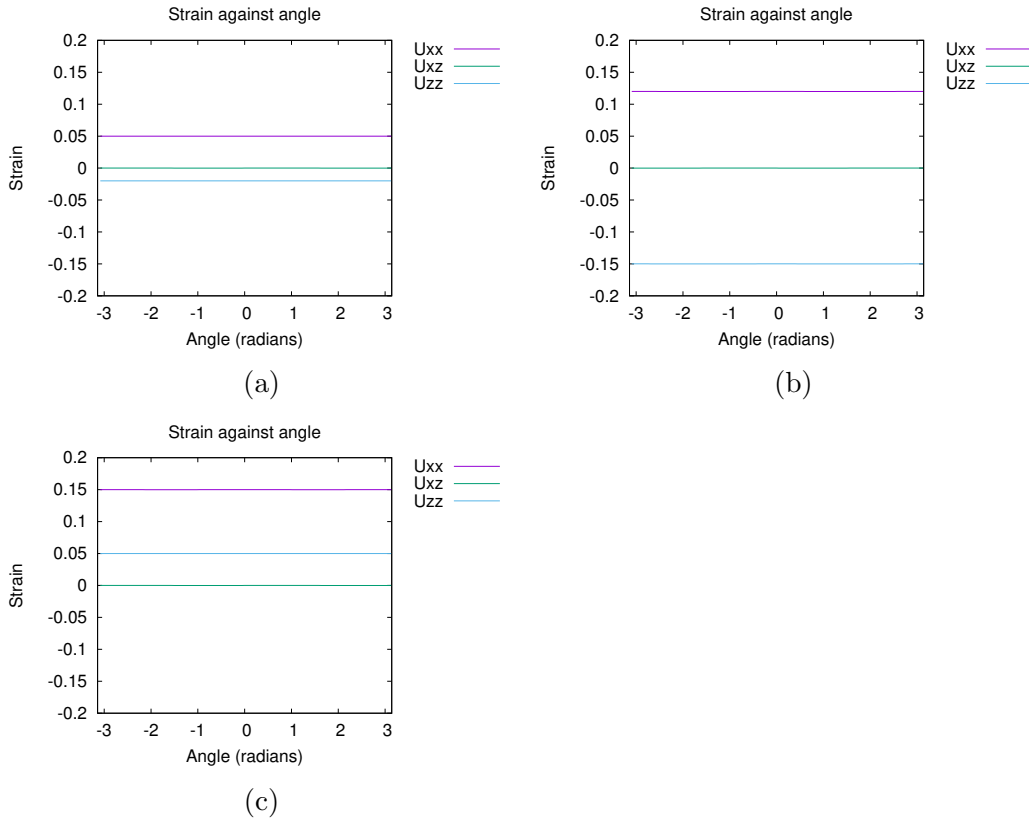
Figure 5.2: The strains calculated for Nucleus A,B and C with the shape parameters as in Table 5.1

assume that the elliptical shape represents the central plane of the nucleus, and that as a result of the symmetry of the deformation, that the strain in the out of plane direction is zero. We therefore are assuming the biaxial strain condition derived above.

Figures 5.2a-5.2c show the strains calculated for the three chosen nuclei. The deformation of each nucleus is chosen as an circle with radius 1 in these units, going to an ellipse, with the axes of the ellipse given by (parallel to x axis under this definition) radius 1.05, and transverse radius (parallel to the z axis) 0.98. Under definitions 5.42 and 5.43, the strains should be constant values across the body given by

$$u_{aa} = u_{xx} = +0.05, \tag{5.44}$$

$$u_{tt} = u_{zz} = -0.02. \tag{5.45}$$

Which is consistent with the calculated strains from our model, as shown in figure 5.2a.

Similarly for nucleus B, deforms from a circle to an ellipse with axial axis radius 1.12, and transverse axis radius 0.85. Under definitions 5.42 and 5.43, the strains should be constant values across the body given by

$$u_{aa} = u_{xx} = +0.12, \tag{5.46}$$

$$u_{tt} = u_{zz} = -0.15. \tag{5.47}$$

Nucleus C deforms from a circle to an ellipse chosen as an ellipse with axes (parallel to x axis under this definition) radius 1.15, and transverse radius (parallel to the z axis) 1.05. Under definitions 5.42 and 5.43, the strains should be constant values across the body given by

$$u_{aa} = u_{xx} = +0.15, \tag{5.48}$$

$$u_{tt} = u_{zz} = +0.05. \tag{5.49}$$

5.4.2   Poisson Ratios

Figures 5.3a,5.3b and 5.3c show the results of the poisson ratio calculation using our model to analyse the circle to ellipse deformations. Using this method, the poisson ratio of Nucleus A was found to converge to 0.5, the poisson ratio of nucleus B was slightly negative , and the poisson ratio of C was in the region $0.0 < \nu < 0.5$.
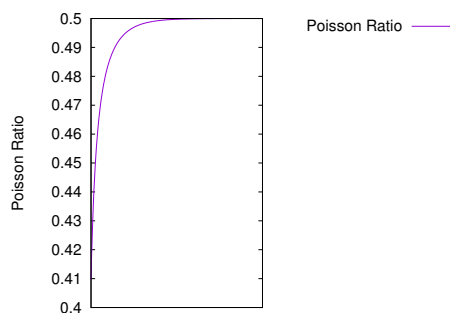
(a) The Poisson ratio for nucleus A. Converged to 0.5, i.e. incompressible.
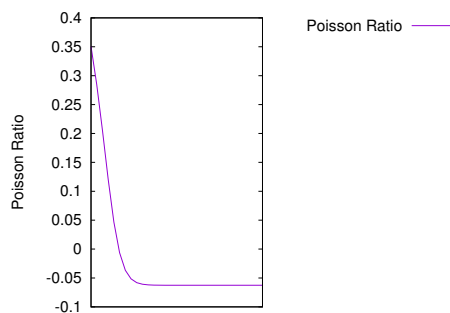
(b) The Poisson ratio for nucleus B. converged to slightly negative, -0.06.
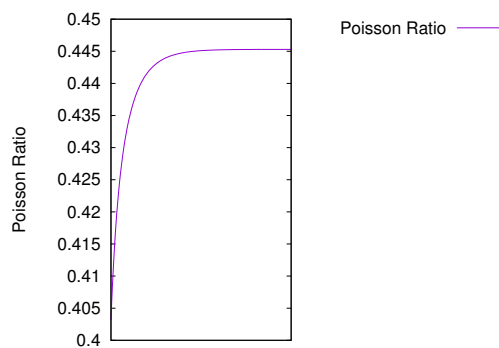
(c) The Poisson ratio for nucleus C. Converged to 0.45, i.e. typical behaviour.

Figure 5.3: Poisson's ratio calculated using the biaxial strain condition

5.5 Discussion

In the paper by K. Chalut et al [19], the Poisson's ratio of stem cell nuclei were measured in the small strain case, assuming that the resulting stress was uniaxial. However, as shown in figure 5.1, the uniaxial stress approximation leads to Poisson's ratios which are non-physical. The non-physical results are displayed in figure 5.1 by the shaded regions, where the blue shaded region represents $\nu < -1.0$ and the green shaded region represents $\nu > 0.5$. The nuclei within these regions are outside the physical limits of ν. These physical limits are set by the relations between ν and the definitions of the Young's modulus E, the Bulk modulus K and shear modulus μ, where the latter three are defined as $E, K, \mu > 0$, leading to the requirements that $0.5 > \nu > -1.0$.

The nuclei used in the analysis in the paper are separated in to two regimes based on size, called large and small nuclei. The large nuclei were defined as the nuclei with 25% largest areas and the small nuclei were those with the 25% smallest areas. We propose that these two regimes require different approximations in order to accurately describe the volume of the nuclei and the deformation that they experience in the out of plane directions.

If the nuclei are significantly smaller than the channel, we propose they should be treated differently to the large nuclei. The long axis of the small nuclei reach lengths of up to $14\mu m$, while the channel height in that direction is $16\mu m$. For this case, we propose that the uniaxial stress approximation, as used in the original work is appropriate. The uniaxial case assumes an symmetric deformation in the out of plane direction to that of the in plane long axes deformation, as shown in section 5.2.2.

For the large nuclei, which have long axes of similar lengths to the channel size before entry $(15 - 16\mu m)$ and grow to $(22 - 24\mu m)$ while inside the constriction, the uniaxial stress approximation is no longer appropriate. Instead we suggest that for the large nuclei, the Poisson's ratio should be calculated using the biaxial strain condition instead. This is due to size of the channels compared to the nucleus. For the uniaxial stress, as the paper

states, they presume that a one dimensional compression is applied to the cells using only the lateral walls, and so the cells are not constrained in the out of plane direction. This approximation is appropriate for the small nuclei, whose long axes are smaller than the constriction size in the out of plane direction. However, for the large nuclei, the walls of the constriction prevent this deformation from being possible. As we are unable to measure the exact deformation in this out of plane direction from the data provided with the paper, we presume that it deforms in such a way that the stress in the out of plane direction is zero, as detailed in the above Biaxial strain derivation in section 5.2.4.

In the biaxial strain condition, the two in plane directions have non-zero strain components while the out of plane direction strain component is zero. This corresponds to the stress in the out of plane direction being non-zero, but with no change in the deformation in the out of plane direction, meaning the strain in that direction is zero. The assumption here then is that because the nucleus completely fills the channel in the out of plane direction before and after entering the constriction, it does not deform in the out of plane direction, filling the channel entirely in and outside of the constriction.

In our results presented here, the biaxial approximation is applied to the nuclei (A), (B) and (C) as highlighted in figure 5.1, and the iterative method to determine a value of Poisson's ratio as describe in section 5.2 was used. In our results, each nucleus is treated as a homogeneous elastic solid, and the undeformed and deformed shapes are aligned by their respective centres of mass. As in figures 5.2a-5.2c, we calculated the strains for the each of the three chosen nuclei. The output values match the assumption of constant strains across the body, and the values found are consistent with the approximation of the strain in each direction as $u = \frac{\delta l}{l_0}$, where u is the strain in a direction with elliptic axis length change *deltal*, from a starting length l_0. The Poisson ratios found represent three different regimes as we expected, though not in the regions predicted by simply assuming $\nu = -\frac{u_{tt}}{u_{aa}}$.

We found nucleus (A) to behave as near incompressible, Nucleus (B) could still be displaying auxetic behaviour under this model and Nucleus (C) in the regime $0.0 < \nu < 0.5$. The result for nucleus (B) suggests that, based on this data and model, the nuclei could still be exhibiting auxetic behaviour under this model, though the conclusions that all the nuclei display this behaviour is not replicated by this approach.

The result for nucleus (A) suggests an non-physical result, in that though there should be a volume change, we predicted it is incompressible. However, given the data presented in the publication, we cannot identify whether the selected nuclei belonged to the larger set of nuclei, or the smaller set, so whether the biaxial strain or uniaxial stress condition is appropriate for nucleus (A) is unclear. The result of nucleus A approaching incompressible when there should be a volume change may be because of the assumption about the nucleus shape being incorrect in the out of plane direction.

5.6 Summary

In this chapter, we have used the computational model from chapter 3 for a homogeneous elastic solid to determine the deformation, strain,stress and traction of deforming cell nuclei, combined with a iterative method to calculate Poisson's ratio. We then compared the results from our model with published experimental data measuring the Poisson Ratio of nuclei.

Chapter 6

Nuclear deformation:3D model

6.1 Introduction

In this chapter, we develop the models of the nucleus discussed earlier in chapter 3 and 4 to allow for the use of three dimensional input data, rather than making assumptions about the shapes of the nucleus in the out of plane direction, as was done in earlier chapters. We begin by describing the changes in implementation from the two dimensional model, including the form of the input data, and a method for allowing the simulated annealing algorithm to perform perturbations in the out of plane direction. We then adapt the calculation of Poisson's ratio from Chapter 5 for use with three dimensional data. We then present some results using three dimensional images of nuclei.

6.2 Differences in implementation from 2d model

6.2.1 Conversion of images from experimental data for use in the three dimensional version of our model

In chapter 3.4, we detailed the method used to generate outlines of cell nuclei from a two dimensional image. We now use a similar approach to convert a series of z stacks into an input file for use with the three dimensional version of our code. As in the earlier chapter, we use existing functionality in the software imageJ [32], to convert each single image into an outline as in chapter 3.4. Each outline is then treated as the shape of the nucleus at a given height, as defined by the distance between z stacks. Figure 6.1 shows a cartoon example of the conversion of several z stacks into outlines and how the full shape represented by the stacks is approximated by connecting them with straight lines at a constant angle relative to the centre of mass.

The mesh representing the shape of the nucleus is formed from the z stacks as follows. First, we converted each stack into an outline following the procedure described in chapter 3.4. We then chose a reference stack, to be used to generate the mesh representing the nucleus. To generate, the mesh,
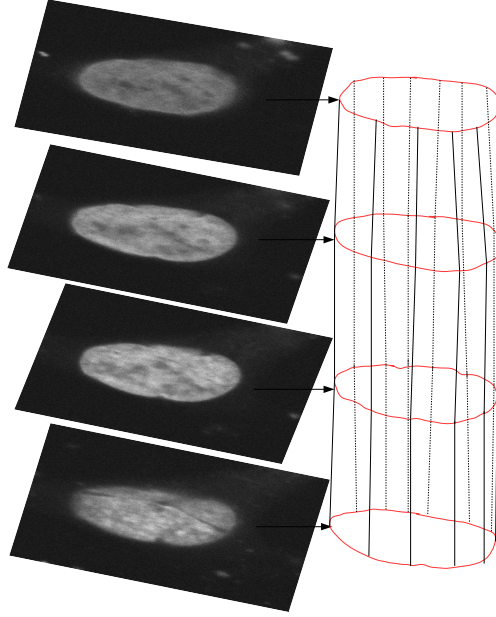
Figure 6.1: Example of the conversion of a series of zstacks in to the multiple outlines that make up the input shape in to our model.

we developed an algorithm to alter the input outlines as follows.

The first step of the algorithm is to change the number of points representing each stack. All the non-reference stacks on both the source and the target shape have points increased or decreased in order to have the same number of points as the reference stack. The number of points on each stack is reduced or increased by calculating the ratio r of the number of points in the reference stack n_{ref} to the number of points in the current stack n_{curr},

$$r = \frac{n_{ref}}{n_{curr}}.$$

(6.1)

The new outline with the same number of points as the reference stack is created by placing a point every r/L along the existing curve, where L is the

entire length of the curve. This results in a curve with the same number of points as the reference stack. This is repeated for every stack in both the target and source images, so that every stack has the same number of points.

The algorithm then aligns all the z stacks of the source shape, so that the list of points in each stack are located at the same angles in the x-y plane. This is done to have the coordinate system be (r, θ, s_2) in the solid model and (s_1, n, s_2) in the shell model, where r and θ have the standard polar coordinate definition, s_1 is the distance along the surface in the x-y plane along each outline in the x-y planes, s_2 is the direction along the mesh between points at a constant angle in each stack, and n is the direction normal to the surface.
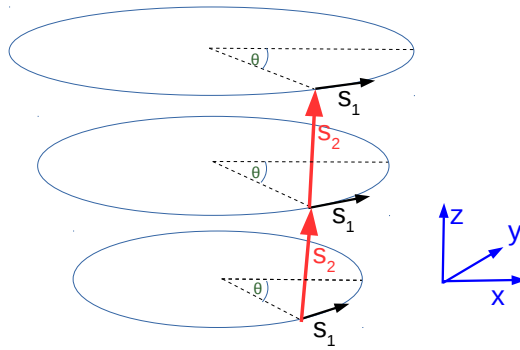
Figure 6.2: Cartoon showing the directions s_1 and s_2. s_1 is the in plane tangent direction along the outline of the nucleus, while s_2 is the tangent direction between different stacks at a fixed angle.

The last step completed by this part of our algorithm is to ensure that the target and source shapes have the same number of stacks making up each image. This is done in order to define the initial deformation field from the source to the target shape. The algorithm does this by increasing or decreasing the number of stacks in the target shape to match the number of stacks in the source shape. In order to modify the number of stacks in the target shape, the top and bottom stacks are kept fixed-. The total number of stacks is then done by using the assumption that each of the

stacks is connected by linear segments. This linear interpolation between the input stacks from the data allows gives an estimate to the shape of the nucleus at any height. Using the interpolation, a new stack is placed at each height z_j from the bottom most stack, where the height z_j is given in terms of the number of stacks before this remeshing step on the target and source,N_{target}, N_{source} respectively and the separation of the stacks in the experimental images, z_{sep} as

$$z_j = \frac{N_{target}}{N_{source}} z_{sep}.$$ (6.2)

This results in the target shape being represented by a series of equally spaced in height z stacks, with the source and target shapes now having the same number of stacks.

(a)   (b)
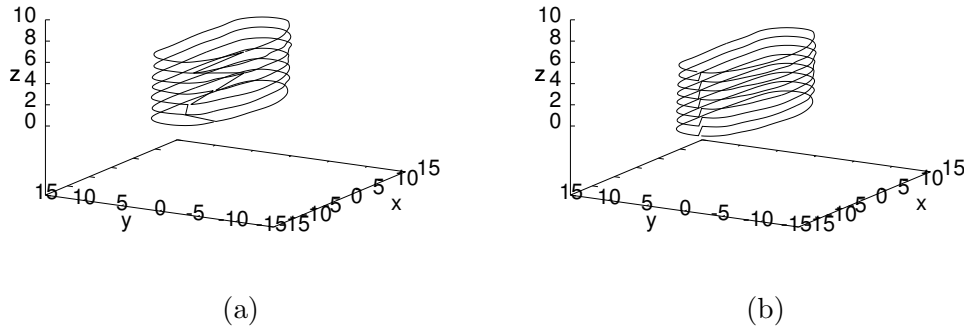
Figure 6.3: An example of the deformed shape before (a) and after (b) the remeshing algorithm. In this example, the source nucleus shape has one extra stack, so the number of stacks on the target shape is increased by one, using the method in chapter 6.2.1. The points on each stack have also been placed so that the smallest angle point is the first element in the list, and the lowest stack in the remeshed shape shifted to be at $z = 0$ to align the target and source shapes by the lowest stack.

6.2.2 Perturbations of z stacks in the out of plane direction
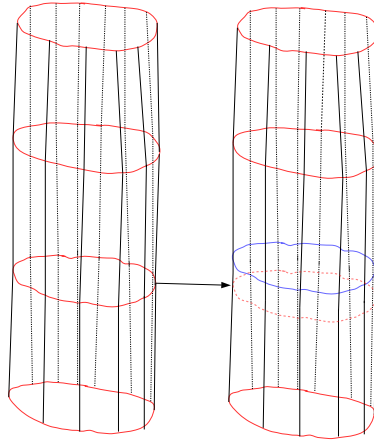
Figure 6.4: Example of the perturbation performed in three dimensions when using input three dimensional data. A potential perturbation is performed by selecting a stack at random, as shown by the arrow from the left cartoon to the right cartoon. The perturbation is then performed by moving the stack in the target shape either upwards or downwards, as shown by the blue outline on the right hand image, which in this example was perturbed upwards.

In addition to the perturbations in the x-y plane, with a full set of three dimensional data, we perform perturbations in the out of plane direction too. The x-y perturbations are performed using the same method on each stack as in the case with a single stack, as detailed in chapter3.10, while the method used for out of plane perturbations is described below.

Firstly, a z stack other than the top/bottom stacks is chosen at random. The top and bottom stacks are excluded in order to maintain the same total height of the mesh. Rather than perturbing a single point, as in the perturbations within the x-y plane, the out of plane perturbations occur by moving all the points on the selected z stack. Secondly, after selecting a stack, a random direction upwards/downwards (positive/negative s_2 directions respectively)

for the perturbation is selected. Each of the points on the chosen stack is moved in the appropriate direction 10% of the height between the selected stack and the next stack. An example of a perturbation is shown in figure 6.4. As the points were remeshed to all be at the same angle between different stacks, each point is moved along the straight line towards the point on the stack it is being deformed towards, to the new height for the z stack. Thirdly, in a similar fashion to the perturbations in the x-y plane, the energy of the new deformation at each point, in terms of the stress and strain tensors, is calculated using

$$f = \frac{1}{2}\sigma_{ij}u_{ij}. \tag{6.3}$$

There are two conditions where we choose to keep the newly perturbed deformation field. The first is where the perturbed deformation field causes the energy of deformation to decrease in comparison to the deformation prior to perturbation. The second is if the exponential of the energy change is bigger than a randomly generated number, i.e. $\exp\frac{-\Delta E}{k_b T} > R$, for a randomly generated number R, using the standard simulated annealing method, described in more detail earlier in chapter 3.10. These perturbations are performed until the minimal energy configuration is found, at which point, the chosen deformation, strain, stress and traction fields are output.

6.2.3 Calculation of values using three dimensional data

In earlier chapters, we used assumptions about the out of plane dimension to calculate the traction force causing deformations of the nucleus. Using a series of z stacks as input in to our model representing three dimensional data, the assumptions that need to be made about the out of plane direction are relaxed in comparison to the two dimensional case.

Using three dimensional data, the third direction in both solid and shell cases is given by the tangent vector, s_2, defined as the direction along the mesh between points at a constant angle in each stack, as mentioned in

section 6.2.1. As the shape is now known in the out of plane direction, we can calculate each of the deformation, strain and stress fields needed to find the traction force directly.

The outwards normal vector is found from the cross product of the two tangent vectors, s_1 and s_2 as

$$\mathbf{n} = \frac{s_1 \times s_2}{|s_1 \times s_2|}. \tag{6.4}$$

The strain is calculated as before, using the full expression for the derivatives of the deformation. Because the co-ordinate system is defined by the input shapes entirely here, the coordinates can be defined so that for the shell, each of the components of the tangent vectors and normal can be defined to be unit length. The tangent and normal basis being made of unit length vectors gives a metric tensor of

$$g_{ij} = \delta_{ij} \tag{6.5}$$

i.e. the identity matrix.

The same is true for the inverse of the metric, which is also the identity. This means all the christoffel symbols, Γ_{ij}^k are zero for these calculations, which simplifies the calculations of the derivatives along the surface. In general, the derivatives along the surface of the basis vectors are then given in terms of the curvature and metric as

$$\frac{\partial \mathbf{e_j}}{\partial x_i} = C_{ij}\mathbf{n} + \Gamma_{ij}^k \mathbf{e_k}. \tag{6.6}$$

where in the shell case, the indices represent one of the tangent vectors. In the case of using three dimensional input data, this simplifies leaving only the curvature tensor term proportional to the normal, C_{ij}.

The curvature is defined as the rate of change of the normal vector in

each of the tangent directions,

$$C_{ij}e_j = \frac{\partial \mathbf{n}}{\partial x_i}. \tag{6.7}$$

As the tangent directions are chosen as linearly independent vectors, so that $s_i \cdot s_j = \delta_{ij}$, i.e. 1 is $1 = j$ and 0 otherwise. Each component of the curvature can be numerically calculated at each point on the surface by taking the dot product of equation 6.7 in the appropriate direction. The equations numerically evaluated for each component are given as follows

$$C_{s_1 s_1} = \frac{\partial \mathbf{n}}{\partial s_1} \cdot e_{s_1}$$

$$C_{s_1 s_2} = \frac{\partial \mathbf{n}}{\partial s_1} \cdot e_{s_2}$$

$$C_{s_2 s_1} = \frac{\partial \mathbf{n}}{\partial s_2} \cdot e_{s_1}$$

$$C_{s_2 s_2} = \frac{\partial \mathbf{n}}{\partial s_2} \cdot e_{s_2}$$

.

6.3   Results

As in chapters 3 and 4, we present the results of our model applied to an example of a nucleus undergoing deformation. The example shown in figures 6.5 and 6.6 uses images of a RPE-1 cell nucleus, expressing inducible Plk4, provided by Pedro Monteiro and Susana Godinho. In this experiment, they imaged the nucleus of cells before and after treating the cell with the antibiotic doxycycline. This causes the cells to aquire extra centrosomes, with more microtubules forming which causes the nucleus to extend in the direction of the orientation of the microtubules. Here we use a image of the nucleus, prior to treatment, as the undeformed shape, and another image of

a nucleus, after the doxycycline treatment, as the deformed shape.Unlike in chapters 3 and 4, no averaging is performed on these images, and the results shown in figures 6.5 and 6.6 use only a single nucleus image for each shape of the nucleus.

In figure 6.5, we show the results of using our model where we have treated the nucleus as a homogeneous elastic solid, using a series of z stacks to represent the three dimensional shape of the nucleus. Figure 6.6 uses the same input data, instead treating the nucleus as a homogeneous elastic shell. These nuclei are treated as a compressible elastic material (Poisson's ratio $\nu < 0.5$). When using the two dimensional data in chapters 3 and 4, we assumed the behaviour in the out of plane direction matched the requirements for incompressibility. Here there is an observable volume change between the undeformed and deformed shapes and therefore they cannot be incompressible. For the purposes of this example, we assume a Poisson's ratio of $\nu = 0.4$.

In the example of a solid nucleus, shown in figure 6.5, the top and bottom layers have shrunk during the s_1 energy minimisation process, where s_1 is as shown in figure 6.2. The change in area can be seen when comparing the final shape to the shape prior to energy minimisation as shown in figure 6.3. This did not occur in the equivalent shell results. This can be explained because the solid model treats this nucleus as a filled three dimensional shape. This assumption affects the closed surface on the top and bottom of the nucleus. The top and bottom surfaces shrink where it is energetically preferable to shrink the surface around the centre of mass. This did not occur in the shell model of the nucleus, as the decrease in size does not necessarily have the same benefit in energy reduction from decreasing the deformation around the centre of mass that is seen in the solid model of the nucleus. Instead, the shell model shows a more significant change in the positions of the stacks of the deformed shape along s_2 (where s_2 is as shown in figure 6.2), where they move to minimise the deformation normal to the surface to reduce the terms

(a)   (b)

(c)   (d)
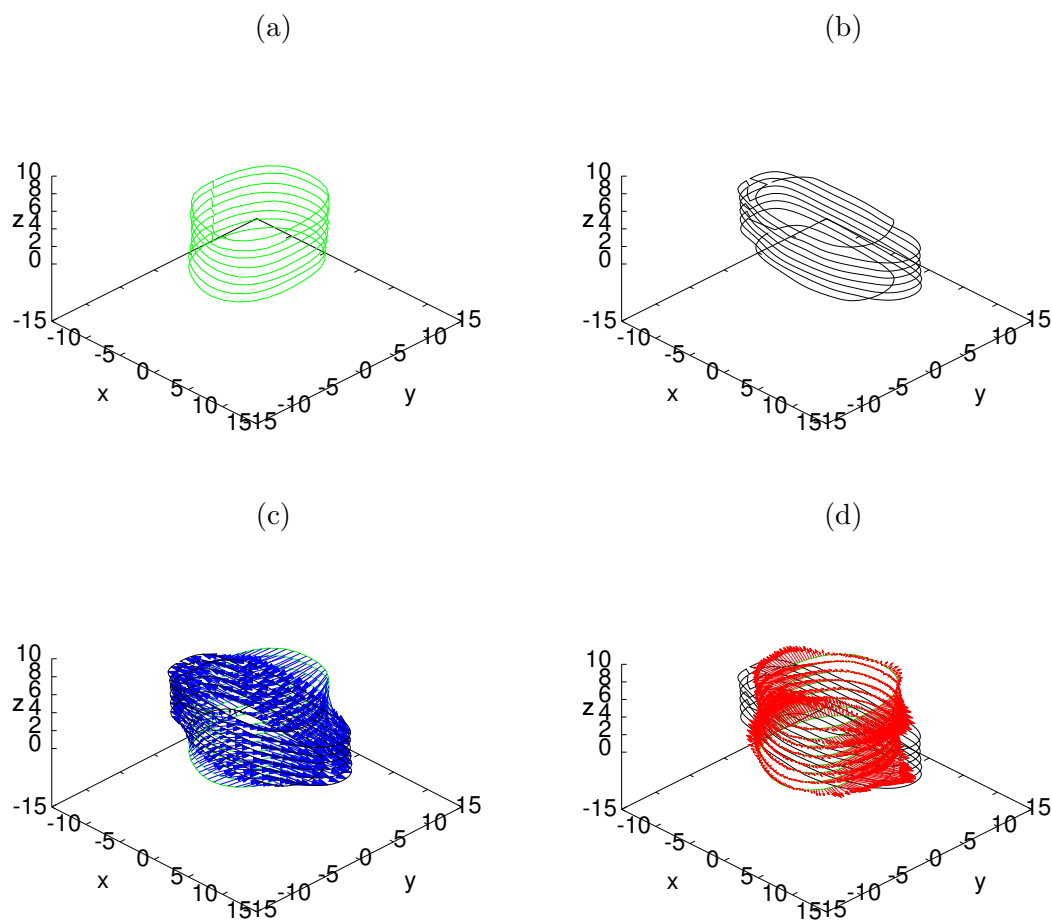
Figure 6.5: The results of our model treating the nucleus as a homogeneous elastic solid, applied to images of a RPE-1 cell nucleus before and another image of a nucleus after being treated with doxycycline. (a) and (b) show the undeformed (prior to treatment) and deformed (after treatment) shapes found after the energy minimisation procedure. The blue arrows in (c) show the final deformation field from the undeformed to the deformed shape. The red arrows in (d) represent the traction field causing the deformation shown in (c), and they are scaled such that one unit of length on the axes represents a traction force of 10kPa. This example uses Young's modulus $E = 5000Pa$ and Poisson's ratio $\nu = 0.4$.

(a)   (b)

(c)   (d)
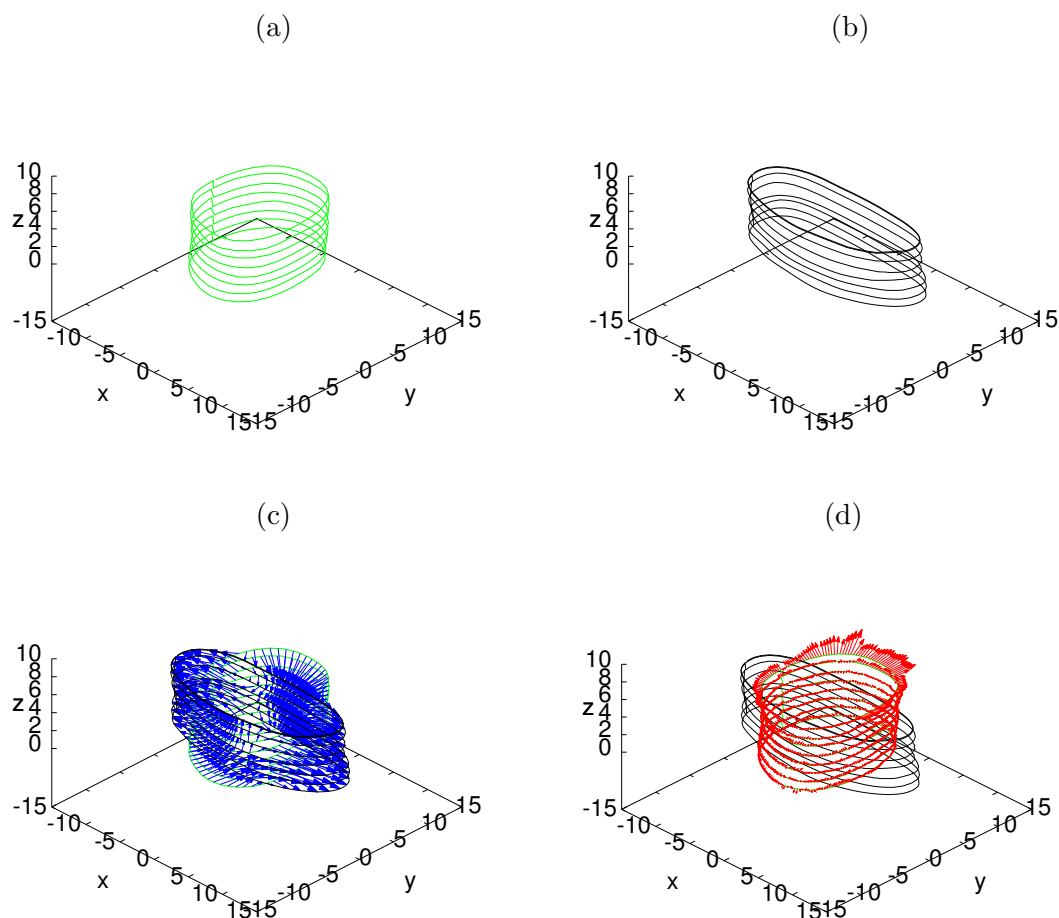
Figure 6.6: The results of our model treating the nucleus as a homogeneous elastic shell, applied to images of a RPE-1 cell nucleus before and another image of a nucleus after being treated with doxycycline. (a) and (b) show the undeformed (prior to treatment) and deformed (after treatment) shapes found after the energy minimisation procedure. The blue arrows in (c) show the final deformation field from the undeformed to the deformed shape. The red arrows in (d) represent the traction field causing the deformation shown in (c), and they are scaled such that one unit of length on the axes represents a traction force of 10kPa. This example uses Young's modulus $E = 5000Pa$ and Poisson's ratio $\nu = 0.4$.

in the strain proportional to the normal deformation. As in chapters 3 and 4, the magnitudes of the traction forces are generally smaller when treating the nucleus as a elastic shell rather than a solid.

These images demonstrate the use of our computational model with three dimensional data input from a series of z stacks, in both the solid and shell modes, for a compressible nucleus.

6.4 Conclusions

In this chapter, we have extended the computational model described in chapters 3 and 4 to calculate the deformation and traction of cell nuclei from three dimensional data given by a series of z stacks. We extended the method used to convert images in to two dimensional data for use with three dimensional data. In order to allow the nucleus to deform in the out of plane direction, we then added an additional component to the meshing algorithm. This addition allowed the computational model to increase or decrease the number of stacks that make up the deformed shape, if it does not initially match the number of stacks in the undeformed shape. This is used to allow a one to one mapping to be defined between the undeformed and deformed shapes, for each point on each stack of the undeformed shape. Perturbations of entire stacks was allowed in order to allow for deformations along the s_2 direction. We then used images of RPE-1 nuclei to provide an example of using this model to calculate traction forces using three dimensional data.

Chapter 7

Conclusions

7.1 Summary

In this thesis, we have presented work to help analyse and understand the deformation of cell nuclei.

In chapter 2, we developed an analytical model of the motion of molecular motors, using a Asymmetric Simple Exclusion Process model to describe the observed discrete stepping motion of the molecular motors.

In chapters 3, 4 and 6, we created a computational tool used to predict the deformation of nuclei based on simulated annealing energy minimisation simulations. This enabled us to predict the traction forces required to deform nuclei from experimental images. In chapters 3 and 4, we used two dimensional data and approximations of the shape in the out of plane direction, whilst in chapter 6 used a series of z stacks to represent the three dimensional shape of the nucleus. Chapter 3 described a model where the nucleus was treated as a homogeneous elastic solid, while in chapter 4 the nucleus was treated as a thin homogeneous elastic shell. Chapter 6 extended both of these models to use three dimensional data.

In chapter 5, we used the simulated annealing model together with an iterative method to determine the Poisson's ratio of nuclei, comparing results with an existing publication.

7.2 Future work

One extension to the work presented in chapters 3, 4 and 6 could be to compare the traction forces predicted with force generation mechanisms within the cell that could be deforming the nucleus. In both the nucleus deforming to enter in to constriction experiments shown in figure 7.1 and when cells were treated with doxycycline, as in figure 7.2, florescence microscopy observations showed an increase in actin and microtubules respectively. These could be used by the cell to cause the observed deformations. The traction forces could be compared with the density of the respective filaments

through a comparison of the intensity of emitted light in stained images, with the magnitude of the traction force calculated at that point on the nucleus surface. As the intensity of the emitted light should be representative of the amount of the stained biological matter at that point in an image, if the traction is caused by a particular filament, we would expect some correlation between the density of the filaments near the surface and the traction forces needed at each position on the surface.
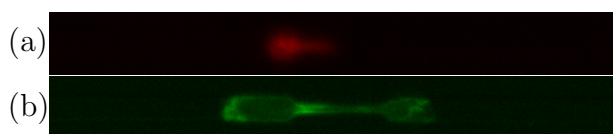
Figure 7.1: An image showing the increase in actin as a nucleus enters a channel. The DNA within the nucleus is shown in red in (a), while actin is shown in green in (b). There is an increase in the amount of actin along the sides of the constriction where the nucleus enters the constriction. Images provided by Hawa Thiam Matthieu Piel.
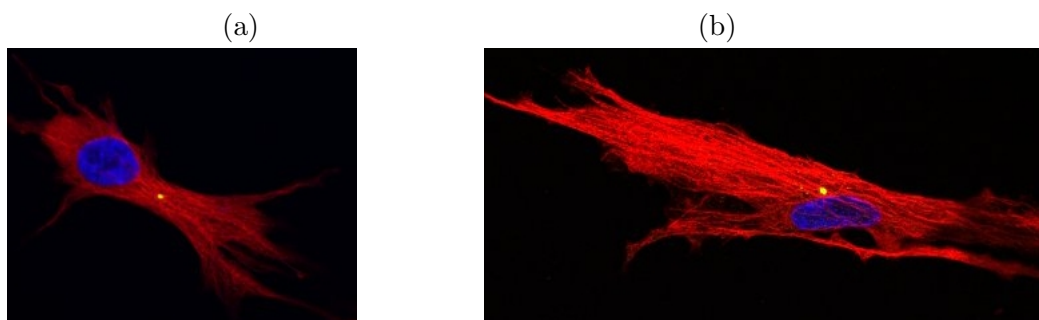
Figure 7.2: Images showing the increase in microtubules around a nucleus (a) prior to treatment and (b) a nucleus after treatment with Doxycycline. The DNA within the nucleus is shown in blue, while microtubules are shown in red and centrosomes in green. There is an increase in the amount of microtubules around the nucleus after treatment. Images provided by Pedro Monteiro and Susana Godinho.

In Chapter 5, we performed calculations of Poisson's ratio, ν, with two

dimensional data and approximations of the shape in the out of plane direction. With 3D data as a series of z stacks, we could perform a similar calculation, but with a direct measurement of the volume of the cell nucleus. Briefly we suggest one this could be done.
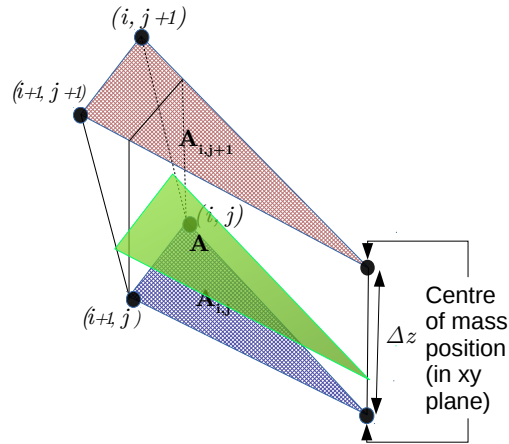
Figure 7.3: Cartoon example showing the positions of the coordinates used to estimate the volume of a segment of the curve between two z stacks. The volume is then calculated between the two stacks by finding the areas of the two triangles formed by the points (i, j),$(i + 1, j)$ and $(i, j + 1)$,$(i + 1, j + 1)$ around the centre of mass, and assuming that the surface formed by the four points is a flat plane.

In the case of a compressible material, to calculate the Poisson's ratio we would need to first find the volume change between undeformed and deformed shapes. Once the input source and target shapes have been remeshed as described in chapter 6, to have the same number of points on each stack, and each stack remeshed to have points at the same list of angles on each stack, as described in chapter 6.2.1, the volume can be calculated from the three dimensional mesh as follows. The volume of the shape between each z stack is then found by using the distances around the centre of mass at points (i, j),$(i + 1, j)$,$(i, j + 1)$ and $(i + 1, j + 1)$. These points form triangular shapes in the xy plane. The volume of each segment, an example of which is shown in figure 7.3 can be used to calculate the volume of the entire shape.

In the figure, the areas of the triangles formed by the points $(i, j), (i + 1, j)$ and the centre of mass is labelled $A_{i,j}$, similarly the area of the triangle given by $(i, j + 1), (i + 1, j + 1)$ and the centre of mass is shown by $A_{i,j+1}$. As we assume the points are joined by a flat plane between stacks, the outline of the shape always forms a similar triangle at each value of z between the two planes observed from experimental data. Each intermediate triangle, having an area A as shown by the green outline. The volume can be calculated by integrating over all the triangle areas between the two known planes. As the angle between the points θ_i is the same between stacks, assuming the length of the positions increases/decreases linearly between stacks, each triangle area A can be written as:

$$A = \frac{\sin(\theta)}{2} \left(l_{i,j} + (l_{i,j+1} - l_{i,j}) \frac{z}{z_{sep}}) \right) \left(l_{i+1,j} + (l_{i+1,j+1} - l_{i+1,j}) \frac{z}{z_{sep}}) \right)$$

$$(7.1)$$

$$v_{i,j} = \int_{z=0}^{z=z_{sep}} A \, dz = \frac{\sin(\theta)}{6} z_{sep} \left(l_{i,j+1} \left(l_{i+1,j+1} + \frac{l_{i+1,j}}{2} \right) + l_{i,j} \left(\frac{l_{i+1,j+1}}{2} + l_{i+1,j} \right) \right)$$

$$(7.2)$$

The total volume occupied between the z stacks is then the sum of $v_{i,j}$ over all points on the z stacks, i.e.

$$V = \sum_i \sum_j v_{i,j} \tag{7.3}$$

where $v_{i,j}$ is given in equation 7.2. In cases where the nucleus is bounded at the top and bottom z stacks, for example, when the nucleus and cell are attached to a surface, this value represents the total volume of the nucleus. If the nucleus is free at either or both ends, there would be an additional volume given in the region above/below the plane seen in the image. However, the way to treat this value would depend on the experimental set up, e.g. if the

nucleus was free on one end, while bounded on another, the free end could be treated as a spherical cap while the bottom stack assumed to have zero volume below it.

In the two dimensional case, Poisson's ratio ν was calculated using an iterative method as described in chapter 5. One of the steps involved in the iterative calculation was calculating the average pressure over the surface. With two dimensional data, the pressure at each point was weighted by the distance equal to half the total line length between each of the neighbouring points. When three dimensional data is input in to our model, the pressure at each point would need to be weighted differently. For instance, weighted by an area segment representing the region the pressure acts on.

In this case, the weighting for each point would be given by the area between midpoints of the nearest neighbours. For a point (i, j), the nearest neighbours in the in plane direction are $(i \pm 1, j)$ and in the out of plane direction are $(i, j \pm 1)$. As the surface between different z stacks and between points in plane are approximated as being connected by straight lines in both directions, this causes the area segment to be rectangular. The area between the midpoints of the neighbouring points is given by

$$A_{i,j} = \frac{1}{4}|\mathbf{X}_{i+1,j} - \mathbf{X}_{i-1,j}||\mathbf{X}_{i,j+1} - \mathbf{X}_{i,j-1}|. \tag{7.4}$$

If the stack currently being weighted is on the top or bottom of the shape, the weighting is instead modified to

$$A_{i,j}^{top} = \frac{1}{4}|\mathbf{X}_{i+1,j} - \mathbf{X}_{i-1,j}||\mathbf{X}_{i,j} - \mathbf{X}_{i,j-1}|. \tag{7.5}$$

$$A_{i,j}^{bot} = \frac{1}{4}|\mathbf{X}_{i+1,j} - \mathbf{X}_{i-1,j}||\mathbf{X}_{i,j+1} - \mathbf{X}_{i,j}|. \tag{7.6}$$

respectively, making these areas approximately half the value of the other stacks, as the shape above or below the top and bottom stacks is unknown.

This would allow the poisson's ratio to be predicted from three dimen-

sional experimental data, and therefore avoid the potential non-physical re-
sults as mentioned in chapter 5, where assumptions were made about the out
of plane behaviour.

Another addition that could improve the results is how the innards of the
nucleus should be treated. In chapter 3 we presented a model of the nucleus
as a homogeneous elastic solid, and in chapter 4, as a homogeneous elastic
shell with contents that freely deform with no contribution to the stress on
the surface. These provide two extreme limits for describing the behaviour of
the nucleus as an elastic material. The nuclear lamina is typically assumed
to behave elastically, while the contents of the nucleus can show viscoelastic
behaviour. In the solid model, we assumed that the entire nucleus displayed
the same elastic properties throughout. The viscoelasticity could be incorpo-
rated by using a viscoelastic model where the viscous term is negligible on the
surface to replicate the elasticity of the lamina, but non-negligible viscosity
inside the body of the nucleus to represent the contents of the nucleus.

7.3 Conclusions

In this thesis we have studied the deformation of the nucleus. To do this, we have developed a computational model for analysing images of nucleus deformation. In this model, we used the laws of continuum mechanics and classical elasticity theory to describe the nucleus of a cell as an elastic material. These simulations could be applied to a wide range of nuclei, or indeed, any elastic material undergoing deformation. This could have applications in medical identification of diseased cells, as well as uses in identifying force generation mechanisms causing observed deformations.

Bibliography

[1] Spudich James A et al. "Optical Traps to Study Properties of Molecular Motors". In: *Cold Spring Harbor protocols* 2011.11 (Nov. 2011), pp. 1305–1318. ISSN: 1940-3402 1559-6095. URL: `http://www.ncbi.nlm.nih.gov/pmc/articles/PMC4784437/`.

[2] Rachid Ait-Haddou and Walter Herzog. "Brownian ratchet models of molecular motors". In: *Cell Biochemistry and Biophysics* 38.2 (2003), pp. 191–213. ISSN: 1559-0283. DOI: `10.1385/CBB:38:2:191`. URL: `http://dx.doi.org/10.1385/CBB:38:2:191`.

[3] Bruce Alberts et al. *Molecular Biology of the Cell*. 4th ed. Garland Science, 2002. ISBN: 0815332181. URL: `http://www.amazon.com/exec/obidos/redirect?tag=citeulike07-20%5C&path=ASIN/0815332181`.

[4] B. Alberts et al. "Molecular Biology of the Cell". In: New york: Garland Science, 2008.

[5] Charlotte Alibert, Bruno Goud, and Jean-Baptiste Manneville. "Are cancer cells really softer than normal cells?" In: *Biology of the Cell* 109.5 (2017), pp. 167–189. ISSN: 1768-322X. DOI: `10.1111/boc.201600078`. URL: `http://dx.doi.org/10.1111/boc.201600078`.

[6] Nathalie Caille et al. "Contribution of the nucleus to the mechanical properties of endothelial cells." eng. In: *J Biomech* 35.2 (Feb. 2002),

pp. 177–187. DOI: `10.1016/S0021-9290(01)00201-9`. URL: `http://www.sciencedirect.com/science/article/pii/S0021929001002019`.

[7] O Campas et al. "Collective dynamics of interacting molecular motors". In: *Physical review letters* 97.3 (2006), p. 038101.

[8] Patricia M. Davidson et al. "Design of a microfluidic device to quantify dynamic intra-nuclear deformation during cell migration through confining environments". In: *Integr. Biol.* 7 (12 2015), pp. 1534–1546. DOI: `10.1039/C5IB00200A`. URL: `http://dx.doi.org/10.1039/C5IB00200A`.

[9] Celine M. Denais et al. "Nuclear envelope rupture and repair during cancer cell migration". In: *Science* 352.6283 (2016), pp. 353–358. ISSN: 0036-8075. DOI: `10.1126/science.aad7297`. eprint: `http://science.sciencemag.org/content/352/6283/353.full.pdf`. URL: `http://science.sciencemag.org/content/352/6283/353`.

[10] Celine Denais and Jan Lammerding. "Nuclear Mechanics in Cancer". In: *Advances in experimental medicine and biology* 773 (2014), pp. 435–470.

[11] B Derrida et al. "Exact solution of a 1D asymmetric exclusion model using a matrix formulation". In: *Journal of Physics A: Mathematical and General* 26.7 (1993), p. 1493. URL: `http://stacks.iop.org/0305-4470/26/i=7/a=011`.

[12] M. R. Evans. "Bose-Einstein condensation in disordered exclusion models and relation to traffic flow". In: *EPL (Europhysics Letters)* 36.1 (1996), p. 13. URL: `http://stacks.iop.org/0295-5075/36/i=1/a=013`.

[13] M. E. Foulaadvand and M. Neek-Amal. "Asymmetric simple exclusion process describing conflicting traffic flows". In: *EPL (Europhysics Letters)* 80.6 (2007), p. 60002. URL: `http://stacks.iop.org/0295-5075/80/i=6/a=60002`.

[14] Daan Frenkel and Berend Smit. *Understanding Molecular Simulation.* 2nd. Orlando, FL, USA: Academic Press, Inc., 2001. ISBN: 0122673514.

[15] Zhijian Fu et al. "The effect of individual tendency on crowd evacuation efficiency under inhomogeneous exit attraction using a static field modified {FFCA} model". In: *Physica A: Statistical Mechanics and its Applications* 392.23 (2013), pp. 6090–6099. ISSN: 0378-4371. DOI: `http://dx.doi.org/10.1016/j.physa.2013.07.062`. URL: `http://www.sciencedirect.com/science/article/pii/S0378437113006936`.

[16] Barbara J Gabryś, Karol Pesz, and Stanisław J Bartkiewicz. "Brownian motion, molecular motors and ratchets". In: *Physica A: Statistical Mechanics and its Applications* 336.1–2 (2004). Proceedings of the {XVIII} Max Born Symposium "Statistical Physics outside Physics", pp. 112–122. ISSN: 0378-4371. DOI: `http://dx.doi.org/10.1016/j.physa.2004.01.016`. URL: `http://www.sciencedirect.com/science/article/pii/S0378437104000391`.

[17] C. Giverso, A. Grillo, and L. Preziosi. "Influence of nucleus deformability on cell entry into cylindrical structures". English. In: *Biomechanics and Modeling in Mechanobiology* 13.3 (2014), pp. 481–502. ISSN: 1617-7959. DOI: `10.1007/s10237-013-0510-3`. URL: `http://dx.doi.org/10.1007/s10237-013-0510-3`.

[18] Farshid Guilak, John R. Tedrow, and Rainer Burgkart. "Viscoelastic Properties of the Cell Nucleus". In: *Biochemical and Biophysical Research Communications* 269.3 (2000), pp. 781–786. ISSN: 0006-291X. DOI: `http://dx.doi.org/10.1006/bbrc.2000.2360`. URL: `http://www.sciencedirect.com/science/article/pii/S0006291X0092360X`.

[19] Andrew C. Hodgson et al. "A microfluidic device for characterizing nuclear deformations". In: *Lab Chip* 17 (5 2017), pp. 805–813. DOI: `10.1039/C6LC01308B`. URL: `http://dx.doi.org/10.1039/C6LC01308B`.

[20] Andrew J. Holland and Don W. Cleveland. "Polo-like Kinase 4 Inhibition: A Strategy for Cancer Therapy?" In: *Cancer Cell* 26.2 (2014), pp. 151–153. ISSN: 1535-6108. DOI: `https://doi.org/10.1016/j.ccr.2014.07.017`. URL: `http://www.sciencedirect.com/science/article/pii/S1535610814003067`.

[21] Tatyana G. Kuznetsova et al. "Atomic force microscopy probing of cell elasticity". In: *Micron* 38.8 (2007). Microscopy in Nanobiotechnology, pp. 824–833. ISSN: 0968-4328. DOI: `https://doi.org/10.1016/j.micron.2007.06.011`. URL: `http://www.sciencedirect.com/science/article/pii/S0968432807001047`.

[22] P. J. M. Laarhoven and E. H. L. Aarts, eds. *Simulated Annealing: Theory and Applications*. Norwell, MA, USA: Kluwer Academic Publishers, 1987. ISBN: 9-027-72513-6.

[23] Jan Lammerding et al. "Lamins A and C but Not Lamin B1 Regulate Nuclear Mechanics". In: *Journal of Biological Chemistry* 281.35 (2006), pp. 25768–25780. DOI: `10.1074/jbc.M513511200`. eprint: `http://www.jbc.org/content/281/35/25768.full.pdf+html`. URL: `http://www.jbc.org/content/281/35/25768.abstract`.

[24] L. D. Landau et al. *Theory of Elasticity, Third Edition: Volume 7 (Theoretical Physics)*. 3rd ed. Butterworth-Heinemann, Jan. 1986. ISBN: 075062633X. URL: `http://www.amazon.com/exec/obidos/redirect?tag=citeulike07-20%5C&path=ASIN/075062633X`.

[25] A. B. Mathur, G. A. Truskey, and W. M. Reichert. "Atomic force and total internal reflection fluorescence microscopy for the study of force transmission in endothelial cells." eng. In: *Biophys J* 78.4 (Apr. 2000), pp. 1725–1735. DOI: `10.1016/S0006-3495(00)76724-5`. URL: `http://www.sciencedirect.com/science/article/pii/S0006349500767245`.

[26] Oliver Otto et al. "Real-time deformability cytometry: on-the-fly cell mechanical phenotyping". In: *Nature Methods* 12.3 (Feb. 2015), pp. 199–202. DOI: 10.1038/nmeth.3281. URL: http://www.nature.com/nmeth/journal/v12/n3/pdf/nmeth.3281.pdf.

[27] Hanchuan Peng et al. "BrainAligner: 3D registration atlases of Drosophila brains". In: *Nat Meth* 8 (6 June 2011). DOI: http://dx.doi.org/10.1038/nmeth.1602.

[28] Matthew Raab et al. "ESCRT III repairs nuclear envelope ruptures during cell migration to limit DNA damage and cell death". In: 352 (Mar. 2016).

[29] Massimo Reconditi et al. "The myosin motor in muscle generates a smaller and slower working stroke at higher load". In: *Nature* 428.6982 (2004), pp. 578–581.

[30] Matthias Rief et al. "Myosin-V stepping kinetics: A molecular model for processivity". In: *Proceedings of the National Academy of Sciences of the United States of America* 97.17 (June 2000), pp. 9482–9486. ISSN: 0027-8424 1091-6490. URL: http://www.ncbi.nlm.nih.gov/pmc/articles/PMC16890/.

[31] A. C. Rowat, J. Lammerding, and J. H. Ipsen. "Mechanical properties of the cell nucleus and the effect of emerin deficiency." eng. In: *Biophys J* 91.12 (Dec. 2006), pp. 4649–4664. DOI: 10.1529/biophysj.106.086454. URL: http://dx.doi.org/10.1529/biophysj.106.086454.

[32] Caroline A Schneider, Wayne S Rasband, and Kevin W Eliceiri. "NIH Image to ImageJ: 25 years of image analysis". In: *Nat Meth* 9 (7 July 2012), pp. 671–675. DOI: http://dx.doi.org/10.1038/nmeth.2089.

[33] Frank Spitzer. "Interaction of Markov processes". In: *Advances in Mathematics* 5.2 (1970), pp. 246–290. ISSN: 0001-8708. DOI: http://dx.doi.org/10.1016/0001-8708(70)90034-4. URL: http://www.sciencedirect.com/science/article/pii/0001870870900344.

[34] *Subtract background: ImageJ Documentation Wiki.* Accessed: 2016-12-10. URL: `http://imagejdocu.tudor.lu/doku.php?id=gui:process:subtract_background`.

[35] Marvin E Tanenbaum, Anna Akhmanova, and Rene Medema. "Bidirectional transport of the nucleus by dynein and kinesin-1". In: *Communicative & integrative biology* 4.1 (2011), pp. 21–25.

[36] Hawa-Racine Thiam et al. "(Perinuclear) Arp 2/3 driven actin polymerizzation enables strong nuclear deformation during immune cells migration". In: *submitted (check published)* ().

[37] Koen Visscher, Mark J Schnitzer, and Steven M Block. "Single kinesin molecules studied with a molecular force clamp". In: *Nature* 400.6740 (1999), pp. 184–189.

[38] Barbara Zitová and Jan Flusser. "Image registration methods: a survey". In: *Image and Vision Computing* 21.11 (2003), pp. 977–1000. ISSN: 0262-8856. DOI: `http://dx.doi.org/10.1016/S0262-8856(03)00137-9`. URL: `http://www.sciencedirect.com/science/article/pii/S0262885603001379`.